PROCESS DEVELOPMENT OF DRAWCASTING STRUCTURES IN THERMOPLASTIC FILMS

A Dissertation
Presented to
The Academic Faculty

by

Katherine Copenhaver

In Partial Fulfillment
of the Requirements for the Degree
Doctor of Philosophy in the
School of Materials Science and Engineering

Georgia Institute of Technology
December 2019

PROCESS DEVELOPMENT OF DRAWCASTING STRUCTURES IN THERMOPLASTIC FILMS

Approved by:

Dr. Jason Nadler, Advisor
Advanced Concepts Laboratory
Structured and Applied Materials Branch
Georgia Tech Research Institute

Dr. Karl Jacob
School of Materials Science and Engineering
Georgia Institute of Technology

Dr. Richard Ng
Kimberly Clark Corporate Research & Engineering

Dr. Vladimir Tsukruk
School of Materials Science and Engineering
Georgia Institute of Technology

Dr. Meisha Shofner
School of Materials Science and Engineering
Georgia Institute of Technology

Date Approved: November 1, 2019

For my sweet Nanny, who I love so much and miss every day beyond words.
I wish you could have seen me finish this.
And for my niece, Maryn Mae, who gave us all a reason to keep going.

πάντα ῥεῖ

ACKNOWLEDGEMENTS

I am so grateful to everyone who made this possible for me, because I certainly did not do it alone. First, I am so thankful to my boss, Dr. Jason Nadler, for hiring me when I had very little lab experience, and for letting me work on polymers in his non-polymers lab. I hope I have convinced everyone that polymers are actually the best materials. Thank you to my coworkers for their support, patience, and advice along the way. I want to give a specific thank you to Keri Ledford, both for all the photolithographic and cleanroom work you did on this project, and for not holding all the broken wafers against me.

I would also like to thank my collaborators at the Kimberly Clark Corporation: Dr. Richard Ng, Dwayne Jackson, and Andrew Baker, without whom none of this would be possible. I deeply appreciate your support, guidance, understanding, and generosity over the past number of years. I could not have asked for better sponsors or collaborators.

Additionally, I would like to thank all my committee members for their time and dedication in reviewing, contemplating, and discussing this work. I have taken classes from a number of them during my time at Georgia Tech, and I truly appreciate their contributions to this work and my education as a whole.

Finally, I'll never be able to adequately thank my family and friends in Georgia, Tennessee, and elsewhere, for their love and encouragement throughout this process. I would not have made it through 2019 in particular without their support.

TABLE OF CONTENTS

LIST OF TABLES

LIST OF FIGURES

LIST OF SYMBOLS AND ABBREVIATIONS

AR	aspect ratio
UV	ultra-violet
PDMS	polydimethylsiloxane
T_g	glass transition temperature
μm	micron/micrometer
nm	nanometer
GPa	gigapascal
kPa	kilopascal
cm	centimeter
PVS	polyvinyl siloxane
PU	polyurethane
DRIE	deep reactive ion etching
PMGI	poly (methyl glutarimide)
PMMA	poly (methyl methacrylate)
ETPTA	ethoxylated trimethylolpropane triacrylate
PVA	polyvinyl alcohol
IR	infrared
EHD	electrohydrodynamic
PS	polystyrene
PVDF	polyvinylidene fluoride
T_m	melting temperature
VFT	Vogel-Fulcher-Tammann

η_s or η	shear viscosity
T_0	polymer's ideal T_g or reference temperature
η_E	extensional viscosity
τ_E	extensional stress
$\dot{\varepsilon}$	extension rate
F-TIR	frustrated total internal reflection
mm	millimeter
BGA	ball grid array
ICP	inductively coupled plasma
°C	degrees Celsius
R_c	radius of curvature
SEM	scanning electron microscope
MPa	megapascal
ITO	indium tin oxide
T_d	decomposition temperature
$\dot{\gamma}$ or $\dot{\gamma}_{yx}$	shear rate
θ_c	contact angle
LDPE	low-density polyethylene
MFI	melt flow index
kDa	kilodaltons
PDI	polydispersity index
kg	kilograms
TGA	thermogravimetric analysis
DSC	differential scanning calorimetry

DTA	differential thermal analysis
STA	simultaneous thermal analysis
ΔH_m	heat of fusion
ΔH_c	heat of cold crystallization
ΔH_m^o	heat of fusion of a purely crystalline polymer
μg	micrograms
mL	milliliters
l_0	polymer drop linear dimension
γ	surface tension or strain
$\bar{\bar{\pi}}$	total stress tensor
$\bar{\bar{\delta}}$	identity matrix
$\bar{\bar{\tau}}$	shear stress tensor
N_1	first normal stress difference
N_2	second normal stress difference
Ψ_1	first normal stress coefficient
Ψ_2	second normal stress coefficient
η_0	zero-shear viscosity
LVE	linear viscoelastic envelope
SAOS	small amplitude oscillatory shear
ω	angular frequency
δ	phase angle
G’	storage modulus
G’’	loss modulus
De	Deborah number

Wi	Weissenberg number
λ	characteristic relaxation time
TTS	time-temperature superposition
a_T	horizontal shift factor
WLF	Williams-Landel-Ferry
c_1, c_2	WLF constants
E	Arrhenius activation energy
R	gas constant
η^*	complex viscosity
η_∞	infinite-shear viscosity
PSA	pressure-sensitive adhesive
rad	radians
HDPE	high-density polyethylene
gf	grams force

SUMMARY

The micro- and nanostructures of natural surfaces leading to functionalities such as anti-fogging, antimicrobial, water collecting, and adhesion are often studied and used as inspiration in the design of synthetic surfaces and products. Many surfaces structures such as micro-ridges or bumps that lend unique fluid-handling properties can be easily fabricated over large areas and have become commonplace in products like anti-fogging goggles or self-cleaning windows. Surfaces with high-aspect-ratio (AR) micro- or nanostructures that impart adhesion, however, are more challenging to manufacture on a large scale in a practical manner, primarily due to high fabrication costs and low-throughput processes. While dry adhesive surfaces with high-AR structures with narrow stems and broad, flat tops are commonly produced on a laboratory scale using silicone materials and multiple photolithography and molding steps, a low-cost, simple fabrication technique amenable to a variety of shapes, length scales, and materials has not yet been developed.

In this thesis, a new process for patterning polymer surfaces with high-AR structures, termed drawcasting, is developed and parameterized. The current state-of-art in the fabrication of three-dimensional, high-AR polymer structures and the limitations of various techniques are first discussed. Drawcasting is then presented as a means of producing a wide variety of surface structure arrays in a flexible, low-cost, and scalable manner.

Drawcasting is an extensional deformation process in which a templated pattern is dipped or submerged in a thermoplastic film or polymer resin. The pattern is then raised,

forming capillary bridged between the pattern elements and the parent material. A phase transformation is then induced through cooling or curing, and the pattern is removed to yield high-AR structure arrays with tips defined by the geometry of the pattern elements. Throughout this work, drawcasting was used to produce arrays of high-AR microstructures with narrow stems and concave, cup-like tips from thermoplastic polymers, termed micro-suction cups.

The geometry of the resulting structure arrays depends on both the process parameters and the material properties of the polymer in use. These complex relationships between the material properties, process parameters, and structure geometry were studied in this work. The development of the drawcasting testbed as well as innovations in process optimization techniques are first discussed, and the evolution and adaptation of novel techniques in molding, lithography, and microscopy that aid in preparation and execution of the drawcasting process are presented. The rate-, time-, and temperature-dependent properties of three polymer samples as they relate to the drawcasting process are then examined. The thermal, wetting, and rheological properties of each polymer were experimentally studied in order to establish limits on the drawcasting process parameters and to provide a basis for future thermofluid modeling. Finally, the production of micro-suction cup arrays on various length scales using a broad range of process parameters is documented, and results from these drawcasting experiments are compared to those from material properties studies. An understanding of a polymer's thermal, wetting, and rheological behavior was found to be essential in developing a functional, reliable, and predictable drawcasting procedure.

CHAPTER 1 INTRODUCTION

The study of natural surfaces exhibiting unique functions has long attracted researchers from a wide array of fields including biology, physics, chemistry, and materials science. Many natural surfaces are comprised of regular, three-dimensional structures that are responsible for their behavior. For example, the microscopic bumps on lotus and rice leaves are often studied for their superhydrophobic and self-cleaning capabilities. Water striders and similar insects have hydrophobic surface structures on their legs that leverage surface tension and allow them to walk on the surface of water. Additionally, the eyes of most flies and mosquitoes are comprised of hierarchical nanostructures that afford them anti-fogging capabilities, and many desert-dwelling plants and insects have micro- and nanostructures on their surfaces that promote condensation in order to increase water collection. Finally, organisms with adhesive surfaces such as the gecko, octopus, and diving beetles are of high interest with regard to the development of bio-inspired wet and dry adhesives. A number of these structured surfaces are shown in Figure 1.1 [1-12].

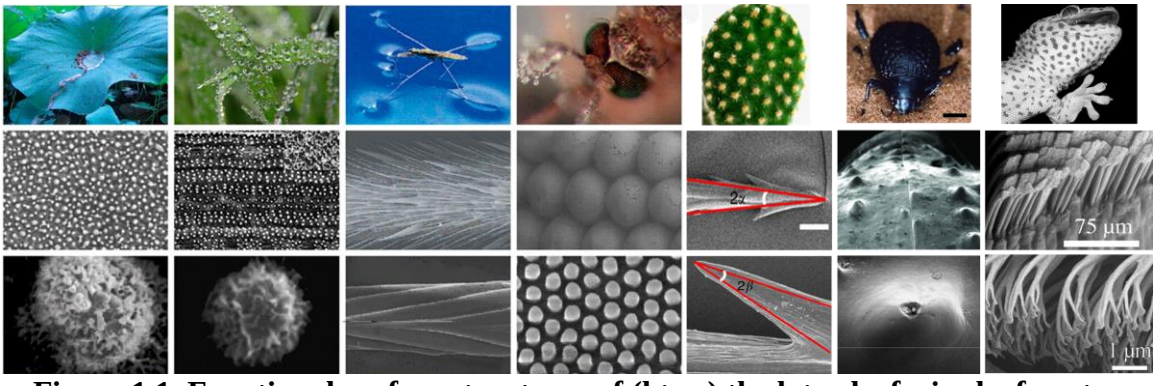

Figure 1.1. Functional surface structures of (l to r) the lotus leaf, rice leaf, water strider, fly eye, desert cactus, desert beetle, and gecko toe [2]

There is a great deal of literature in the field of bio-inspired adhesives. The most commonly mimicked adhesive surface structure is that of the gecko, which exhibits both wet and dry adhesion through hierarchical, spatula-shaped surface structures found on each toe pad [13-18]. Structured adhesives inspired by the surfaces of gecko toes or other organisms have advantages over the more commonly used pressure-sensitive adhesives, which are usually flat pads comprised of a low viscosity, tacky polymer. Structured adhesives are generally more reusable as they can exhibit self-cleaning capabilities, and they can provide better airflow between their substrate and the adherend, which is attractive for use in personal products and medical applications [2,19-22]. Structured surfaces and their relation to adhesive properties will be discussed thoroughly in subsequent chapters.

The majority of techniques for fabricating bio-inspired surfaces involve complex photolithography and molding steps that are not feasible beyond a lab scale due to their heavy reliance on cleanroom processes and resulting high cost [3,23]. These structured surfaces are most commonly prepared using thermally- or UV-curable resins such as polydimethylsiloxane (PDMS) [24-26]. Furthermore, the most prevalent structure fabricated to create bio-inspired adhesive surfaces consists of a high-aspect-ratio column terminating in a wide, flat top, which is referred to as a "mushroom" structure [2,3,27-33]. In this work, inspiration was taken from the surface structures of diving beetles, which are high-AR structures that terminate in a cup- or bowl-like shape. These structures, shown in Figure 1.2, are herein referred to as "micro-suction cups."

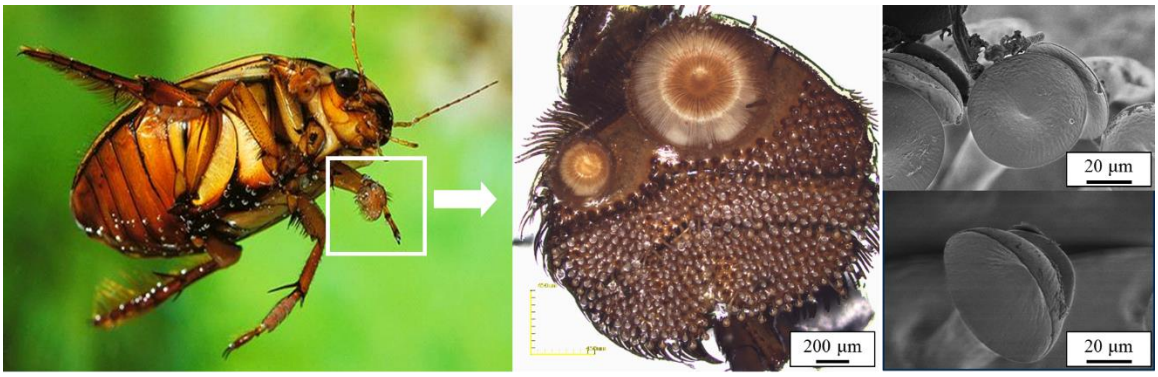

Figure 1.2. Surface structures of diving beetle attachment pad

As flat-tipped mushroom microstructures have been shown to exhibit similar adhesive properties to that of the gecko toe through van der Waals forces alone [27,29,32,34-37], similarly-scaled structures arrays of structures with concave tips may exhibit enhanced adhesion due to an added suction effect.

High-AR micro- or nanostructures with tip geometries other that flat or pointed are very rare in literature due to the difficulty in their fabrication. Photolithography is typically used to create positive or negative geometries with straight or slanted side walls, and curved architectures can typically only be achieved through successive thermal treatments [38-41]. These fabrication techniques and many others will be discussed in further chapters.

In this work, we present a new process, termed drawcasting, for patterning thermoplastics or curable viscous resins with concave-tipped surface structures. Arrays of micro-suction cups at a range of sizes are produced in this work, but drawcasting is amenable to a vast array of tip shapes. Drawcasting is an extensional deformation process in which templated patterns are drawn from a molten or uncured parent material. To produce micro-suction cups, a heated array of hemispheres is lowered into a molten thermoplastic film and subsequently raised. The molten polymer is drawn upward with the

pattern, forming a capillary bridge. The system is then allowed to cool below the polymer's glass transition temperature (T_g), and the cups are released from the hemispherical array. The geometry of the resulting structure arrays depends on both the processing parameters such as temperature and speed, as well as the temperature-, rate-, and time-dependent properties of the materials used. While these structure arrays are inspired by dry biological adhesives, this work is focused on the development of the drawcasting process itself, rather than the performance of the obtained structures. Drawcasting is the first process in existence that can reliably produce arrays of high-AR polymer surface structures with concave or otherwise structured tips that does not rely primarily on photolithographically-prepared molds.

The thermal, wetting, and rheological behavior of three common industrial thermoplastics will be studied in this work as they relate to the drawcasting process in attempts to establish upper and lower limits of the processing variables to ensure successfully structure fabrication. Furthermore, this work will provide a background for future analytical or numerical modeling of the drawcasting process. Understanding the limits of drawcasting and the relationships between process parameters, material properties, and obtained structures could allow the process to be scaled up to an industrial level or to be applied to different length scales, materials, and structure tips.

Chapter 2 of this thesis discusses the fundamental mechanisms of adhesion as well as biological surfaces commonly mimicked on the laboratory scale. A range of surface patterning techniques are also detailed, including photolithographic, molding, electrohydrodynamic, and drawing processes. The drawcasting process is then presented in Chapter 3. Each step of the process is discussed along with techniques used to prepare

components of the drawcasting fixture and to optimize the process itself. Chapter 4 outlines the experimental techniques used to characterize the chosen thermoplastics' temperature-, rate-, and time-dependent properties, as well as the samples fabricated using drawcasting. The results of the material characterization experiments are discussed in Chapter 5, while drawn structure arrays at a range of sizes are presented in Chapter 6. Finally, Chapter 7 both concludes the thesis and discusses current and planned work that will further improve the drawcasting process and facilitate its application to different length scales.

CHAPTER 2. LITERATURE REVIEW

The following sections detail the fabrication of common bio-inspired structured surfaces on laboratory scales, with particular attention given to those fabricated for dry adhesive applications. A description of the fundamentals of adhesive mechanisms is first given in order to establish the context for the type of structure typically targeted for a given surface. The structured surfaces of different organisms exhibiting wet and dry adhesion are then discussed. The examples given have been widely studied for their adhesive properties, and there is an abundance of literature devoted to synthetic surfaces inspired by each of the organisms discussed. An analysis of the effect of the adhesive structure's geometry on the adhesive function and performance of the organism as a whole is presented. A variety of methods employed on the lab scale to fabricate high-AR structured polymer surfaces at the micro- and nanoscale are then detailed. Common failure modes and barriers to process scale-up are then considered, followed by a discussion of common materials used in the production of structured polymer surfaces.

2.1. Adhesion Mechanisms

2.1.1. Wet Adhesion and Surface Fouling

From the perspective of designing a structured adhesive surface, the underlying mechanism through which the adhesive might cling to the adherend surface needs to first be understood. The local chemical and topographical environment can fundamentally change the type of adhesion taking place. Namely, the surface roughness and the presence

or absence of surface fluid often dictates the type of surface structure necessary for adhesion to occur. A wide variety of adhesion mechanisms exist in nature, including mechanical interactions such as hooks or vacuum, chemical interactions, electrostatic charges, quantum mechanical forces such as van der Waals forces and magnetics, and hydrophobic or hydrophilic interactions. Excluding mechanical adhesion and magnetics, adhesive mechanisms are generally classified as "wet" or "dry." [22,42]

Wet adhesives rely on a liquid to create a high degree of contact area between two surfaces. Aside from a chemical bonding agent such as super glue or epoxy, this can be achieved by an intermediate liquid between two surfaces, or by one highly compliant surface in contact with a rough substrate, which could be either rigid or compliant as well. Adhesion through an intermediate liquid can be classified as either Stefan or capillary adhesion, depending on separation distance between the two adhering surfaces. Stefan adhesion occurs when two surfaces are closely separated by a thin liquid film (film thickness/lateral surface dimension«1). The force required to separate these two surfaces is primarily a consequence of the viscosity of the fluid. At larger separations, capillary adhesion dominates. As two surfaces with an intermediate liquid are separated, the liquid forms a capillary bridge between the surfaces, the curvature and tenacity of which is governed by the surface tensions and ensuing contact angles of the liquid and surfaces in contact. The strength of the capillary adhesion is due to a resistance of the liquid to both form a new surface by elongating the capillary bridge and to dewet the adherend surface. Wet adhesion through a compliant surface, on the other hand, is often termed "pressure-sensitive" adhesion, as a force is usually required to deform the compliant surface in order to establish a certain degree of contact area necessary for adhesion. The adhesive force in

this case is due to van der Waals forces, which are significant when the separation between a given pair of particles is on the nanoscale. The strength of adhesion in this case depends on the established contact area, as a higher degree of close contact between the two surfaces will result in more van der Waals attraction. The contact area, in turn, is dependent on the applied pressure [1,42-46].

Wet adhesives are typically either permanent in the case of chemical transformations, or they can be removed but are not reusable. Capillary-based adhesives or pressure-sensitive adhesives are particularly susceptible to contamination, which can disrupt a capillary bridge or greatly reduce the contact area in the case of pressure-sensitive adhesives. Furthermore, pressure-sensitive adhesives are often acrylate-based and leave behind sticky residues. This is particularly disadvantageous in the case of skin adhesives used in healthcare and personal products. Acrylate-based adhesives also have poor biocompatibility with prolonged skin exposure, as they do not allow any ventilation of air or moisture wicking. Overall, the ability of wet adhesive to be reused is drastically reduced by their sensitivity to surface fouling, while pressure-sensitive adhesives in particular are also prone to stress concentrations due to their bulk deformation, which reduces their mechanical durability [2,47,48].

2.1.2. Dry Adhesion and Surface Structuring

Dry adhesives are essentially films that can adhere to other surfaces without needing to a secondary liquid or a high degree of bulk compliance. Dry adhesives rely on the same van der Waals adhesion mechanism as pressure-sensitive adhesives, which

necessitates a high degree of contact area. Dry adhesives, however, operate without needing a large extent of elastic deformation. Conformal contact in this case is accomplished by splitting up the adhesive surface into discrete structures, which is commonly referred to as "contact splitting." Dividing an adhesive surface into numerous subcontacts offers the surface a much lower effective modulus without changing the properties of the bulk material. In this way, a dry adhesive can achieve the same degree of contact area as a similar pressure-sensitive adhesive without developing stress concentrations in the bulk of the material. High-AR fibrillar structures in particular enhance the ability of a surface to conform to a rough adherend, even if they are comprised of a relatively high modulus material, as the structured surface greatly reduces the amount of elastic deformation necessary to create a given contact area. These long fibrils can conform to the roughness of a given substrate with a lower strain energy penalty than that of a smooth, flat surface. Furthermore, any energy penalty associated with distortion of a slender fibrillar element to accommodate a rough substrate is overcome by the reduction in interfacial free energy that occurs when fibrils make conformal contact with the substrate. Conformal contact achieved by fibrillar structures on the surfaces of an adhesive pad is illustrated in Figure 2.1 [2,46,48-53].

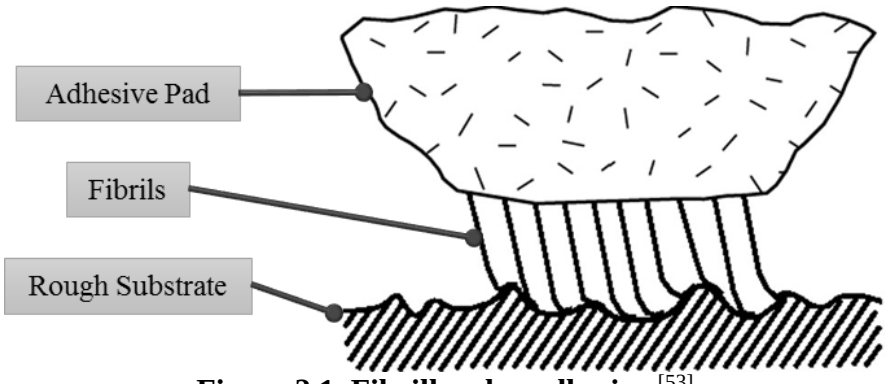

Figure 2.1. Fibrillar dry adhesive [53]

Additionally, contact splitting causes an adhesive surface to be less sensitive to defects or impurities such as dust or dirt particles that may be present on an adherend surface. A surface pollutant preventing the detachment of one subcontact will not affect the neighboring structures, as illustrated in Figure 2.2.

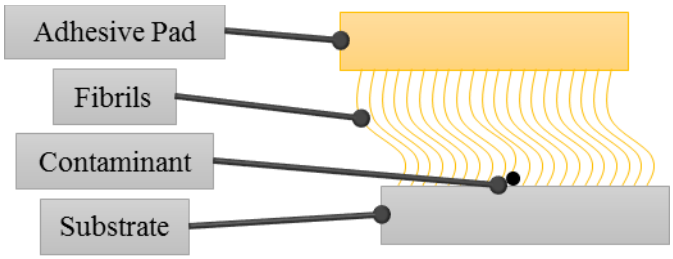

Figure 2.2. Fibrillar adhesive displaying insensitivity to surface contaminants

Contact splitting also leads to a phenomenon known as crack trapping, in which a crack or break in adhesion between one subcontact or group of subcontacts on a structured adhesive surface will not propagate over the entire contact area. When an individual fibril is elongated until its contact with the adherend breaks, the energy supplied to deform the fiber is dissipated inelastically rather than returned to the bulk. The crack must be reinitiated at each subcontact to allow for complete detachment of the surfaces. In the case of a smooth, cohesive contact like that of a pressure-sensitive adhesive, any surface asperities can prevent contact between the two surfaces in a region much larger than the asperity itself. In the absence of any defect-tolerant structures or crack blunting mechanisms that are present in structured adhesives, these cracks can easily spread to cause detachment in response to any retractive force on the adhesive [3,21,46,49,54,55].

The multitudes of subcontact points on a structured dry adhesive that reduce its sensitivity to surface roughness, cracks, and, particularly, surface impurities typically allow

these adhesives to be reusable. The van der Waals-based bonding in dry adhesives is usually nondestructive and temporary, meaning it can be detached and reattached many times without significantly degrading its adhesive performance. In the case of skin adhesion, structured dry adhesives are expected to provide better biocompatibility than their pressure-sensitive analogues, as the separation between the bulk material and the adherend given by the surface structures would allow for air ventilation. Furthermore, since dry adhesives can be comprised of materials with a higher bulk modulus, they leave no residue on the skin after detachment [2,19].

2.2. Biological Adhesives

Arguably, the most widely studied and mimicked biological system exhibiting dry adhesion is that of gecko feet, which exhibit reversible dry and wet adhesion as well as self-cleaning abilities. Other commonly studied adhesive systems include the toe pads of tree frogs and cup-like structures found on octopi and some types of beetles. The adhesive micro- and nanostructures of these organisms are herein discussed, with attention given to the effect of the structure geometry on the type and strength of the adhesive bond.

2.2.1. Organisms with Adhesive Structures

The adhesive and self-cleaning functions exhibited by geckoes are attributed to the hierarchical arrangement of approximately 20 rows of transversely arranged lamellae on each of the gecko's toe pads. The lamellae are further divided into setae, of which there are

between 500,000 and 1,000,000 per foot. The setae are, on average, 110 μm tall and 5 μm in diameter. Each seta branches into flat "spatula" structures at the tip. Each spatula structure is up to 2 μm in length and generally 200 nm in diameter, and there are typically 100 to 1000 spatulae per seta. The structures on the gecko's toes are comprised of β-keratin, which exhibits an elastic modulus of 2-4 GPa. However, the hierarchical fibrillar toe pad structures present an effective modulus of approximately 100 kPa, which is similar to the modulus of many pressure-sensitive adhesives. These structures allow the gecko toes to establish a high contact area on surfaces with widely varying roughness amplitudes, generating considerable van der Waals adhesive forces. Geckoes are, in fact, the largest known organisms that can adhere to irregular surfaces by using intermolecular forces alone. The hierarchical structures of a gecko toe pad are shown in Figure 2.3 [15,17,34,42,52,56-59].

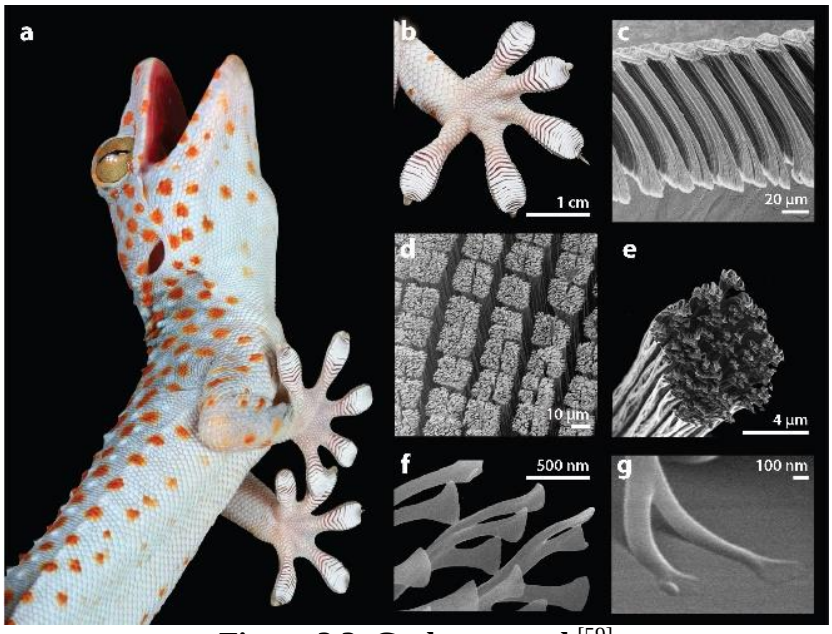

Figure 2.3. Gecko toe pad [59]

The surface structures found in the toes of tree frogs are also widely studied and used for the fabrication of bio-inspired functional adhesives. The toes are comprised of hierarchical arrays of 10 to 15-μm wide hexagonal cells separated by 1-μm wide and 10-μm deep channels. Each cell is further divided into arrays of nanopillars, which are between 200 and 400 nm in diameter and terminate in a concave shape. These structures are depicted in Figure 2.4.

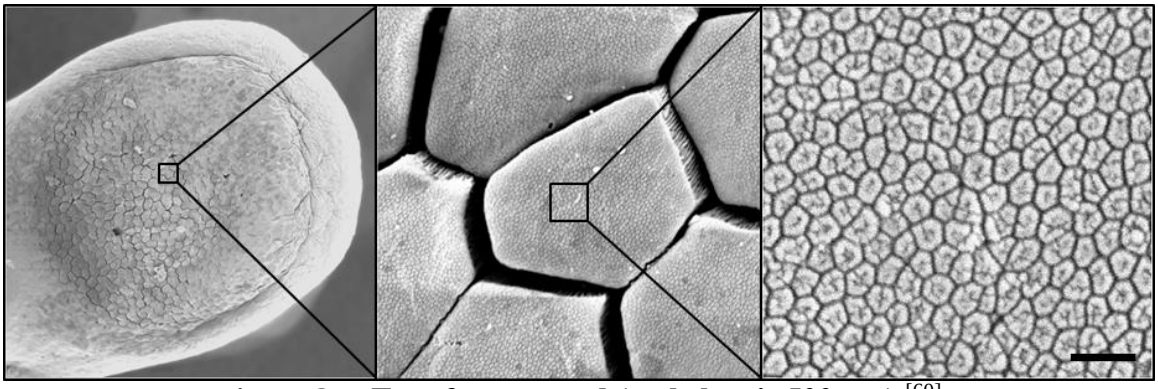

Figure 2.4. Tree frog toe pad (scale bar is 500 μm) [60]

The frog secretes a mucus into the contact area between the toe pad and substrates through the channels between the hexagonal cells. The tree frog's adhesion is mainly through Stefan and capillary forces generated and controlled by the flow of mucus within the cells and nanopillars [42,60-62].

The underside of the arms of octopuses are famously covered in suction cup structures that allow them to adhere to surfaces as well as manipulate soft or hard objects with arbitrary surface geometries. The suction cups or "suckers," as they are typically referred to in literature, can be anywhere between 1 mm and 1 cm in diameter depending on the type and size of the octopus, as well as the position of the sucker on the arm. Each sucker consists of two general regions connected by a constricted orifice or sphincter. The

first region, the infundibulum, is the exposed disk-like portion of the sucker that is reshaped by extrinsic muscles to conform to an exterior surface. The second region, the acetabulum, is a hollow portion below the infundibulum and sphincter. Extrinsic muscles expand the acetabulum in order to generate negative pressure within the sucker, and the sphincter also expands or contracts to limit fluid flow between the two regions. Octopus suckers adhere to surfaces primarily through suction forces, which are controlled by surrounding muscles that act in response to sensory input. A cross-section of a typical octopus sucker is shown in Figure 2.5 [63-66].

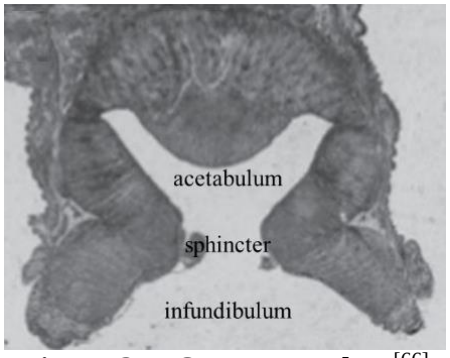

Figure 2.5. Octopus sucker [66]

Varieties of beetles have arrays of high-AR fibrillar structures terminating in a concave bowl-like shape on their front legs. Male boreal water beetles (family *Dytiscidae*) use these structures to grasp females during mating. The suction cups are comprised of a narrow stem or shaft with a wider cup or bowl shape at the end. There are deep folds in the stem where it meets the cup that allow the cup to tilt, which aids the male beetle during mating, as the female beetle usually tries to away erratically after being attacked by a male. The adhesive pad of a male water beetle consists of one to two large primary cups and medium secondary cups, respectively, and a large number of small cups. The number, size,

and arrangement of these cups all vary between species, and has been found to be directly related to the surface roughness of the elytra, or hardened forewings, of the male beetles species' female counterparts [67-69].

For example, the adhesive pad of a male *dysticus marginalus* consists of one primary cup approximately 900 μm in diameter, one secondary cup approximately 650 μm in diameter, and up to 150 small cups with a maximum diameter of 50 μm. In contrast, the adhesive pad of *gradopherus zonatus* is comprised of 3 primary cups and between 30 and 70 small cups. The large suction cups on diving beetles are primarily used to adhere to smooth surfaces, while the smaller and more numerous cups allow the beetles pad to adapt to uneven surfaces by offering a lower effective modulus as has been observed in gecko toe pads. The number of small cups on the adhesive pads of beetles in family *Dytscidae* has been found to vary between 20 and 1000. The toe pads of two different species of *Dytscidae* beetles, *Dysticus lapponicus* and *Graphoderus zonatus*, are shown in Figure 2.6 [70].

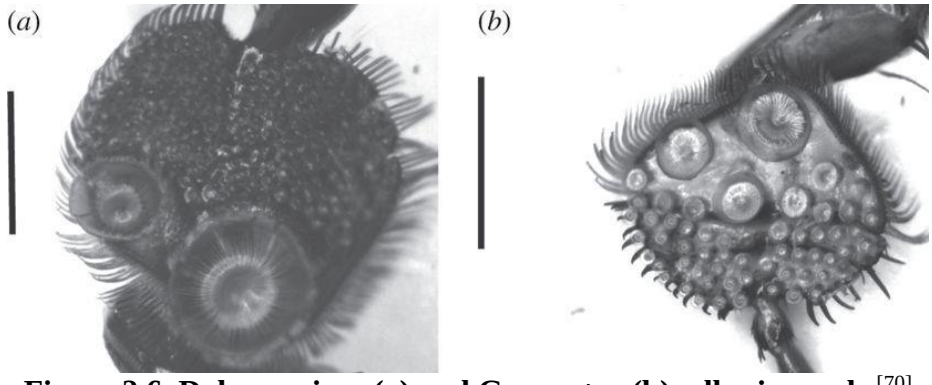

Figure 2.6. D. lapponicus (a) and G. zonatus (b) adhesive pads [70]

The number and variety of sizes of suction cups on the beetle adhesion pad afford adhesion through both van der Waals and suction forces. In some species, the small cups have been

found to account for approximately 40% of the overall adhesion force of the attachment pad on the rough female elytra. The male beetle strikes the female with sufficient force to cause the adhesive cups to rotate and flatten, while the tendency of the cups to elastically return to their original shape generates a negative pressure under them [67-72].

2.2.2. Scaling Considerations

In general, larger organisms such as geckos with structured adhesive pads or appendages tend to have smaller and more densely packed terminal contacts than that of a small organism such as a spider or beetle. The adhesive strength of biological systems has been found to be inversely proportional to the radius of the terminal structure, suggesting that increasing the density and reducing the diameter of surface structures would lead to enhanced adhesive performance. Furthermore, fibrils of different lengths at constant diameter have shown an increase in adhesion force with increasing length, as higher-AR fibrils can dissipate a larger amount of elastic energy at pull-off. However, increasing the aspect ratio of fibrillar structures in order to reduce the adhesive pad's effective modulus can lead to failure of the structures in the form of lateral collapse or stiction, entanglement, or fiber rupture due to excessive elongation. Many animals resolved these problems by evolving structures that are tilted with respect to the adhesive pad or base, which can lower the surface's effective modulus without needing to increase the aspect ratio of the structures, or through hierarchical structures as seen in the gecko and tree frog's adhesive pads. In order to design and develop effective, robust, and reusable structured adhesive inspired by biological systems like those mentioned in the previous section, a balance must

be found between the material's elastic modulus and the adhesive surface's effective modulus. In other words, the material must be sufficiently stiff to avoid structural damage after repeated use, while it must be sufficiently soft or the geometry must be optimized in such a way to achieve a necessary degree of conformal contact between the surface structures and the adherend [2,21,44,45,54,56,69].

2.2.3. Structure Geometry

2.2.3.1. Flat Tips

Biological adhesive structures rarely terminate in flat pillar shapes. Instead, adhesive surface structures often broaden or thin at the tip, depending on their function. Structures comprised of a narrow stem with a flat, broad top perpendicular to the stem are commonly referred to in literature as "mushroom" structures, while structures terminating in a thin, flat shape, as those seen on the gecko, are described as "spatula" structures. These structures are depicted schematically in Figure 2.7 [3].

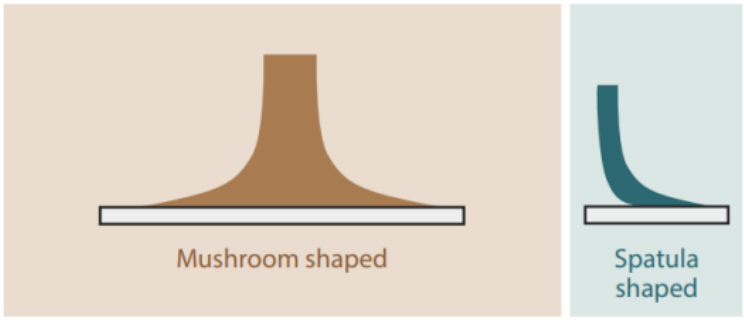

Figure 2.7. Biological adhesive structure tips [3]

Flat spatula structures are more suited for short-term, dynamic applications, and achieve adhesion by being dragged across a surface. Dragging the setae in shear pulls the spatula tip in tension, which results in large frictional and adhesive forces. The contact can also be broken quickly by peeling, which makes these structures ideal for locomotion. These spatula shapes are typically seen in fast-moving organisms such as flies, spiders, some beetles, and the gecko. Mushroom-shaped structures, however, do not require a shear stress or frictional force to achieve adhesion. Mushroom structures can remain passively adhered to a substrate and can often withstand high normal and angled pull-off forces before detaching, which makes them suitable for prolonged attachment [59,69].

The thin contact pad of mushroom structures also reduces stress concentrations that occur at the outer edge of flat pillar-like structures. In response to tension on the fiber, a thin contact pad can deform rather than accumulate stress concentrations at the edges. The stress profile across the contact area then depends on the thickness of the tip, diameter of the tip, and the diameter of the stem. If the contact pad is too thin or too thick, stress singularities can arise at the outer edge of the stem where it joins the wider tip or at the outer edge of the tip, respectively, leading to adhesive failure by interfacial crack propagation. However, if the geometry of the tip and stem are optimized, pulling forces are more likely to induce center cracks that grow radially outward until failure. These cracks can form a low-pressure zone inside the contact area during removal, which would lead to a suction contribution to the overall adhesion force. Furthermore, narrowing the stem of a mushroom structure will lower its bending stiffness, allowing it to better withstand angled pull-off or shear. Optimized mushroom-tipped structured adhesives have exhibited pull-off

forces up to an order of magnitude higher than similar tip-less pillar-like structures [2,3,21,34,46,73-75].

2.2.3.2. Concave Tips

In pull-off tests of artificial mushroom-tipped structured adhesives, it has been shown that suction can contribute to up to 10% of the overall pull-off force, while the remaining pull-off force was attributed to van der Waals adhesion. This was demonstrated by Heepe and Varenberg when testing 50-µm diameter polyvinylsiloxane (PVS) mushroom structure arrays under reduced and atmospheric conditions. These structures are shown in Figure 2.8 [76].

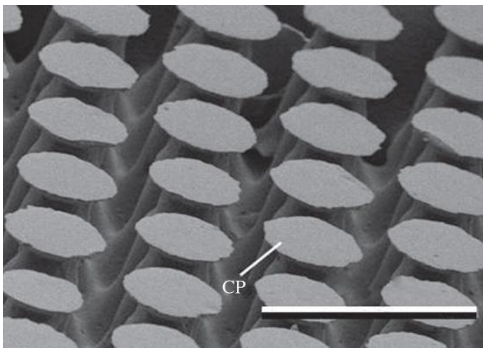

Figure 2.8. Mushroom-tipped PVS structure array (scale bar is 100 µm) [76]

This suction contribution could be further enhanced by structuring the tops of these fibrillar adhesives to be curved to a bowl or cup shape, like those structures seen on the adhesive pads of beetles. Small, arrayed cups would be advantageous because, as previously discussed, smaller and more numerous contact points benefit from the phenomena of contact splitting and crack trapping. These structures could also see the benefit of both van

der Waals forces and an enhanced suction force, giving rise to a greater adhesion force than that of conventional arrayed mushroom structures. Cups must be both sufficiently small and arrayed in a manner that reduces the effective modulus of the adhesive surface in order to provide intimate contact with the adherend surface. The modulus of the cup will also affect the amount of preload required to flatten or nearly flatten the structure against the adherend surface. If these geometric and load conditions were met, both van der Waals and suction forces would oppose loss of adhesion in the cups due to a tensile force on the stem. Furthermore, the tensile stretching force can be mediated by stretching of the cups' rims and stems, if the material has a sufficiently low elastic modulus [69,77].

A variety of single microscale suction cups was produced by Fischer and Grob; these structures are shown in Figure 2.9 [75].

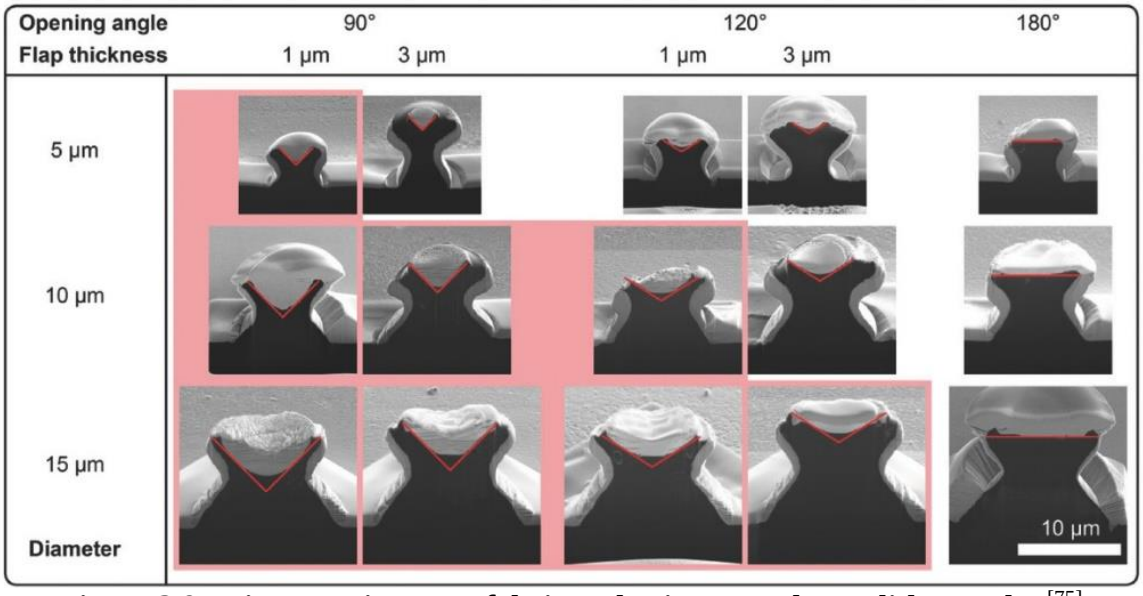

Figure 2.9. Micro-suction cups fabricated using two-photon lithography [75]

The flexibility of the cups was found to increase with higher ratios of cup diameter to cup thickness, which enabled the cups to attain high degrees of contact area with sufficient pre-

load. The pull-off stresses of these cups were found to greatly exceed the values seen in literature for comparable mushroom-shaped structures. It was theorized that the gradual contact formation from the edge of the cups toward the center during loading leads to a higher contact area than that of similar mushroom structures, and the initial elastic deformation of the cup could induce frictional forces that further increase adhesion. Although these suction cup structures seem to outperform conventional mushroom-shaped adhesive structures, the behavior of micro-suction cup arrays has not yet been reported. This is likely due to difficulties in fabricating complex and curved tip geometries in suitable materials at the micro-scale, which will be discussed later in this chapter [54,75].

2.3. Fabrication of Micro- and Nanoscale Polymer Surface Structures

A variety of methods found in literature employed to fabricate structured polymer surfaces at the micro- and nanoscale are herein discussed. Techniques for producing fibrillar structures with flat, mushroom, and concave tips with applications beyond that of dry adhesives are detailed. Common failure modes and barriers to process scale-up are then considered, followed by a discussion of common materials used in the production of structured polymer surfaces.

2.3.1. Fabrication Methods

2.3.1.1. Photolithography and Soft Lithography

By far the most common strategy for producing arrayed structures on polymer surfaces is through a combination of photo- and soft lithography using polymer resins, most commonly polydimethylsiloxane (PDMS), polyvinylsiloxane (PVS), or polyurethane (PU), and a photolithographically-prepared mold [24-26,45,56,78]. To fabricate a mold using photolithography, a substrate with a layer of photosensitive polymer, or photoresist, is partially exposed to ultra-violet (UV) irradiation through a pre-patterned mask. The resulting photoresist-patterned substrate is then typically subjected to a wet (chemical) or dry (plasma) etch that selectively removes portions of the substrate not protected by the patterned photoresist. Wet chemical etchants are generally isotropic, meaning they etch in all directions and can produce curved or angled sidewalls, while dry etchants are most often anisotropic, resulting in straight sidewalls [38-40].

Polymer substrates with structured surfaces can be then produced using molds prepared via photolithography. The most common method is to pattern and etch deep wells into silicon substrates, which can feature a differently patterned base to create high-AR polymer structures with alternate tip geometries. The holes are then typically filled with PDMS or another resin, which is then cured thermally or by UV irradiation, although there are some reports of replication with thermoplastics through the use of thermocompression molding [16,24,79]. The following sections describe polymer surface structures produced through both conventional and unconventional photo- and soft lithographic methods.

2.3.1.1.1. Flat- and Mushroom-Tipped Structures

The simplest fibrillar structure, that resembling a pillar with a constant diameter along the axis and flat top, can be fabricated with a photolithographically-prepared mold. The diameters and layout of the structures are defined by the initial photomask, and polymer surfaces patterned with fibril arrays have been reported in literature with structure diameters ranging from 100 nm to 500 μm. An array of 6-μm diameter fibrils produced by Aksak and Murphy using a photolithographically-prepared mold is shown in Figure 2.10 [27].

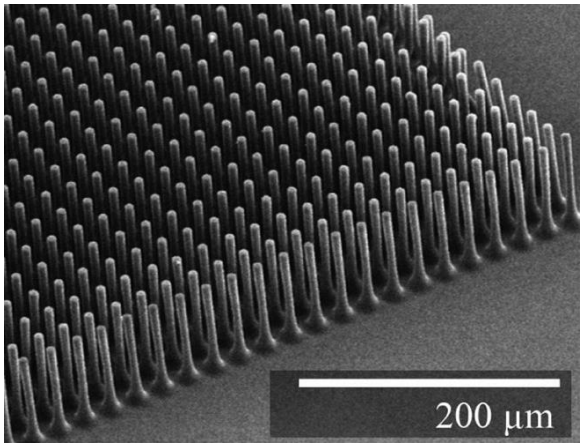

Figure 2.10. Molded polymer microfiber array [27]

The aspect ratio is defined by the diameter and the depth of the etch in the substrate. Higher-AR features are generally more difficult to demold, so the chance of fiber rupture or plastic deformation increases when the aspect ratio of the mold is increased [27,51,76,80,81].

Structured with overhanging "mushroom" caps are made with more complex molds than that of simple fibrils. The cap can be achieved by generating a mold with undercut holes either by using combinations of anisotropic and isotropic etches, exploiting the

footing effect that occurs during deep reacting ion etching (DRIE), or exposing both sides of a photoresist layer with different masking on a UV-transparent substrate. While these methods are among the most common seen in literature for fabricating mushroom-shaped polymer surface structures, this list is by no means exhaustive. A variety of photolithography-based methods for fabricating intricate geometries exists, each with varying degrees of complexity [2,3,32,34,35,82,83].

A combination of photoresists and different etchants was used by Sameoto and Menon [84] in the process depicted in Figure 2.11, in which photoresist was spun on a layer of polymethylglutarimide (PMGI) [84].

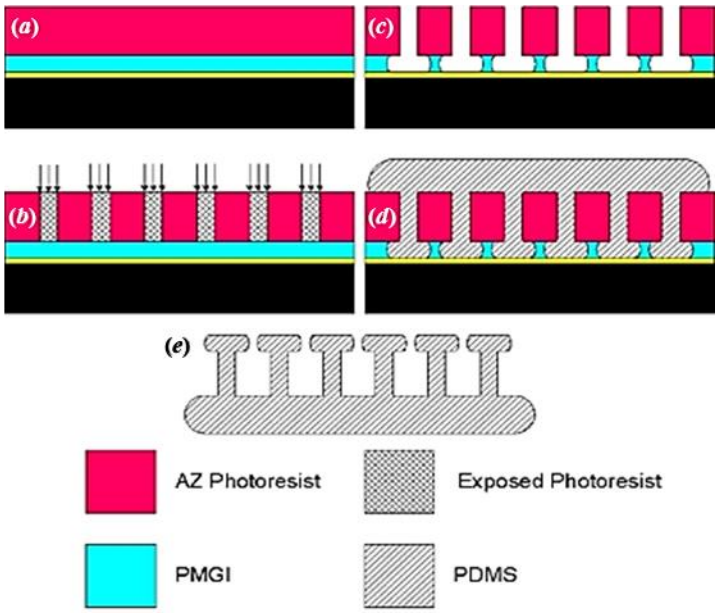

Figure 2.11. Molding process for mushroom-tipped structures: spinning PGMI and photoresist (a), photoresist exposure (b), photoresist development and etch (c), and PDMS molding (d-e) [84]

After the photoresist was exposed and developed, the PGMI was isotropically wet-etched to form a desired undercut. The mold was then filled with PDMS and cured to yield structures depicted in Figure 2.12 [84].

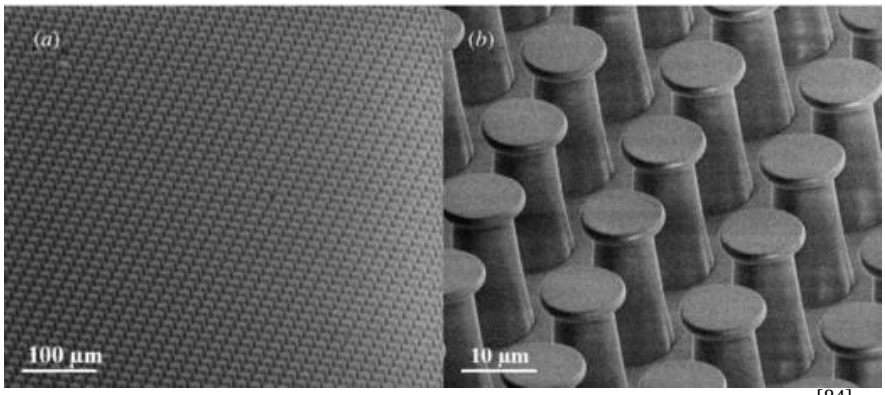

Figure 2.12. Mushroom-tipped molded PDMS structures [84]

Lateral etching or "footing" can also occur during DRIE, a common dry etching technique, when the etching front reaches an oxide interface. As shown in Figure 2.13, DRIE will etch silicon anisotropically, yielding straight sidewalls, and it will begin to etch laterally at the silicon/silicon oxide interface [85,86].

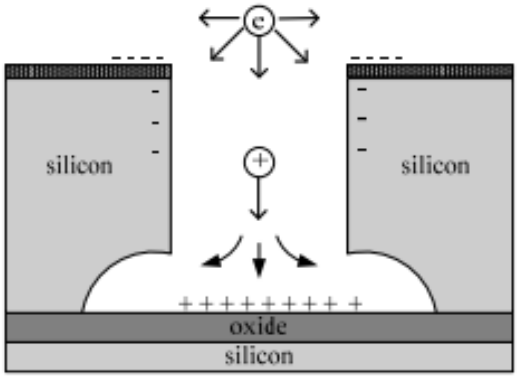

Figure 2.13. DRIE footing effect [86]

The footing effect in DRIE has been exploited by numerous researchers to fabricate mushroom-shaped polymer structures for dry adhesion. The diameters of the stems and overhanging caps can be controlled by the mask used and etching conditions [2,3,28,82]. Kim and Park used DRIE and the footing effect to produce a variety of mushroom structures with different aspect ratios and top diameters as shown in Figure 2.14 [35].

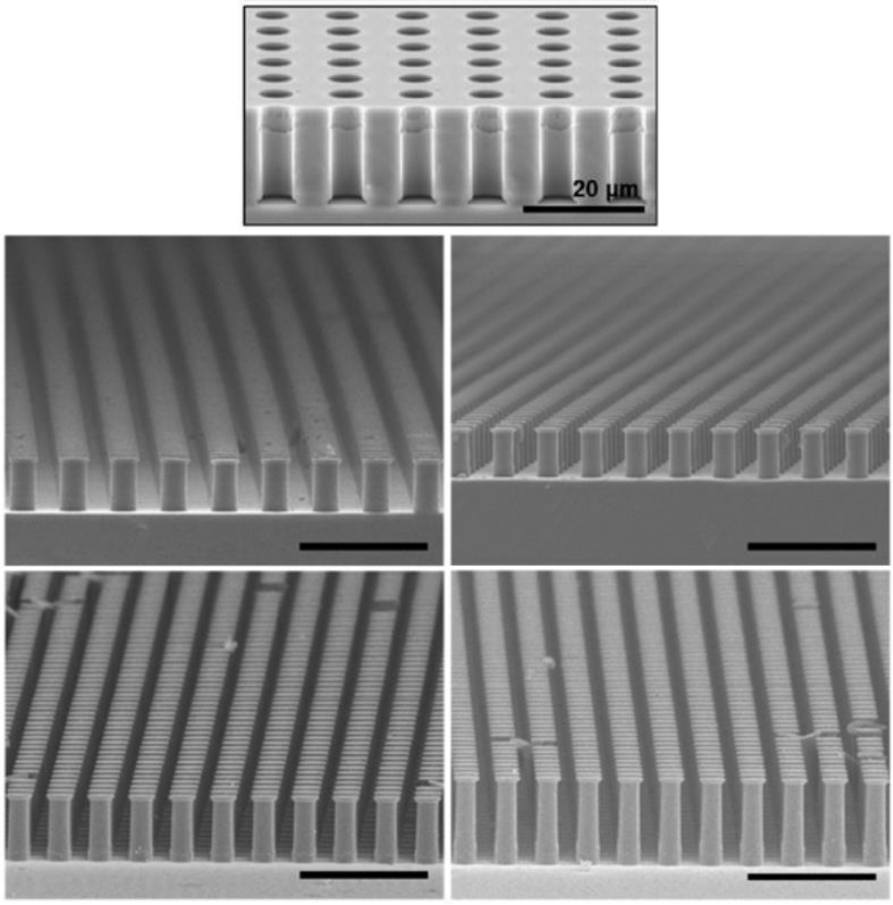

Figure 2.14. Silicon mold (top) produced using DRIE and resulting PDMS structures (bottom) (scale bars are 40 µm) [35]

Unique tip architectures can also by fabricated using photolithography by patterning photoresist on a UV-transparent substrate such as quartz or soda lime glass and exposing the photoresist on both sides with different masking on either side. Wang and Hu

spun a thick layer of positive photoresist on a glass substrate and partially exposed the top surface to UV light through a photomask. The bottom of the photoresist was then exposed briefly to UV light without a photomask through the glass substrate. Areas closer to the substrate in this case were more exposed, which resulted in slanted or undercut holes under photoresist pillars after development. PDMS was then used to make positive replicas of the holes in the photoresist. The diameter and height of the stems and overhanging caps could be changed by altering the photomask, photoresist thickness, substrate exposure time, and development time. The process is depicted in Figure 2.15 along with a variety of resulting mushroom-tipped structure arrays [32].

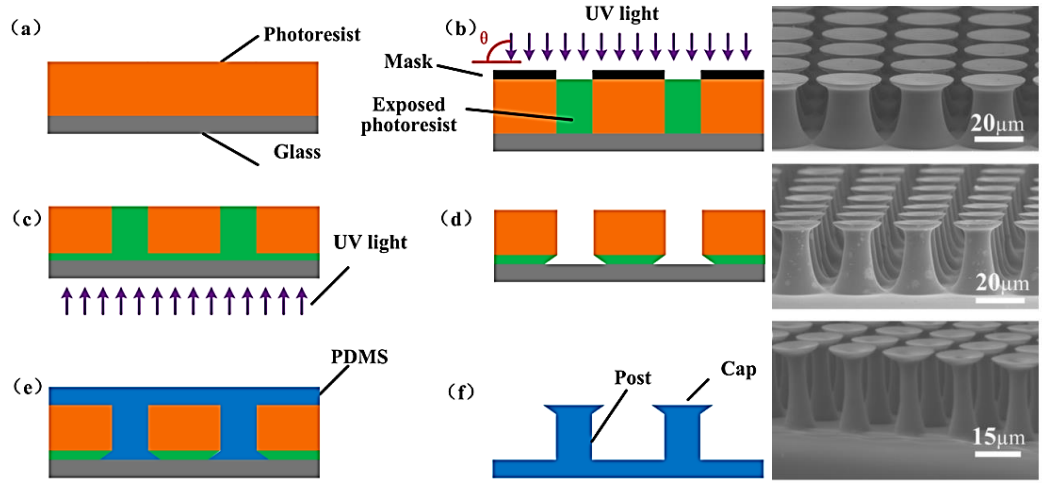

Figure 2.15. Preparation of photoresist mold and PDMS structures using dual-side exposure (left): photoresist and baking (a), photoresist top exposure with mask (b), photoresist back exposure without mask (c), photoresist development (d), PDMS molding (e-f); and resulting structures (right) [32]

2.3.1.1.2. Concave-Tipped Structures

While there are abundant reports in literature on photolithography and molding-based fabrication methods for pillar-like and mushroom-tipped structures, the production

of high-AR structures terminating in bowl or cup shapes is exceedingly rare. There have been reports of multi-part molds for producing such structures arrays at relatively large (hundreds of microns to millimeters) scales [77,87], but there are currently no reported methods for reliably creating these structures in the same size range as that of mushroom-based adhesive structures. Some groups have reported methods for patterning polymer surfaces with concave wells or depressions to produce octopus or other cephalopod-inspired suction-based adhesives. These patterns are typically made by photolithographically patterning and molding from arrays of microlenses, which can be achieved by patterning photoresist pillars on a substrate and reflowing them to create a curved shape [88]. Arrays of concave wells with raised perimeters have also been fabricated by patterning holes in a rigid substrate and pouring a liquid polymer precursor over the holes while trapping air, resulting in raised cups. This process and the resulting structures, reported by Baik and Kim, are shown in Figure 2.16 [89].

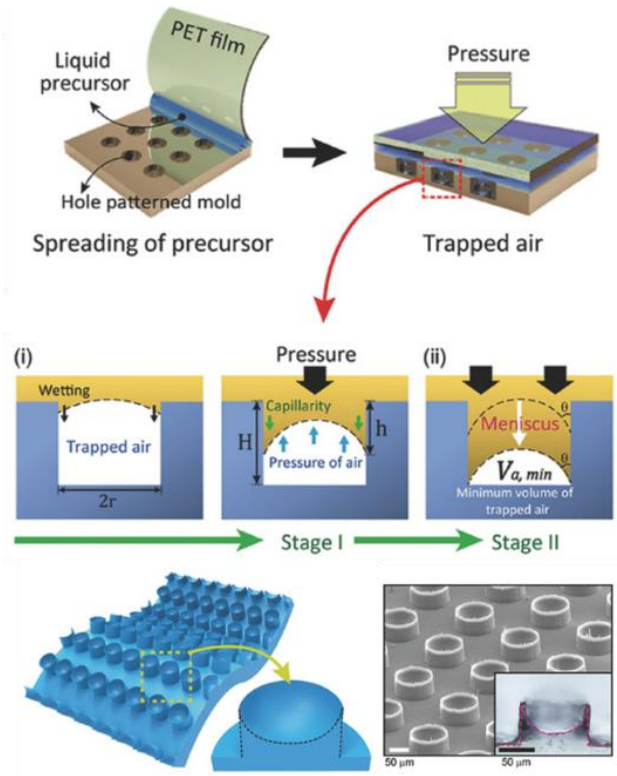

Figure 2.16. Concave structure patterning process using trapped air: trapping air to form meniscus (Stage I) and applying pressure to define cup height (Stage II) [89]

Similar structures were reported by Thanh-Vinh and Takahashi, in which photoresist was spun onto a surface patterned with microlenses. The photoresist was exposed to UV light through the substrate and microlenses, which left the lens shape with a slanting hole array after development. The resulting molded structures were similar to those shown by Baik and Kim and were 100-250 μm in diameter [90].

Narrow stemmed structures with concave tips were prepared photolithographically by Wienhold and Kraemmer in a patterning and etching process shown in Figure 2.17 with the resulting structures [41].

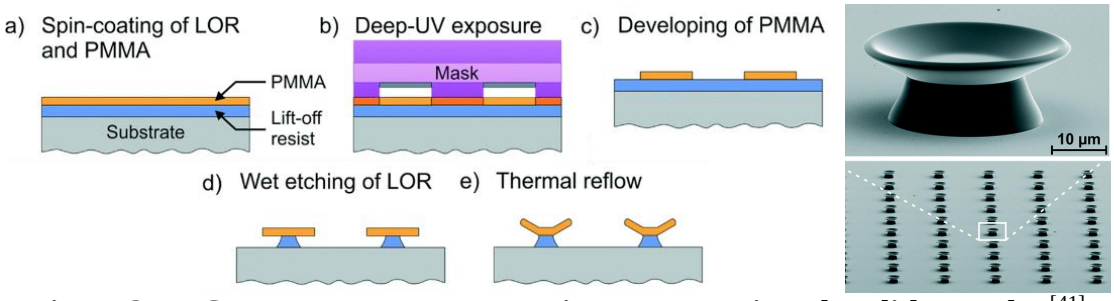

Figure 2.17. Concave structure patterning process using photolithography [41]

Poly (methyl methacrylate) (PMMA) disks were first patterned on a layer of photoresist on a silicon substrate. The photoresist was wet etches to give undercut stems, and after development the samples were heated to soften the PMMA and cause it to deform into a bowl-like shape. The resulting structures were rigid and were not used as dry adhesives, but as whispering-gallery mode resonators for biosensing. Any use of this fabrication method for different applications has not been reported.

2.3.1.1.3. Angled Structures, Inking, and Successive Molding

High-AR fibrillar arrays can also be fabricated photolithographically in which the axis of the fibers is non-perpendicular to the substrate. These structures can be produced by patterning an array of holes on a substrate and using a dry etch technique with the patterned substrate at a tilt with respect to the etchant source, or the photoresist can initially be exposed through a photomask with the UV source at an angle to the substrate [2,27,32,91]. Fibrillar arrays with structured tips can also be produced without initially patterning the tip shape in the mold. In this process, known as "inking," straight or tilted fibers molded from a photolithographically-prepared mold are dipped into a thin film of polymer precursor. The fibers with wetted tips can then be pressed on another substrate and cured, resulting in

flat, mushroom-like tips that exhibit anisotropic adhesion [2,28,29,32,37,54,82]. This process and resulting structures, produced by Murphy and Aksak, are depicted in 2.18 [36].

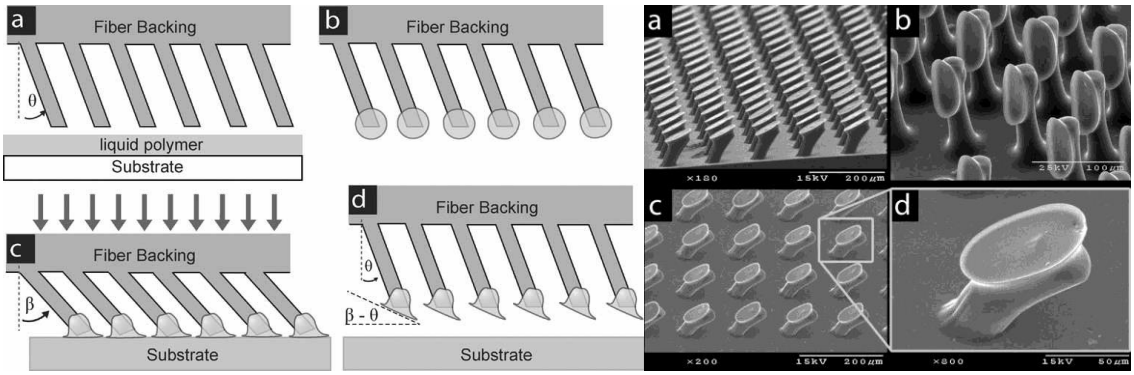

Figure 2.18. Preparation of angled mushroom-tipped fibrils (left): liquid polymer spun on substrate (a), bare, angled fiber tips dipped into liquid and retracted (b), fibers pressed onto substrate and cured (c), and cured fibers removed from substrate (d); and resulting structures with varying tilt angles (right, a-d) [36]

Hierarchical structures like those seen on the gecko can be produced using the aforementioned methods by adding successive molding steps with dual level molds. Microscale structures are often first patterned and used as the substrate for molding nanoscale patterns, as shown below [2,25,32,92]. Mushroom structures, shown in Figure 2.19, with three levels of hierarchy were produced by Murphy and Kim using this technique [93].

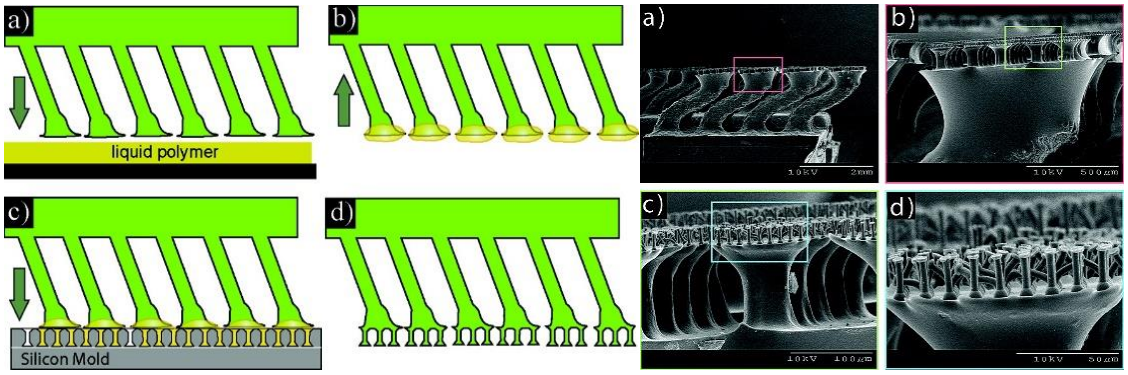

Figure 2.19. Preparation of hierarchical mushroom tips (left):liquid polymer spun on substrate (a), mushroom-tipped fiber dipped in liquid and retracted (b), fiber array placed on etched silicon mold and cured (c), hierarchical array removed from mold (d); and resulting structures at various levels of hierarchy (right, a-d) [93]

2.3.1.1.4. Alternative Photolithographic Methods

Outside of the traditional photolithographic methods using a photomask and UV irradiation, micro- and nanostructures can be fabricated by etching rigid substrates or exposing resin to a curing source in different manners. Colloidal lithography uses monolayers of spheres, either closely packed or distributed in a desired pattern, as an etch mask rather than a patterned photoresist. The spheres etch along with the substrate and act as a sacrificial mask. Curved, angled, or straight sidewalls can be obtained in the underlying substrate depending on the etch rate of the spheres used relative to that of the substrate [94]. Chen and Yang fabricated octopus-inspired nanosucker arrays using colloidal lithography and a series of molding steps. A close-packed layer of 250-nm diameter silica spheres was coated on a film of ethoxylated trimethylolpropane triacrylate (ETPTA) on a silicon substrate and subjected to a reactive ion etch. The etch rate of the ETPTA was much higher than that of the silica spheres, so the spheres protected part of the polymer film from being immediately etched. This partial etch of the ETPTA layer and silica spheres resulted in

sphere-tipped structures with silica tips and polymer stems. A polyvinyl alcohol (PVA) solution was then cast over the structures and peeled off after drying, causing the silica spheres to separate from the polymer stems. PDMS was then cast onto the PVA film with embedded silica spheres to create an array of nanosuckers that were replicas of the ETPTA nanostems, being wider at their base and having a concave top surface. These structures at each step of the process are shown in Figure 2.20 [95].

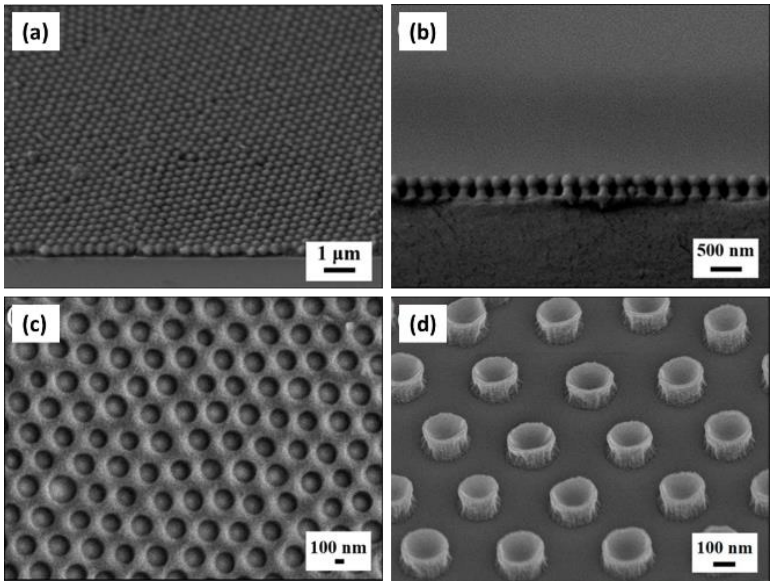

Figure 2.20. Concave structure patterning process: silica sphere layer (a), silica caps and ETPTA stems after etching (b), PVA film with embedded silica spheres (c), and molded PDMS nanosucker array (d) [95]

The funnel or suction cup microstructures reported by Fischer and Grob, shown in Figure 2.9 (section 2.2.3.2), were fabricated using two-photon lithography, a method used for fabricating complex structures with sub-micron resolution. This process uses a focused femtosecond near-IR laser to photo-induce polymerization in polymer resin at the laser's focal point. A desired 3D structure is built by successively exposing or "writing" 2-dimensional layers of resin cured in a specified pattern. The uncured resin is removed after

the entire structure is written, making the process analogous to negative-tone lithography or stereolithographic 3D printing. While two-photon lithography can be used to fabricate unique architectures at a micro- or nanoscale, the build volume is usually limited to under a cubic millimeter, resulting in a very low throughput [75,96].

2.3.1.2. Electrohydrodynamically-Induced Instabilities

Another non-photolithographic method that has been used to pattern polymer surfaces for a variety of applications is to induce electrohydrodynamic (EHD) instabilities on a polymer film. When placed in a strong electric field between two capacitor plates or electrodes, a polymer film experiences an electrostatic stress at the interface between the polymer and air due to a mismatch in their dielectric constants. This stress, along with thermal fluctuations, induces small magnitude capillary waves in the polymer film if it is above its glass transition temperature (T_g), and the minima and maxima of those waves experience slightly difference electric field strengths. In a sufficiently strong electric field, the capillary wave maxima, where the distances between the polymer film and the top electrode are the smallest, can eventually be drawn upward to make contact with the top electrode. The wavelength of the instabilities in the film and the ability of the polymer to be drawn upward is dependent on the competition between surface tension forces and the electrostatic stress imparted on the polymer. The process can also be performed on an uncured resin, which is cured thermally or by UV after instabilities are induced [97-101].

These instabilities can be encouraged by either patterning the polymer or the top electrode before imposing an electric field, as the field and resulting destabilizing forces

on the film will always be strongest where the gap between the polymer and the top electrode is the smallest. EHD instabilities have been used to pattern a wide range of thermoplastic polymers and resins, with the most common being PMMA, polystyrene (PS), polyvinylidene fluoride (PVDF), and UV-curable acrylate resins [97,102-106]. After making contact with an upper electrode, destabilized polymer films will begin to spread transversely on the electrode through a phenomenon known as electrowetting. Many researchers have used EHD instabilities and electrowetting to fabricate high-AR mushroom-tipped structures for use in dry adhesives [2,107,108]. Hu and Tian produced mushroom-tipped arrays by hot embossing a PMMA film and drawing the embossed features upward toward a top flat place in a strong electric field. The drawn micropillars spread on the electrode surface, and the extent of spreading was found to depend on the applied voltage. The process is shown in Figure 2.21 [31].

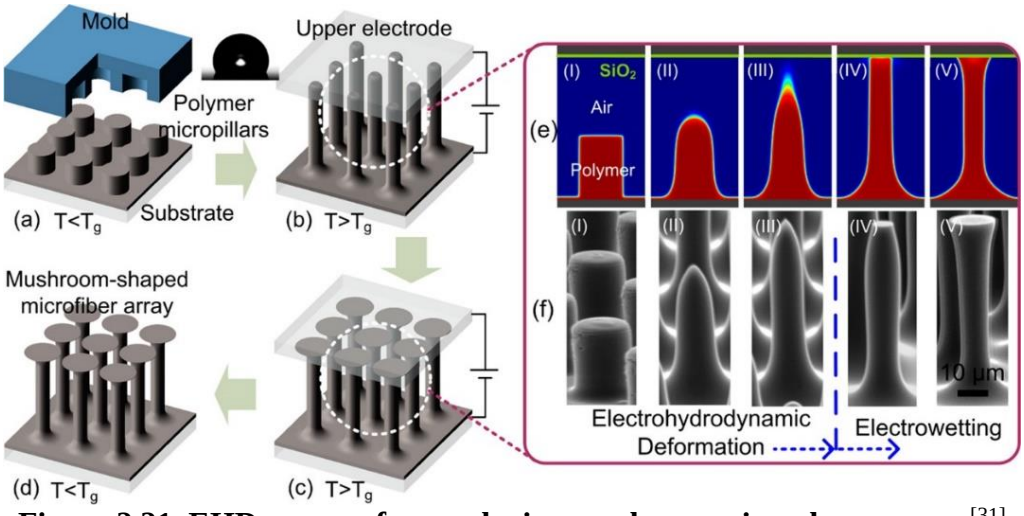

Figure 2.21. EHD process for producing mushroom-tipped structures [31]

2.3.1.3. Drawing Lithography

Drawing uncured liquids or molten polymers can also be achieved by mechanical or contact means. The drawing of polymeric fibers or filaments is a well-established manufacturing process, but applying these drawing methods to other 3-dimensional structures is a relatively new area of interest. This technique, which is referred to by multiple names in literature including direct drawing, liquid bridge process, and, most often, drawing lithography, has been most widely used for producing microneedles as an alternative to oral medication and conventional syringes for drug delivery. Microneedles are typically produced via drawing lithography by heating a thermoplastic polymer film above its melting temperature. A patterned substrate is then brought into contact with the molten film, and the system is then cooled, increasing the polymer's viscosity. The pattern is then raised at a fixed rate, pulling with it the wetted polymer and forming columns that are thinned and stretched as the pattern continues to rise. Drawing the polymer structures before, after, or during, cooling to specified temperatures allows one to tailor the evolution of the structure diameter along its axis. Once the pattern reaches the desired height, the system is cooled below the glass transition temperature of the polymer, and further ascension of the pattern breaks the polymeric bridges at their smallest diameter, resulting in sharp tips. This process can also be performed with a viscous polymer resin that can be cured after drawing by UV irradiation or some other means [109].

While the drawing of microneedle arrays has become a fairly well-established technique, with multiple clinical trials underway [110,111], there are very few applications of drawing lithography in literature to create polymer structures or tip geometries other than

sharp, needle-like projections [112]. Spina and Stefanini reported the fabrication of arrays of microhooks by drawing pointed structures and performing a subsequent heat treatment to allow the tips to sag or curl over to one side [113]. Paek and Kim used the technique to product high-AR PDMS micropillars with microspheres at their tips. Glass or PMMA microspheres ~50 μm in diameter were first assembled on a photolithographically-patterned SU-8 grid and transferred onto a double stick tape on a glass substrate. The microsphere array was lowered to contact the uncured PDMS film, and the array was raised upward at a specified rate while heat was applied to cure the PDMS. The group saw a spread in the height and diameters when drawing 4x4 arrays of structures, which was attributed to uncertainty in the depth of the microspheres' immersion in the uncured PDMS and probable tilting of the microsphere array with respect to the PDMS. Any deviation from parallelism between the microspheres and the PDMS changed the immersion depth of the spheres and the final geometry of the drawn structures [114].

Regardless of the target geometry, there are common processing parameters across all drawing lithography techniques that affect the final structures. The temperature of the system at the time of drawing determines whether a thermoplastic polymer is in the solid, glassy, or liquid state, or the degree of curing in a polymer resin. Fabrication of predictable and repeatable structures through drawing lithography requires an intimate knowledge of the relationships between the polymer's viscosity and surface tension with temperature, as well as the dependence of viscosity on the drawing rate. In the glass transition, that is, between T_m and T_g, the shear viscosity of polymers often shows a stronger-than-Arrhenius increase in response to the decreasing temperature, termed super-Arrhenius behavior. The shear viscosity-temperature relationship of polymer melts can be fitted by the Vogel-

Fulcher-Tammann (VFT) equation (Equation 1.1), in which A is a temperature-independent constant and T_0 is the ideal T_g of the polymer.

$$\eta_s \sim e^{\frac{A}{T-T_0}} \tag{1.1}$$

This equation implies that there is an exponential increase in shear viscosity as a molten glassy polymer approaches T_0. For this reason, the patterned substrate is brought into contact with the polymer above its melting temperature. Drawing typically begins above the polymer's T_m but can continue during cooling between T_m and T_g. Below the glass transition, further drawing can either cause the polymeric bridge to fracture at its narrowest point, or it can be used to detach the patterned substrate from the drawn structures [109].

Parameters such as the target height and the drawing rate also have a strong effect on structure, as deformation stress and deformation rate of a polymer in uniaxial flow are the core parameters that influence the polymer's deformation mechanism. A polymer's extensional viscosity, which describes its resistance to extensional deformation, is defined in Equation 1.2 as the extensional tensile stress divided by the extension rate.

$$\eta_E(t) = \frac{\tau_E(t)}{\dot{\varepsilon}} \tag{1.2}$$

An exemplary plot of the relationship between the shear viscosity and temperature of a thermoplastic polymer is shown in Figure 2.22, along with a depiction of the drawing lithography process.

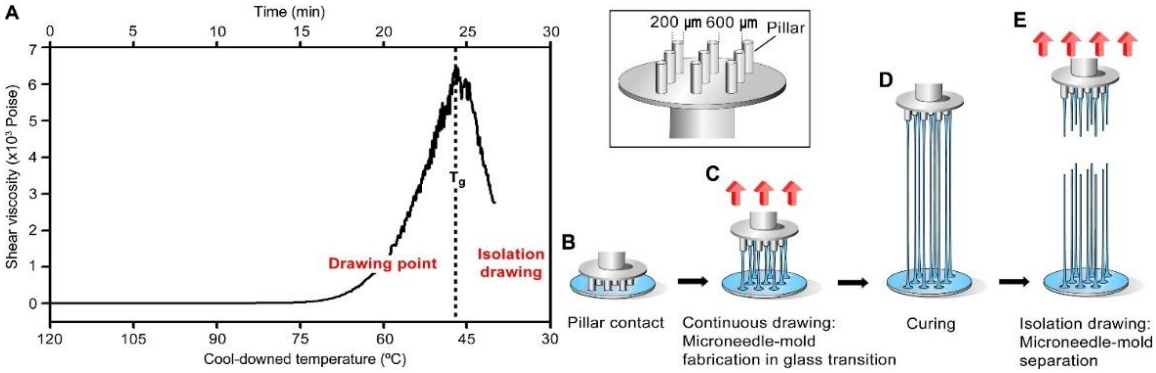

Figure 2.22. Shear viscosity-temperature plot (left) and drawing lithography procedure (right) [109]

Depending on the type of material used, the temperature of the polymer film substrate, the temperature of the pattern, and the draw rate, among other factors, the number of needle profiles that can be created using drawing lithography is nearly limitless, as demonstrated in Figure 2.23 [58,109,115-117].

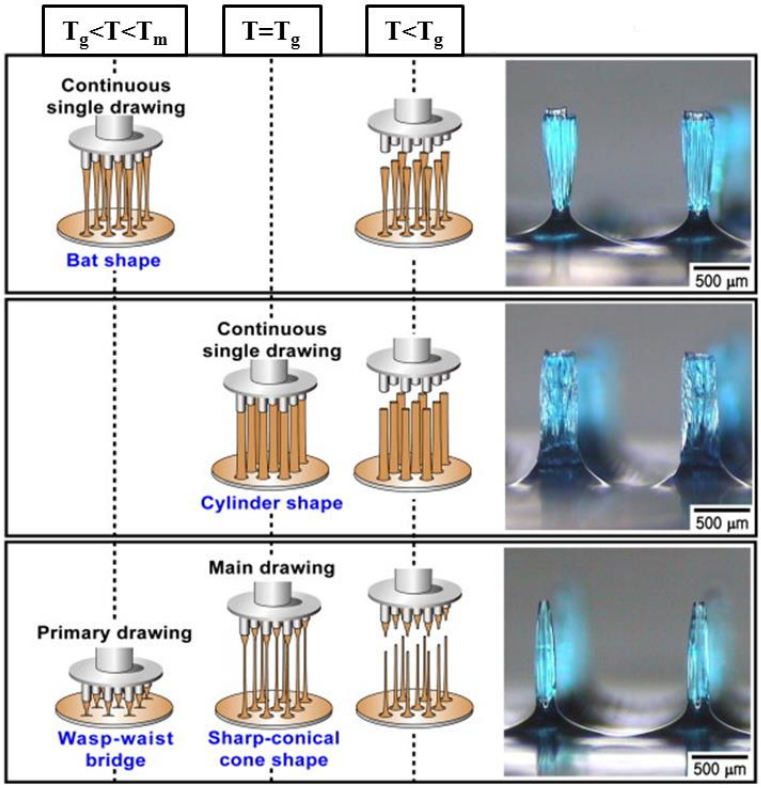

Figure 2.23. Structures produced from varying drawing lithography procedures [109]

2.3.2. Process Scaling and Material Considerations

Despite the growing interest in bio-inspired polymer structures fabricated through photolithography and molding techniques in academia, these materials are unlikely to see commercial success in the near future due to limitations in current manufacturing practices. Producing large areas of structures molded from photolithographically-prepared templates is prohibitively expensive due to the high cost of working in microfabrication or cleanroom environments. This not only includes facility or equipment costs, but the expenses of masks, substrates, and raw materials as well. Furthermore, the largest silicon wafers typically available are 100 mm in diameter, severely limiting the area of a polymer with surface structures that can be used at one time. While some work has been done on the lab-

scale to develop a continuous fabrication system with a rolling mold and UV exposure system [118], the fabrication method of those detailed in section 2.3.1 most likely to be scaled up is drawing lithography. Drawing lithography is relatively simple in comparison to other nano- and microfabrication methods, employs mild processing conditions, and can accommodate a wide range of polymers [26,34,45,78,109].

While silicone rubbers and similar UV or thermally curable resins are attractive because of their high fidelity in molding, thermoplastics are generally attractive from a manufacturing point of view both because they can be solidified from a melt much faster than most curable materials and because they are recyclable. Thermoplastics are most appropriate for inexpensive or disposable products, while silicones are often used for long-term, durable products, so the intended application clearly should influence the material choice when fabricating structured polymer surfaces [45]. Currently the most common materials used to fabricate such surface structures for bio-inspired dry adhesive applications are PDMS, PVS, and polyurethanes [24,74,78]. However, high-AR structures comprised of these low modulus materials are highly prone to structural collapse, yielding, and fatigue after repeated use. Arrayed structures composed of a higher modulus material like that of the gecko foot's β-keratin are more durable than their silicone or polyurethane counterparts and can withstand a higher degree of cyclic loading. They can exhibit the same adhesive performance as a low modulus material if their geometry were to be optimized in such a way that they have similar effective moduli and establish a high contact area with the adherend [58,81,119].

As discussed in section 2.3.2.2, a high-AR microstructure terminating in a concave bowl shape could be a more effective dry adhesive structure than the conventional

mushroom-shaped dry adhesives commonly produced on the lab scale out of PDMS through photo- and soft lithography. In the following chapters, a new process is presented to fabricate these structures in a range of sizes and materials. This process, termed "drawcasting," is a modification and new application of the potentially scalable and facile drawing lithography technique.

CHAPTER 3. DRAWCASTING PROCESS

As discussed in Chapter 2, few of the available methods for fabricating polymer surfaces with high-AR structure arrays are scalable, cost-effective, or amenable to multiple types of polymers or structure geometries. The drawcasting process is herein presented as a means to fabricate arrays of polymer surface structures in a repeatable, predictable, and relatively facile manner. Each aspect of the drawcasting system is detailed in order to explain the steps and processes involved in producing surface structure arrays. Structures with a concave tip, henceforth referred to as micro-suction cups, with applications as dry and reusable adhesives, are the focus.

3.1. Process Description and Preparation of Drawcasting Elements

Drawcasting is an extensional deformation process in which templated patterns are drawn from a viscous or viscoelastic phase of a parent material such as a thermoplastic film or a polymer resin. A patterned template is first lowered to a specific depth in a viscous (resin) or molten (thermoplastic) precursor, forming a meniscus on the patterned surface. The template is then raised to a specified position, forming capillary bridges from the precursor material. A phase transformation is then induced through curing (resin) or cooling (thermoplastic), and the pattern is removed to yield an array of three-dimensional structures on the surface of the parent material. In this work, thermoplastic polymer films were used with patterns of arrayed hemispheres to draw micro-suction cups on various length scales. The drawcasting process is depicted schematically in Figure 3.1.

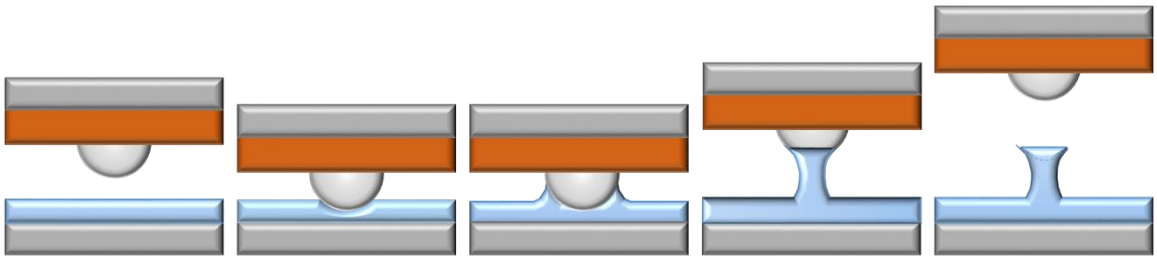

Figure 3.1. Drawcasting process

The drawcasting system consists of three fundamental elements: a heated pattern, a polymer film, and a heated base. A thermoplastic polymer film is typically heated above its melting temperature (T_m) on a substrate positioned below a hemispherical pattern, as shown in Figure 3.2.

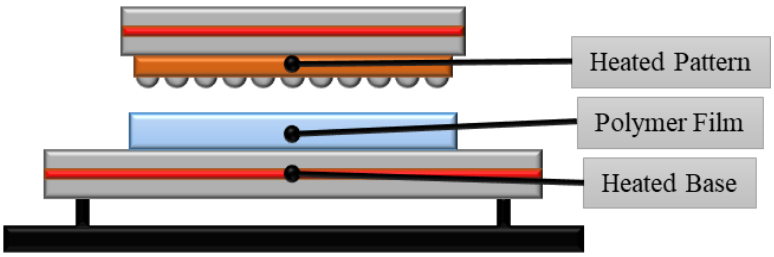

Figure 3.2. Drawcasting elements

The heated pattern is attached to a linear motor such that the height of the pattern with respect to the polymer film as well as the velocity of the pattern when being raised or lowered can be precisely defined. The following sections discuss the preparation of the drawcasting elements as well as supplemental fixtures and processes that were developed to aid in drawcasting.

3.1.1. Polymer Film Press

Prior to being placed on the heated base, a thermoplastic film is pressed to a defined thickness using a film press consisting of two heated platens in a hydraulic press. Steel shims of various thicknesses were produced to place between the two platens with polymer pellets in order to dictate the thickness of the resulting film. This film press is shown in Figure 3.3.

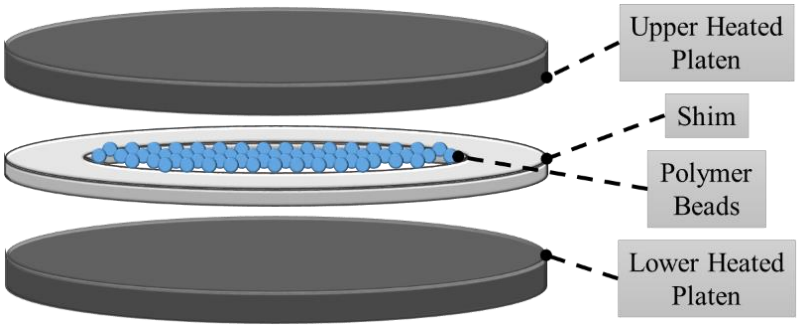

Figure 3.3. Polymer film press

Generally, films are pressed to thicknesses well above the diameter of the pattern with which they are to be used in order to avoid additional resistance to drawing due to volume depletion or interaction with the base. For example, films used with 500-µm diameter patterns are typically pressed to thicknesses of 650 µm or larger. Uniform films with parallel faces are crucial in drawcasting, as deviation from uniformity will affect the volume of polymer interacting with a given pattern, resulting in a nonuniform structure array. To press a polymer film, the upper and lower platens were heated to 200 °C, and the assembly was pressed under roughly 3.45 MPa for 5 minutes. The assembly was then allowed to cool passively under pressure, and the thickness and uniformity of the films were assessed using a micrometer before use in drawcasting.

3.1.2. Pattern Fabrication

A number of hemispherical patterns in varying sizes have been prepared for drawcasting of micro-suction cup arrays. Three distinct processes were developed in order to fabricate patterns with structure diameters ranging from 3 mm to 50 µm.

3.1.2.1. Ball Bearings

The largest hemispherical patterns, those with 3-mm diameter hemispheres, were fabricated using pre-purchased stainless-steel ball bearings (McMaster Carr). The ball bearings were arranged on an aluminum plate that was micromachined with an array of depressions and through-holes. The ball bearings were arranged to sit in the depressions and were held in place with epoxy, applied to the back side of the aluminum plate. This process is depicted in Figure 3.4.

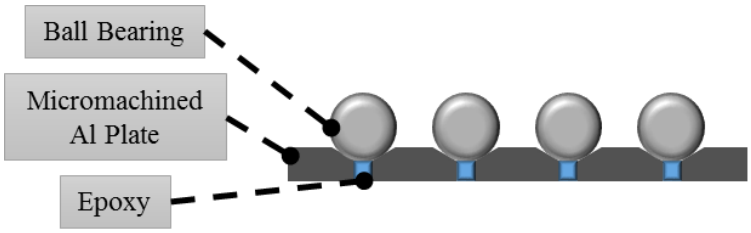

Figure 3.4. 3-mm diameter ball bearing pattern fabrication

The pattern was then attached to a heater and used as the upper heater in the drawcasting process. An example of the 3-mm diameter ball bearing pattern is shown in Figure 3.5.

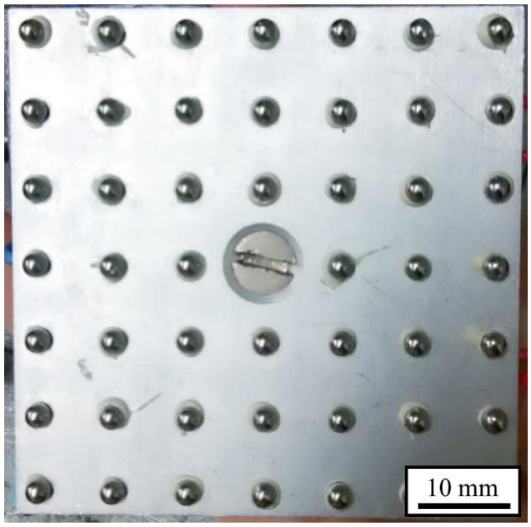

Figure 3.5. 3-mm diameter ball bearing pattern

3.1.2.2. Ball Grid Arrays

In order to fabricate upper patterns with smaller diameters, a second process was developed due to limitations in the attainable sizes of ball bearings. Ball grid array (BGA) preforms, which are arrays of tin/silver/copper alloy solder spheres adhered to a polyimide backing, were purchased with either 500 or 250-μm diameter spheres (EZ-Reball). Copper plates were photolithographically patterned with arrays of holes corresponding to the size and spacing of the BGAs. Solder flux was then applied to the patterned copper plates, and the BGA preforms were aligned to the plates. The preforms and plates were heated to 230 °C, allowing the solder to melt and reflow to fill the holes in the photoresist pattern. The polyimide preform backing was then removed, allowing the hemisphere-patterned copper to be used as the upper heated pattern in drawcasting. This fabrication process is depicted in Figure 3.6, and examples of resulting 250- and 500-μm diameter BGA patterns are shown in Figure 3.7.

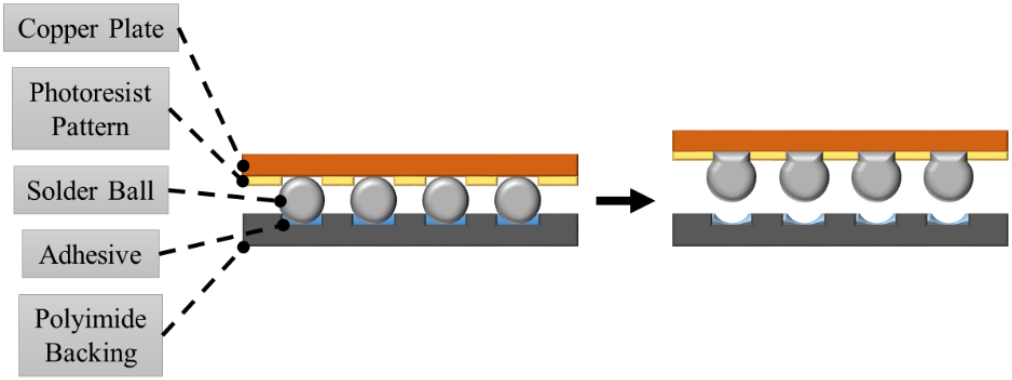

Figure 3.6. BGA pattern fabrication process

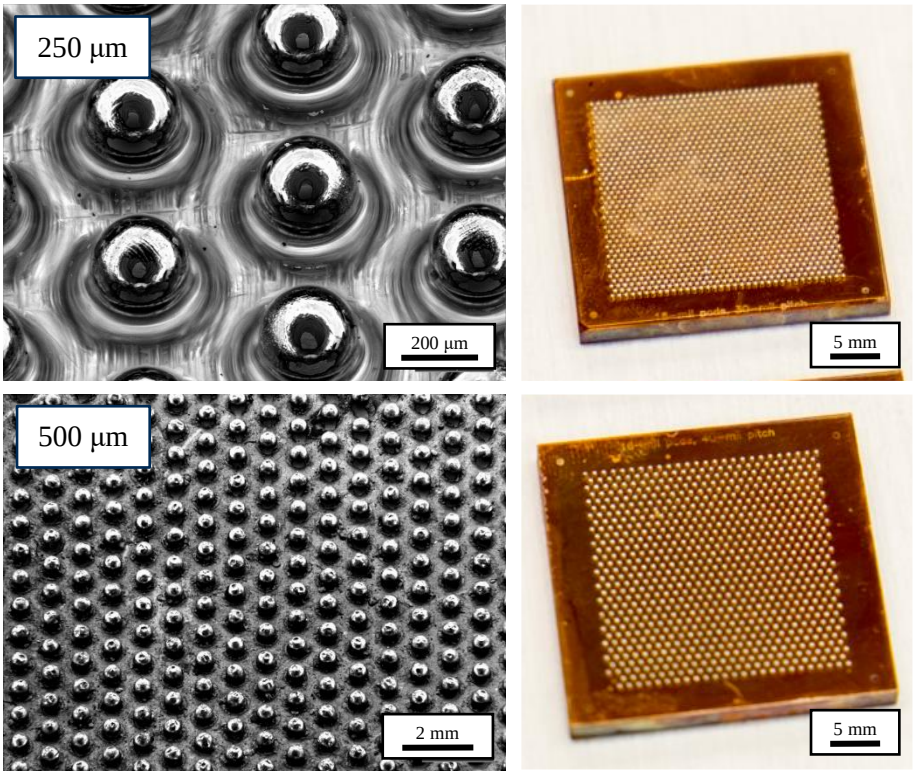

Figure 3.7. 250 (top)- and 500 (bottom)-µm diameter BGA patterns on Cu

3.1.2.3. Rounded Micropillars

A third and final process was developed in order to fabricate arrays of hemispheres equal to and lower than 250 μm in diameter, as artefacts on the surface of the reflowed solder balls such as dendrites limit their smoothness and become increasingly problematic at smaller scales. An array of photoresist pillars (AZ 40XT-11D, Microresist Technologies) was first patterned on a silicon wafer using a mask consisting of arrays of holes with defined diameters and spacing. After exposing and developing the photoresist, the silicon wafer was heated to 150 °C for one hour, allowing the photoresist caps to reflow and form hemispherical caps or lens-like shapes on the surface of the wafer. This temperature was chosen to ensure softening and reflow of the photoresist while avoiding excessive lowering of its surface tension and viscosity, which could allow it to spread on the wafer's surface. The silicone wafer was then dry etched using inductively coupled plasma (ICP), with the photoresist lenses behaving as an etch mask. The etch rates were defined such that the resulting pillars were 100-150 μm in height. The diameter of the silicon pillar and photoresist cap is determined by the original photomask, while the radius of curvature (R_c) of the caps is defined by the thickness of the photoresist layer. Figure 3.8 shows scanning electron microscope (SEM) images of rounded silicon/photoresist micropillar arrays with diameters of 50, 100, and 250 μm.

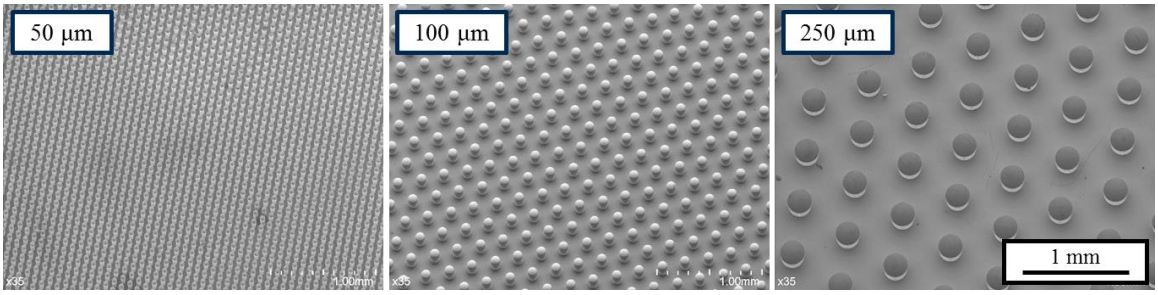

Figure 3.8. 50-, 100-, and 250-µm diameter Si pillars with rounded photoresist caps

The thickness of the photoresist layer was held constant for each diameter of micropillars such that the resulting radius of curvature and height of the curved caps was the same for each respective diameter. The photoresist thickness and corresponding radii of curvature and cap heights of each size of rounded micropillar fabricated are given in Table 3.1.

Table 3.1. Rounded Micropillar Geometries

Pillar Diameter (µm)	Photoresist Thickness (µm)	R_c (µm)	Cap Height (µm)
250	40	142.6	74
100	15	59.8	27
50	7	30.5	13

PDMS was then cast over the rounded pillars, cured, and removed. In order to obtain a PDMS mold with parallel faces, ensuring that all of the pillar depressions would lie in the same plane as the top and bottom of the mold, a molding fixture was constructed. The fixture consisted of a base to hold the patterned silicon wafer, spacers to define the mold thickness, and a compressive ring and plate along with a compressible gasket. This fixture is depicted in Figure 3.9.

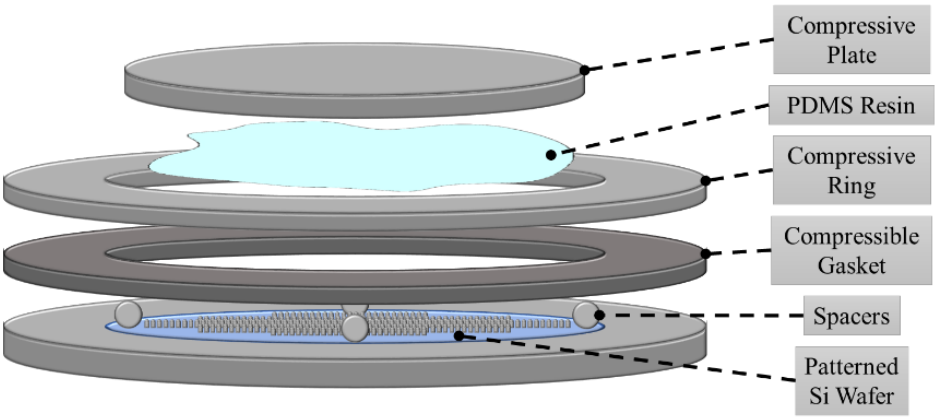

Figure 3.9. PDMS molding fixture

A thermally curable high-temperature epoxy (EpoTek 377) was then cast into the PDMS mold, and a glass slide was placed on top of the setup to act as a substrate. After curing, the PDMS was removed, yielding epoxy replicas of the rounded silicon/photoresist micropillars on glass substrates. The full rounded micropillar fabrication process is depicted in Figure 3.10, and epoxy micropillars on glass substrates are shown in Figure 3.11.

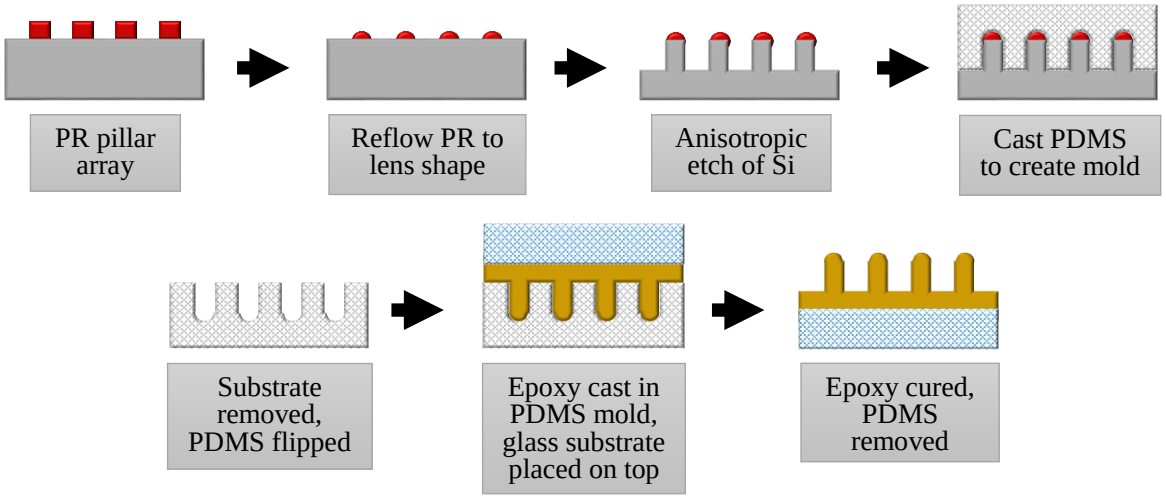

Figure 3.10. Rounded micropillar pattern fabrication process

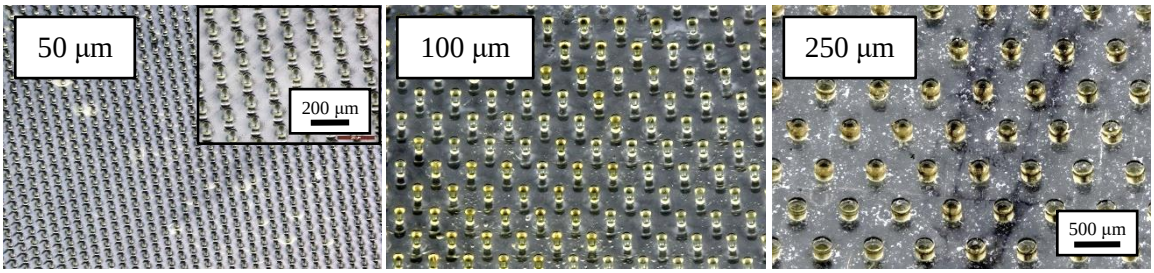

Figure 3.11. 50-, 100-, and 250-µm diameter epoxy rounded micropillar patterns

The three pattern fabrication methods and corresponding attributes are listed in Table 3.2.

Table 3.2. Pattern Fabrication Methods

	Ball Bearings	Ball Grid Arrays	Rounded Micropillars
Array size	Limited to size of aluminum plate	27x27 mm	Limited to size of silicon wafer
Hemisphere Diameter	3 mm	250-500 µm	50-250 µm
Diameter Lower Limit	1.6 mm [120]	250 µm	1-5 µm
Processes	Micromachining and affixing with epoxy	Photolithographic patterning and solder reflow	Photolithographic patterning and molding
Pattern Material	Stainless steel	Tin/Silver/Copper alloy	EpoTek 377 epoxy
Substrate Material	Aluminum	Copper	Glass

3.1.3. Leveling with F-TIR and Dip Depth Precision

As has been reported with any viscous drawing process like those listed in Chapter 2, parallelism between the upper pattern and the drawing media, either a thermoplastic film or an uncured resin, is essential for obtaining uniform structure arrays. The necessary degree of precision in alignment of the pattern to the polymer below increases with both increasing the area of the pattern and decreasing the size of the pattern features. Two scenarios in the current drawcasting system that can arise from imprecise leveling can result in a failed or undesirable structure. First, if the base of the ball bearing or BGA

pattern in a particular area touches the liquid ("over-dipping"), the liquid will wet the base, eliminating the possibility to draw structures from that vicinity. In the case of the rounded epoxy micropillar patterns, over-dipping is defined as a scenario in which the pattern extends into the polymer melt beyond the rounded caps of the micropillars. Conversely, if the pattern features in a particular area fail to make contact with the liquid ("under-dipping"), a structure cannot be drawn. Examples of over- and under-dipping for both a 3-mm diameter ball bearing and a 250-μm diameter rounded micropillar pattern are illustrated in Figure 3.12.

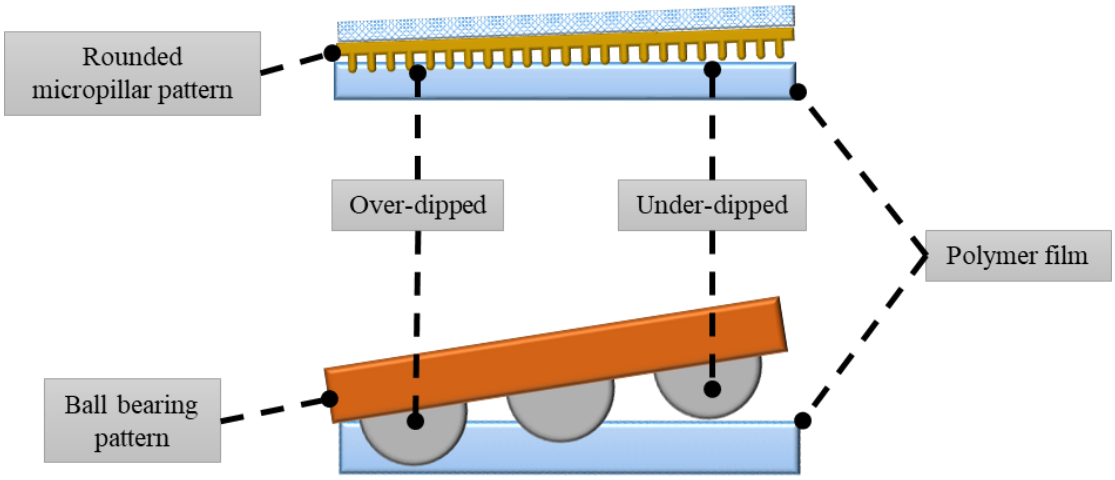

Figure 3.12. Drawing failures due to pattern misalignment with rounded micropillar (top) and ball bearing (bottom) patterns

As Figure 3.12 suggests, drawing failure due to under- or over-dipping occurs more readily in the smaller diameter micropillar patterns than in the larger BGA or ball bearing patterns. Any level of misalignment will lead to nonuniform structures across the drawn array, but a continuous array of structures can still be drawn using a larger-featured pattern with some degree of misalignment, whereas the same misalignment between a smaller-featured pattern results in drawing failure.

A fixture and procedure based on optical tactile sensors commonly used in fingerprint scanners were then developed to ensure parallelism between the upper pattern and the polymer films before drawing. In a basic fingerprint scanner, light is shone into a glass or acrylic substrate that acts as a waveguide or a “trap.” When viewed from one of the faces of the glass, the surface appears dark. However, when something contacts with one of the surfaces, the internal reflection is frustrated, and light escapes from the point of contact and scatters. The contact area appears as a bright spot when viewed from the opposite surface. The F-TIR mechanism is depicted in Figure 3.13 with an example of a fingerprint scanned using F-TIR [121].

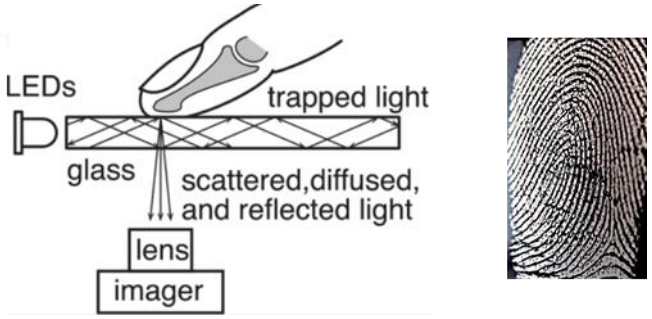

Figure 3.13. F-TIR mechanism and scanned fingerprint [121,122]

If the object contacting the glass is compressed onto the surface, the brightness of the scattered light will increase due to the increase in contact area. For this reason, F-TIR systems can also be used to visualize force distribution on a surface. This phenomenon is illustrated in Figure 3.14 [123].

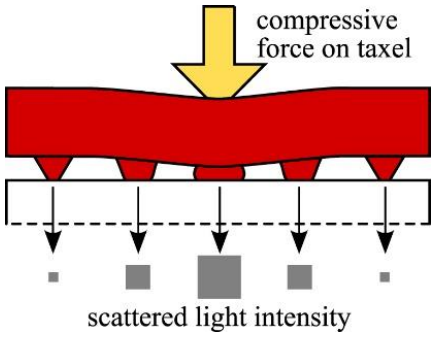

Figure 3.14. F-TIR response to changes in contact area [123]

An F-TIR system was built for the drawcasting system such that light entered the side of a glass substrate with an ITO coating functioning as the heated base. A 45° angled mirror was placed under the substrate, and a digital microscope (Dino-Lite) was directed at the mirror to image the underside of the glass. The edge of the glass where light entered was roughened by bead blasting so that the surface would act as a diffuser and ensure uniform distribution of the light within the glass [124]. The ITO-coated glass was then heated above the polymer's T_m, and the film was laid on the glass surface, ensuring conformal contact between the polymer film and the glass. The system was then cooled to room temperature by external heating fans, and the upper pattern was lowered to make contact with the polymer film. The upper pattern was connected to a stack of X- and Y-axis goniometers, which allowed adjustments to be made to the positioning of the upper pattern relative to the base. The F-TIR system is depicted schematically in Figure 3.15 (elements in image are not to scale).

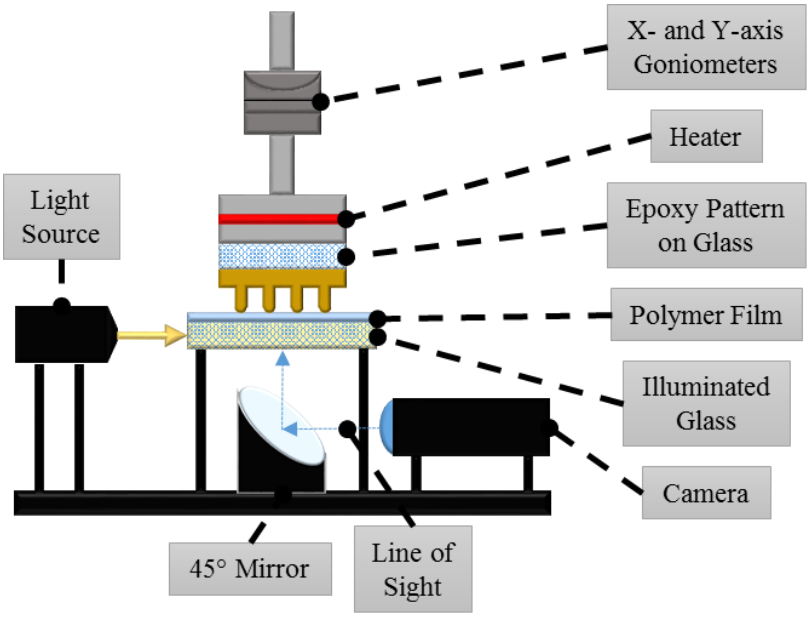

Figure 3.15. F-TIR setup for leveling pattern in drawcasting

The leveling procedure was then iterative: the pattern was lowered to make contact, and the area of the pattern in contact with the polymer film could be seen on the digital microscope. If one area shone brightly, indicating contact between the pattern and film, while the rest of the image was dark, the pattern would be raised and the goniometers would be adjusted to rectify the misalignment. This process was repeated as needed until the entire area of the upper pattern appeared to make contact with the polymer film at once, which was indicated by the entire image appearing bright. Images at different points in this leveling procedure are shown in Figure 3.16.

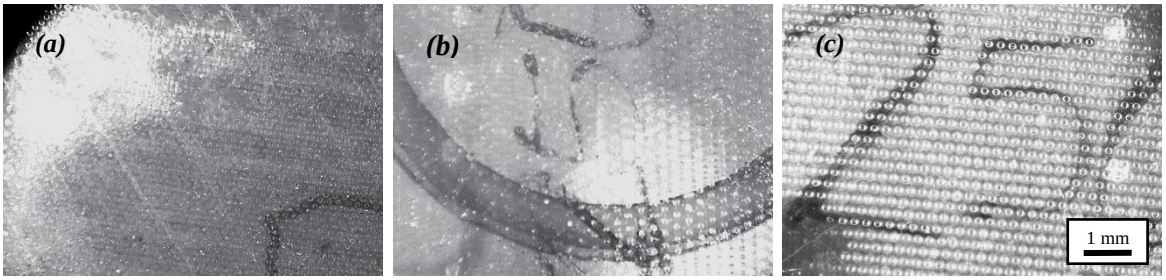

Figure 3.16. Misaligned (a and b) and aligned (c) drawcasting patterns imaged using F-TIR

The first two images depict a misaligned upper pattern, while the third image shows a pattern that is parallel to the polymer film.

As the diameter of the pattern feature is reduced, the height of the rounded portion of the pattern that can extend into the melt before over-dipping is drastically reduced as well. For example, the 3-mm diameter ball bearing patterns can extend 1.5 mm into a sufficiently thick molten film before the pattern is over-dipped, but the 100-μm diameter rounded micropillar pattern cannot exceed a dip depth of 30 μm before over-dipping. Thus, knowing the exact position of the pattern relative to the polymer melt becomes much more critical when drawcasting with smaller patterns. The position of the pattern when it makes contact with a solid film can be ascertained by using the F-TIR system and noting the displacement of the linear motor, but heating the film and the pattern after the leveling procedure in order to draw structures results in thermal expansion of the drawcasting fixture components. Accordingly, the displacement of the linear motor when the unheated pattern and solid film are in contact is not the same as the necessary displacement to make contact when the pattern and film are heated above the polymer's melting temperature. In the molten state, the F-TIR method cannot be used to visualize contact between the pattern and film, as the method relies on pressure being generated at an interface between two

materials in contact. When the film is molten and wets the heated pattern, is appears as essentially one material using the F-TIR system. For this reason, the optical microscope is raised after leveling with F-TIR to be parallel with the molten film, allowing one to monitor the gap between the pattern and film as well as the dip depth from a side view.

3.1.4. Pattern Release with Cellulose Solution

After drawing structures from the molten polymer films, the pattern and polymer are cooled to room temperature. In order to remove the pattern from the drawn structures without damaging the structure array, the patterns were coated with an ad hoc mold release. The mold release or coating on the patterns needed to be able to withstand high temperatures, sufficiently thin as to not disturb the surfaces of the drawn structures, and easily removable and water-soluble to avoid the use of solvents. For this purpose, an 0.5% solution by weight of hydroxyethyl cellulose, a common thickening or lubricating agent, was prepared in distilled water. Patterns were placed on a hot plate at 150 °C and sprayed with a solution using an air brush gun (paasche HAPK), which caused the water to evaporate immediately, leaving a thin layer of water-soluble cellulose on the pattern surface. After drawing, the patterns and attached structures were submerged in water and sonicated to dissolve the cellulose layer and allow detachment of the structures without damage.

3.2. Drawcasting Procedure and Parameters

The following sections detail the steps of the drawcasting process and the variables associated with each.

3.2.1. Step One: Lowering Pattern into Polymer Film

As previously stated, the pattern and polymer film are heated prior to lowering the pattern into the film. The temperature of the film and pattern must be chosen such that the polymer is able to wet and adhere to the pattern. The dip depth or extent of immersion of the pattern into the polymer film will dictate the degree of contact between the film and the pattern elements at the start of step two of drawcasting. The position of the pattern relative to the film's surface and the ensuing dip depth is monitored by an optical microscope which views the process from the side. Step one of the drawcasting process is illustrated in Figure 3.17.

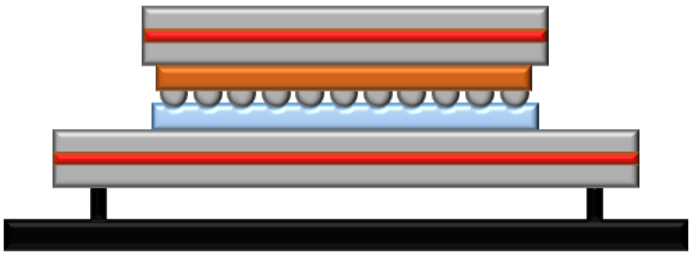

Figure 3.17. Drawcasting step one: pattern lowering and immersion

3.2.2. Step Two: Isothermal or Cooled Dwelling

Once the pattern is submerged into the polymer film to a desired depth, drawcasting can proceed in one of three ways. First, the pattern can be withdrawn immediately from the melt, meaning that the temperature at which the pattern is dipped and withdrawn are the same, and there is no dwell time. Second, the pattern can be allowed to dwell at a given depth in the polymer film isothermally, which gives the polymer time to wet the pattern, increasing the contact area between the two and encouraging adhesion of the polymer to the pattern. The contact area at the time of drawing and ensuing structural features such as the diameter of the cups and height of the overall structure would then be dependent on the wetting rate of the polymer with respect to the temperature and temporal length of the dwell. Finally, the pattern can be allowed to dwell in the molten film while the system is cooled. In this case, the heaters for the pattern and base are typically turned off, and external fans are turned on to expedite cooling. The dwell time is usually dictated by the desired temperature for drawing and cooling rate of the system. Dipping and drawing at different temperatures can be advantageous in that dipping at a higher temperature encourages wetting of the polymer melt on the pattern, and drawing at a slightly lower temperature enhances the strength of the melt by increasing its viscosity. A higher wetting rate encourages the polymer to adhere to the pattern, while a higher viscosity effectively strengthens the filament by slowing the rate of necking. Step two of drawcasting is illustrated in Figure 3.18.

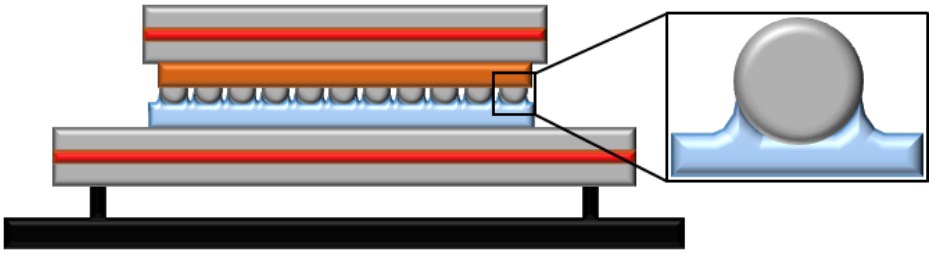

Figure 3.18. Drawcasting step two: isothermal or cooled dwelling

While there are certainly other methods that could be employed during this step of drawcasting such as stepwise lowering of the pattern or multi stages of isothermal dwells, the aforementioned three methods were the only ones considered in this body of work.

3.2.3. Step Three: Drawing

When the system reaches a prescribed temperature or has dwelled in the melt for the desired length of time, the pattern is drawn upward with a specified velocity to a desired height. These parameters, in conjunction with temperature, determine both the height of the overall structure as well as the shape of the structure's "stem," or the evolution of the structure diameter along the height. Step four of drawcasting is illustrated in Figure 3.19.

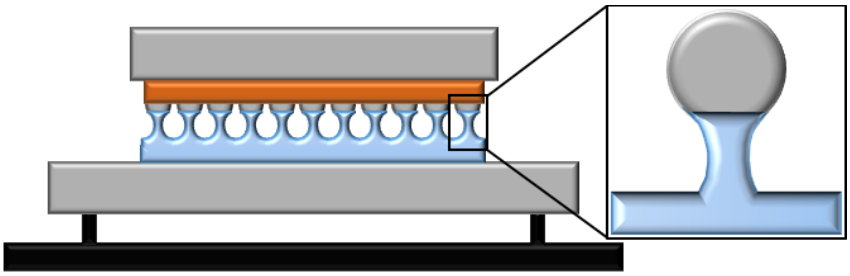

Figure 3.19. Drawcasting step three: drawing

As the response of thermoplastic polymers to deformation is dependent on both temperature and rate, the temperature and rate at which step four of drawcasting is performed are both critical in successfully drawing an array of structures. For example, if a structure is drawn at a given temperature at a sufficiently high velocity, the polymeric bridge may fracture due to an excessive plastic response of the polymer. Conversely, if the pattern is drawn at a very low velocity and a sufficiently high temperature, the polymer may have time to relax and neck completely before the structure reaches its desired height, an occurrence linked to the material's temperature-dependent relaxation time, capillary pressure on the polymeric bridge due to surface tension, and elastic recoil at both the base and the polymer/pattern interface. Cooling the system before and during drawing increases the viscosity of the melt, which serves to resist filament breakup before the polymer reaches its glass transition temperature [125]. These material properties will be discussed fully in later chapters.

3.2.4. Step Four: Cooling and Pattern Release

Once an array of structures is drawn to the desired height, the system is allowed to cool completely to room temperature. The pattern is then typically removed from the top heater, and the polymer film is removed from the base. The pattern and film, with the drawn structures attaching the two, are then submerged in water and sonicated in order to dissolve the cellulose solution and release the pattern from the structures, resulting in an array similar to that illustrated in Figure 3.20.

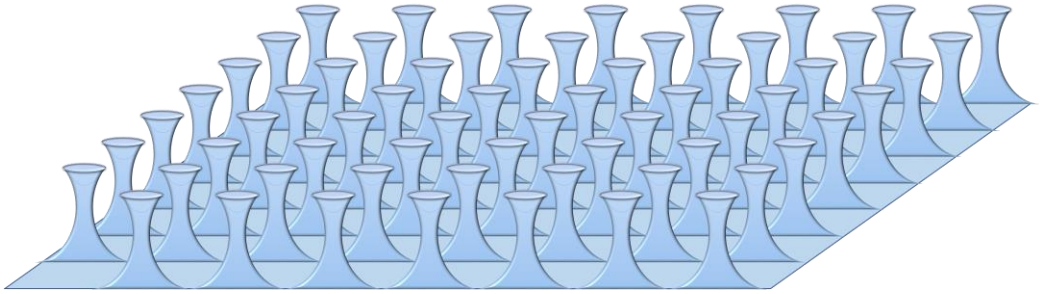

Figure 3.20. Drawn structure array after cooling and release

Finally, the preparation and four steps of drawcasting are summarized in Figure 3.21

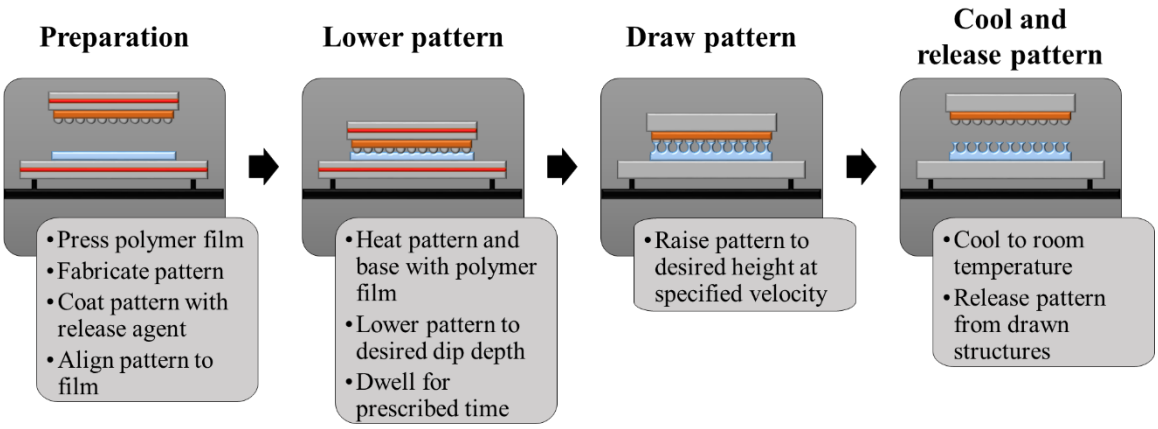

Figure 3.21. Drawcasting process summary

3.3. Drawcasting Testbed

The custom fixture built for the micro-suction cup drawcasting process is shown in Figure 3.22, while a current image of the drawcasting testbed is included in the Appendix.

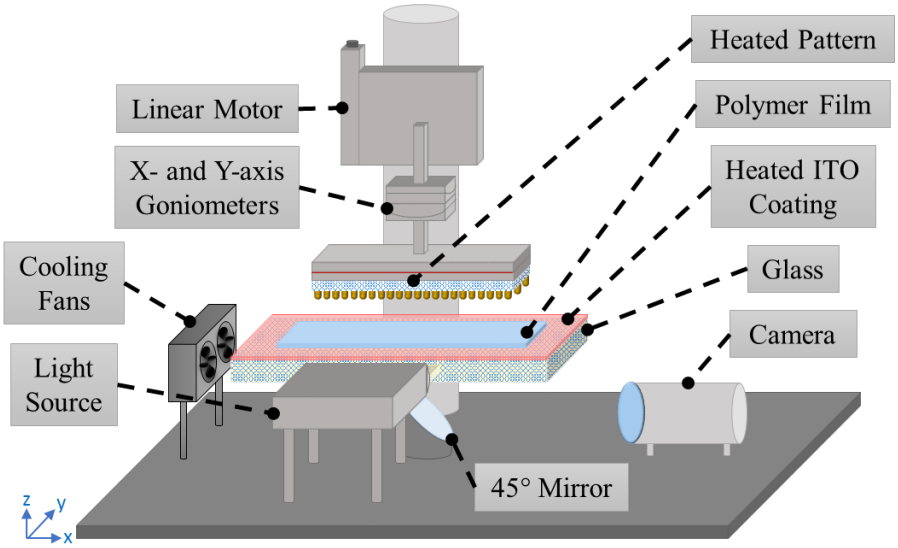

Figure 3.22. Drawcasting testbed

The heated pattern and goniometers are attached to a linear (z) motor (ThorLabs) with a velocity range of 1 µm/s to 20 mm/s. The linear motor, heaters, and digital microscope are all independently controlled by a computer, while the cooling fans, light source, and goniometers are controlled manually. After aligning the pattern to the polymer film using the F-TIR system, the glass substrate and the top pattern are heated to specified temperatures, to a maximum of 200 °C. The camera is then raised to the height of the heated base, and the drawcasting procedure is performed as described previously.

CHAPTER 4. EXPERIMENTAL PROCEDURES

To provide a versatile technique for fabricating desirable three-dimensional structures, operating limits for the process parameters must first be established with respect to the material being used. The background and measurement techniques of relevant rate- and temperature-dependent properties are discussed in the following sections, followed by a description of samples fabricated using drawcasting in order to elucidate the connections between the process parameters, material properties, and drawn structures.

4.1. Material Properties, Process Parameters, and Structural Features

Rate- and temperature-dependent material properties relevant to drawcasting, adjustable process parameters, and resulting structural features of interest are listed in Table 4.1.

Table 4.1. Drawcasting Variables

Structural Features	Process Parameters	Material Properties
Cup diameter	Heater temperatures	T_g, T_m, T_d
Cup radius of curvature	Immersion/dip depth	$\eta(T)$, cohesive strength as f(T)
Structure height	Draw temperature/dwell time	$\eta(\dot{\gamma})$, cohesive strength as f(V)
Minimum stem diameter	Draw speed	$\theta_c(t, T)$
Height of minimum stem diameter	Draw height	
	Pattern size and arrangement	

The structural features listed in Table 4.1 are shown schematically in Figure 4.1.

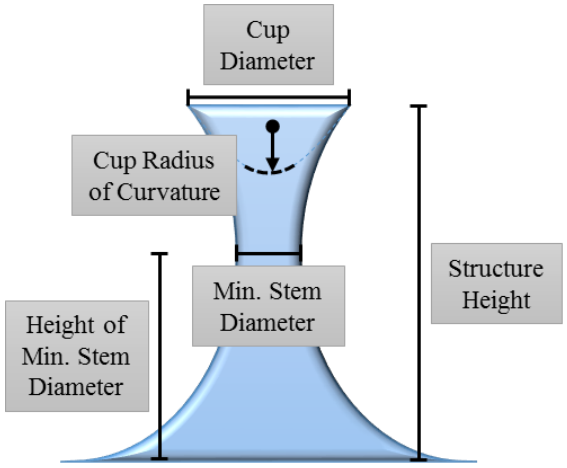

Figure 4.1. Suction cup structural features

While other material properties such as temperature-dependent surface tension are also linked to the relationships between process parameters and obtained structural features, only the material properties listed in Table 4.1 are investigated in this work. The structural features listed in Table 4.1 and shown in Figure 4.1 have been identified as the features that will most strongly affect the structure arrays' performance as a dry adhesive. Additionally, these structural features have been shown experimentally to be strongly affected by the drawcasting configuration and process parameters.

For a given thermoplastic, there are ranges of process parameters that can be used to draw structures. Outside of these ranges, either nothing can be drawn from the polymer film, or failure will occur in the structure at some point of the drawcasting process. For example, if the initial heater temperatures are too low, the polymer film will not wet the pattern, and no structures will be drawn upon raising of the pattern. Similarly, if the system

is allowed to cool too much before drawing, the viscosity of the film will be too high to allow sufficient deformation of the film to draw structures.

The temperature-dependent phase behavior, temperature- and rate-dependent rheological properties, and the temperature- and time-dependent wetting behavior of the thermoplastic being used in drawcasting will dictate the overall ability to successfully draw a structure. As such, these properties also have direct effects on all the structural features of the micro-suction cups of interest.

4.2. Materials

Three polymers commonly used in high-throughput manufacturing of nonwoven materials and personal consumer products were used in fabrication with the micro-suction cup drawcasting system: Dow INFUSE 9108 and 9508 elastomers and ExxonMobil LGA 105 low-density polyethylene (LDPE). Selected thermal and molecular properties of these polymers are given in Table 4.2 [126-129].

Table 4.2. Polymer Properties

Polymer	Density (g/cm^3)	MFI (g/10 min, 2.16 kg at 190 °C)	Ultimate Tensile Strength (MPa)	M_n (kDa)	M_w (kDa)	PDI
9108	0.866	1	5.1	63	156	2.48
9508	0.866	5	2.9	38	101	2.66
LDPE	0.920	6.5	9.9	N/A		

The 9108 and 9508 elastomers are multi-block copolymers comprised of semicrystalline ethylene-octene blocks (“hard” blocks) with low octene concentration alternating with amorphous ethylene-octene blocks (“soft” blocks) with high octene concentration. The

block copolymers are synthesized using two catalysts, one forming the high density, PE-majority block, and the other forming the ethylene chain with a high incorporation of octene. The size and distribution of the blocks, and ensuing mechanical properties, are controlled by the concentration of catalysts and chain shuttling agent used during synthesis [130,131]. The mechanical properties such as high tensile elongation and the processability of these elastomeric block copolymers make them attractive for both the drawcasting process and the application of micro-suction cups as arrayed dry adhesives.

LDPE was also used in this study in order to investigate the applicability of the drawcasting process to more rigid thermoplastics. Furthermore, LDPE melts are known to have strain hardening properties in extension due to its high degree of long-chain branching [132]. The effect of strain hardening on the extension of polymer melts will be discussed later in this chapter.

4.3. Thermal Characterization

4.3.1. Background

4.3.1.1. Thermal Transitions

The thermal properties of polymers are characterized by measuring a sample's weight and/or the energy it gains or loses as a function of time or temperature. The measurement of mass loss with respect to temperature or time is known as thermogravimetric analysis (TGA), while the measurement of endo- or exothermic events with time or temperature is known as differential scanning calorimetry (DSC) or differential thermal analysis (DTA). TGA instruments consist primarily of a precision

balance and a programmable furnace, and measurements can be taken as a function of temperature or as a function of time at a constant temperature. The mass loss measured by TGA is used to determine the onset of events such as volatilization or decomposition. DSC or DTA measurements require two sample holders, and the difference in energy input to the sample of interest with respect to that of a reference material is measured as both are subjected to a controlled temperature program. An empty pan is usually used as the reference material, while the sample is placed in a second, identical pan. The empty pan generally heats up faster than the sample due to the sample's heat capacity, but the rate of change of the temperature of the sample and reference with respect to the applied temperature is the same until a thermal event occurs in the sample. These events include phase changes such as melting, crystallization, or decomposition, or a glass transition. During melting, for example, the temperature of the sample does not change with increasing input temperature, as melting is an endothermic reaction, meaning it requires excess energy (in the form of heat) to proceed. This change in heating of the sample with respect to the reference appears on a DSC curve of heat flux (measured by the instrument in volts and converted to watts through appropriate instrument calibrations) versus temperature as a peak in the plot. The glass transition of a polymer appears on a DSC curve as a change in the baseline of the plot of heat flow with increasing temperature. After the glass transition, the amorphous portions of a semicrystalline polymer gain mobility, and the heat capacity of the sample increases, meaning the sample requires more heat energy to effect a change in its temperature after the glass transition. This results in an upward shift in the previously linear plot of heat flow versus temperature [133,134].

DTA and TGA measurements can be taken simultaneously by some instruments, known as simultaneous thermal analyzers (STA). When measuring the thermal properties of a polymer sample, a preheating cycle is necessary, as the heating and cooling conditions the sample previously experienced determine its crystalline state and, thus, its glass transition and melting characteristics. If a semi-crystalline polymer is allowed to cool slowly, the molecular chains have a greater chance of diffusing into an ordered region and crystallizing, while a polymer cooled quickly or quenched will have a greater portion of amorphous material since the molecular chains are not afforded the time necessary to crystallize [134].

4.3.1.2. Crystalline Content

The crystalline content of a polymer sample can also be calculated from an STA measurement by determining the heat of fusion (ΔH_m) and the heat of cold crystallization (ΔH_c) and comparing their difference to the heat of fusion of a purely crystalline form of the polymer ($\Delta H_m°$), according to Equation 4.1 [134].

$$\% \, crystallinity = \frac{\Delta H_m - \Delta H_c}{\Delta H_m{}^0} \cdot 100 \qquad (4.1)$$

4.3.2. Experimentation

STA measurements were performed according to ASTM D3418 [135]. Samples of each material weighing between 10 and 20 μg were prepared and placed in Al_2O_3 crucibles fitted with lids with a small hole, allowing the escape of volatile species during heating.

Each sample was first heated from room temperature to 200 °C at a rate of 10 °C/min. under a 50 mL/min. flow of air. Each sample was cooled back to room temperature at the same rate to erase its thermal history. The sample of interest was then heated to 500 °C under the same conditions, and the heat flow versus temperature behavior of each sample was recorded. The glass transition temperature of each sample was identified as the midpoint of the change in the baseline of each STA curve, while the melting and degradation temperatures were identified as the temperature at the onset of melting or degradation events.

The change in enthalpies of melting and cold crystallization were determined for each sample by integrating the melting and crystallization peaks of the obtained STA curves in MATLAB. The crystalline percentages of each sample were calculated according to Equation 4.1, taking the latent heat of melting of a purely crystalline PE sample as ΔH_m^0=293.6 J/g [136]. The exact structure of the commercial thermoplastic elastomers is undisclosed, but the manufacturer's website indicates that the majority of the block copolymers are comprised of ethylene units [128]. As such, the value of the latent heat of melting for purely crystalline PE was also used in the crystallinity calculations of these materials in order to obtain a relative value.

4.4. Wetting

4.4.1. Background

The wettability of a surface is governed by its chemical and physical characteristics as well as material properties of the polymer. A surface is characterized as either having

an affinity for or an aversion to an impending liquid by the contact angle a drop of the liquid makes with the surface. In general, a liquid will wet a surface if the adhesive forces between the liquid and the solid are greater than the cohesive forces within the liquid. The surface energy and roughness of the substrate and the surface tension and viscosity of the liquid all influence the liquid/solid adhesive and liquid cohesive force balance. Equilibrium contact angles are typically measured by dispensing a drop of liquid on the surface of interest and observing the angle formed by the intersection of the liquid-solid and liquid-vapor interface. This angle initially changes with time, as the contact area increases immediately after the liquid is dispensed. The rate of increase of the contact area defines the wetting rate of the system, and the equilibrium contact angle is defined as the angle at the liquid-solid-gas three-phase contact line when the rate of change in the contact area is negligible or nonexistent [137-139]. The wetting rate of any liquid on a surface is related directly to its surface tension and inversely with its viscosity, as shown in Equation 4.2,

$$A(t) \propto l_0 \left(\frac{\gamma t}{\eta}\right) \tag{4.2}$$

in which A refers to the wetted area after time t, l_0 is the initial linear dimension of the drop, and γ and η are the melt's surface tension and viscosity, respectively, both of which vary strongly with temperature [140].

4.4.2. Experimentation

In the drawcasting process, the initial contact area and contact angle between the pattern and the polymer melt is established by the immersion or dip depth of the pattern into the molten film. If the pattern is allowed to dwell in the melt before drawing, the contact area will increase at a rate dependent on both the temperature of the system as well as how far the initial contact angle is from its equilibrium angle at that temperature. This change in contact area occurs between steps one and two of drawcasting and is illustrated in Figure 4.2.

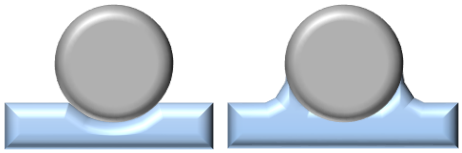

Figure 4.2. Initial contact between pattern and polymer melt (left) and pattern wetting after dwelling (right)

The contact area at the onset of drawing directly affects the overall success of the process as well as the geometry of the structures obtained. An understanding of the polymer's temperature-dependent wetting behavior is crucial in order to understand the effect of the temperatures and dwell time implemented during drawcasting on the obtained structures.

Wetting measurements were carried out on each polymer sample at temperatures ranging from 130 to 190 °C in intervals of 20 °C. In each measurement, a 650-μm thick polymer film was placed on the heated base of the drawcasting testbed. A single 3-mm diameter ball bearing was attached to the upper heater at the same temperature as the base on the linear motor of the testbed and was coated in hydroxyethyl cellulose solution. The

upper heater with the ball bearing was lowered until it contacted the molten film, and the evolution of the contact area was recorded using a digital microscope (FLIR Blackfly, 170fps) for a duration of 10 minutes. The change in the diameter of the wetted area with time was measured using ImageJ software with the DropSnake plugin [141]. The modified testbed for contact angle measurements is depicted in Figure 4.3.

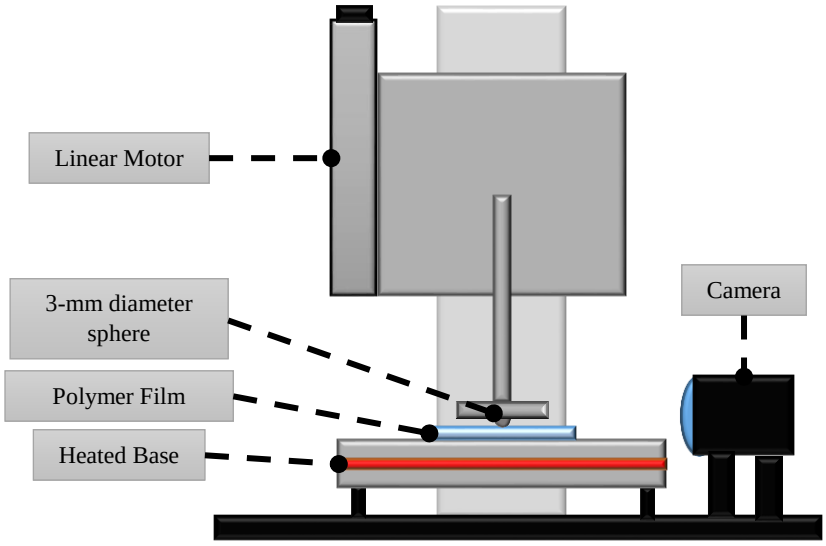

Figure 4.3. Contact angle measurement fixture

4.5. Rheological Studies

4.5.1. Background

The ability to draw a structure from a molten film depends on both the adherence of the melt to the pattern and the melt's viscoelastic response to the force imposed by the upward motion of the pattern. In order to deform a formerly flat semi-infinite reservoir of material (i.e., a sufficiently thick film), the adhesion between the material and the adherend needs to be stronger than the cohesive forces holding the material together and resisting it

from being deformed or stretched. Adhesion of the melt to the pattern surface depends on the wetted area, which, as detailed in section 4.3, is related to both the temperature and the contact time. As stated, the temperature dependence of the wetting rate arises from the polymer's temperature-dependent viscosity. The cohesion of the melt is characterized by the dependence of its viscoelastic properties on both temperature and deformation rate. As discussed in Chapter 3, there exists a range of process conditions for a given material that will yield a successful structure array in drawcasting. The viscoelastic response of the three polymers of interest, 9108 and 9508 elastomers and LDPE, at conditions similar to those used in drawcasting will be explored in the following sections. The polymer's viscoelastic properties as they relate to the cohesion of the polymer melt during drawcasting are first discussed, and their measurement through oscillatory shear testing is detailed. The adhesion of the polymer melt and upper pattern is then analyzed through probe-tack testing, in which a hemispherical probe is brought into contact with a molten polymer film and subsequently withdrawn at a constant velocity.

An understanding of the polymer melt's viscoelastic properties in shear and extension is crucial to establish limits on the process conditions employed in drawcasting and to predict whether an array could successfully be drawn for a given parameter set. Furthermore, characterization of the material's shear and extensional behavior is necessary for any future analytical or numerical modeling of the drawcasting process.

4.5.2. Shear Rheology

4.5.2.1. Shear Rheological Principles and Oscillatory Testing

The most widely studied rheological property of polymers is the shear viscosity, which describes the relationship between the shear stress in a material and a particular applied strain rate. For an incompressible fluid such as a polymer melt, the total shear stress tensor is defined in Equation 4.3,

$$\bar{\bar{\pi}} = -p\bar{\bar{\delta}} + \bar{\bar{\tau}} = \begin{pmatrix} p + \tau_{xx} & \tau_{yx} & 0 \\ \tau_{yx} & p + \tau_{yy} & 0 \\ 0 & 0 & p + \tau_{zz} \end{pmatrix} \tag{4.3}$$

in which p represents the pressure, $\bar{\bar{\delta}}$ is the identity matrix, and $\bar{\bar{\tau}}$ is the shear stress tensor that arises from the viscosity of the fluid. The pressure and normal stress contributions (the diagonal terms of the matrix in Equation 4.3) are difficult to separate in typical shear measurements, so the rheological behavior of polymer melts is usually described by the three following quantities:

- shear stress: τ_{xy},
- first normal stress difference: $N_1 = \tau_{xx} - \tau_{yy}$,
- and second normal stress difference: $N_2 = \tau_{yy} - \tau_{zz}$.

In simple, steady shear flows, the stresses are functions only of the applied shear rate, $\dot{\gamma}$. Steady shear flow in polymer melts is then described by Equations 4.4-6.

$$\tau_{yx} = -\eta(\dot{\gamma})\dot{\gamma}_{yx} \tag{4.4}$$

$$\tau_{xx} - \tau_{yy} = -\Psi_1(\dot{\gamma})\dot{\gamma}_{yx}{}^2 \quad (4.5)$$

$$\tau_{yy} - \tau_{zz} = -\Psi_2(\dot{\gamma})\dot{\gamma}_{yx}{}^2 \quad (4.6)$$

These equations are referred to as the material's viscometric functions, and Ψ_1 and Ψ_2 are knows as the first and second normal stress coefficients, respectively [142-144].

The viscosity of polymer melts is directly proportional to the shear rate at low rates. The viscosity approaches a constant value with decreasing shear rate, which is defined as the zero-shear viscosity and denoted as η_0. With increasing shear rate, the viscosity of most polymeric materials decreases, and the melt is defined as shear-thinning. The shear-thinning region of a $\eta(\dot{\gamma})$ plot often obeys a power law given in Equation 4.7,

$$\eta(\dot{\gamma}) = k\dot{\gamma}^{n-1} \quad (4.7)$$

in which *k* is a material-dependent parameter and *n* is the power law exponent. The region in which the stress is proportional to strain known as the linear viscoelastic envelope (LVE), and many shear rheological studies are performed in this region [142,145].

The application of a steady shear flow at a range of rates to a polymer melt in a linear fashion is difficult to achieve experimentally. As such, the rheological behavior of a polymer melt in shear is often studied using an oscillating rheometer with a parallel plate or cone and plate configuration. In a typical small amplitude oscillatory shear (SAOS) measurement, a sinusoidally varying strain γ with an angular frequency ω at a strain rate within the LVE is applied to a polymer sample between two plates according to Equation 4.8.

$$\gamma(t) = \gamma_0 sin(\omega t) \tag{4.8}$$

The resulting time-varying shear stress of the viscoelastic material exhibits components both in-phase and out-of-phase with the applied strain. The shear stress and strain will oscillate at the same frequency, but the stress response will lead the strain by a phase angle δ according to Equation 4.9.

$$\sigma(t) = \sigma_0 sin(\omega t + \delta) \tag{4.9}$$

The shear stress can be separated into its orthogonal functions, which relate the phase angle to the ratios of the amplitudes of stress and strain, described in Equations 4.10-12.

$$\sigma(t) = \gamma_0 [G'(\omega)\, sin(\omega t) + G''(\omega)\, cos(\omega t)] \tag{4.10}$$

$$G' = \frac{\sigma_0}{\gamma_0} cos\delta \tag{4.11}$$

$$G'' = \frac{\sigma_0}{\gamma_0} sin\delta \tag{4.12}$$

G’ and G’’ are termed the storage and loss moduli, and they represent the respective in-phase elastic component and out-of-phase viscous component of the shear stress response. The ratio of the loss and storage moduli is known as the loss tangent, defined in Equation 4.13.

$$tan\,\delta = \frac{G''}{G'} \tag{4.13}$$

The loss tangent illustrates the degree to which a polymer melt is behaving as a solid or as a liquid at the prescribed conditions. A low loss tangent value implies that the response of the material is dominated by elastic storage, while a high loss tangent indicates that the energy of deformation is dissipated throughout the material in the form of heat and cannot be recovered by releasing the external load. Within the linear viscoelastic range, rheological parameters such as the loss and storage moduli and the loss tangent are independent of the value of stress amplitude applied during testing [142,143,146,147].

At high frequencies of applied strain, thermoplastics exhibit a low loss tangent and elastic, glassy behavior, while the low frequency or long-time response is always more viscous with a high loss tangent. The differing behavior of polymer melts at high and low frequencies of shear deformation is due to a difference in the ability of the polymer structure to relax or return to equilibrium after the imposed deformation. If a strain is imposed on a polymer melt and released, the stress in the melt cannot dissipate instantaneously, but rather decreases over a time scale, which is termed the relaxation time. The relaxation time of a melt at a given temperature can be determined by plotting the storage and loss moduli as a function of the angular frequency and noting the frequency at which the moduli traces cross one another. This is the frequency below which, viscous behavior dominates and above which, elastic behavior dominates. The relaxation time of the melt is defined as the inverse of this crossover frequency. A number of factors can influence the relaxation time and overall viscoelastic response of a polymer melt. These include molecular structure such as branching, temperature, and the average molecular weight and its distribution [144].

Viscoelastic flows are often characterized by two dimensionless numbers: the Deborah number (De) and the Weissenberg number (Wi). The Deborah number is a ratio of the relaxation time (λ) and the timescale over which the flow is observed (t_{obs}), defined in Equation 4.14.

$$De = \frac{\lambda}{t_{obs}} \tag{4.14}$$

A high Deborah number, with a long relaxation time and/or short observation time, the material exhibits a solid-like response. Conversely, a flow with a short relaxation time and long observation time will exhibit fluid-like behavior. The Weissenberg number is a ratio of the elastic and viscous forces in a system, defined by the material's relaxation time and a ratio of a characteristic velocity (U) and length scale (L), as shown in Equations 4.15 and 4.16 [142].

$$Wi = \lambda \frac{U}{L} \tag{4.15}$$

$$Wi = \frac{elastic\ forces}{viscous\ forces} = \frac{\tau_{xx} - \tau_{yy}}{\tau_{xy}} = \frac{\lambda \eta \dot{\gamma}^2}{\eta \dot{\gamma}} = \lambda \dot{\gamma} \tag{4.16}$$

In simple, steady shear, the predominant elastic force is due to the first normal stress difference ($\tau_{xx} - \tau_{yy}$ or N_1), while the viscous forces are simply due to the shear stress τ_{xy}. The first normal stress difference and the shear stress can be expressed as a function of the relaxation time, viscosity, and shear rate, as shown in Equation 4.16, through application of the upper-convected Maxwell differential model, which simplifies the

Weissenberg number to a product of the relaxation time and a characteristic deformation rate $\dot{\gamma}$ [148].

4.5.2.2. Time-Temperature Superposition

Viscoelastic data obtained from oscillatory shear measurements on polymer melts at different temperatures can often be combined on a single master plot. Shift factors are used to extrapolate the data to temperature or shear frequencies not experimentally determined using the time-temperature superposition principle (TTS). This principle is based on the idea that increasing the temperature of a polymer melt has an equivalent effect on its viscoelastic behavior as does changing the shear rate. For example, changing the temperature of a polymer melt does not change its functional dependence of η on $\dot{\gamma}$; it merely changes its zero-shear viscosity and the shear rate range that makes up the LVE. The viscosity at a certain temperature and shear rate is then equal to the viscosity at a reference temperature T_0 after correcting for the dependence of η_0 on temperature by using a horizontal shift factor $a_T(T)$, as given in Equation 4.17.

$$\eta_0(T) = a_T \eta_0(T_0) \tag{4.17}$$

TTS can be used with a variety of data sets, such as stress relaxation, creep compliance, and storage and loss moduli. Many of these viscoelastic functions can also be related to one another, greatly reducing the amount of experimental work needed to fully characterize a polymer's shear rheological profile [142-143].

The amount of horizontal shifting required to align data to a master curve, or the value of a_T, can typically be described by either applying the Williams-Landel-Ferry (WLF) model or the Arrhenius model, which are given in Equations 4.18-4.19, respectively.

$$WLF\text{: } \log a_T = \frac{-c_1(T-T_0)}{c_2+T-T_0} \tag{4.18}$$

$$Arrhenius\text{: } \log a_T = \frac{E}{R(T-T_0)} \tag{4.19}$$

In the WLF equation, c_1 and c_2 are material- and temperature-dependent constants. In the Arrhenius equations, E refers to the material's activation energy, while R is the universal gas constant. The WLF equation is typically used to describe the behavior of polymers at temperatures within 100 °C of their glass transition temperature, as the equation is based on the assumption that the fractional free volume of the polymer increases linearly with temperature in this range. The Arrhenius equation is typically used at temperatures exceeding T_g+100 °C, as the temperature of is regarded to be the rate-limiting factor in this region, rather than the material's free volume [149,150].

4.5.2.3. Rheological Models

Frequency-dependent linear viscoelastic data can also be used to predict steady state shear viscosity as a function of shear rate, as the steady state shear viscosity and the dynamic viscosity (obtained as a function of frequency) are equivalent at corresponding values of frequency and shear rate, shown in Equation 4.20.

$$\eta(\dot{\gamma}) = |\eta^*(\omega)|\big|_{\omega=\dot{\gamma}} \tag{4.20}$$

In Equation 4.17, η*(ω) denotes the frequency-dependent complex viscosity obtained from oscillatory measurements. This relationship is known as the Cox-Merz rule and is often used to convert oscillatory data to steady shear data in order to determine a polymer's zero-shear viscosity. A rheological model is typically fit to $\eta(\dot{\gamma})$ plots in order to extrapolate the data to zero shear and infinite shear, where the viscosity often plateaus again to an infinite-shear viscosity η_∞. There are a variety of established rheological models available for this purpose, one of the most popular being the Carreau-Yasuda model given in Equation 4.21.

$$\frac{\eta-\eta_\infty}{\eta_0-\eta_\infty} = [1 + (\lambda\dot{\gamma})^a]^{\frac{n-1}{a}} \tag{4.21}$$

In this model, λ denotes the polymer's relaxation time, *n* is the power law exponent, and *a* is a dimensionless parameter that describes the transition between the zero-shear plateau and the power law region of the plot of viscosity with respect to shear rate [142].

4.5.3. Tack

4.5.3.1. Principles of Tack

Tack is an extrinsic material property most commonly measured for pressure sensitive adhesives (PSAs). The tack of a material describes its ability to form a bond to another material under light pressure in a short time. In a typical probe-tack experiment, a

probe, either flat or spherical, is brought in contact with a polymer at either a specified pressure or penetration depth. The probe is kept in contact with the polymer for a certain period, after which it is raised at a given velocity. The force supplied to retract the probe is measured as a function of time or distance, and the tack of the material is defined as the maximum stress attained during testing. In the testing of PSAs, the interface between the polymer and the probe is usually of the highest interest, as the purpose of the measurement is generally to determine the stress the PSA can withstand before delaminating from the probe [151-153]. The force-distance curve can also be used to calculate the energy of adhesion or cohesion, taken as the area under the curve. In a typical probe-tack test in which the polymer delaminates from the probe, the force increases steadily and abruptly falls to zero when delamination takes place. If the polymer remains adhered to the probe, the force increases sharply with initial separation until it reaches a maximum, after which it slowly decays to zero due to the thinning of the polymeric bridge between the probe and the base. The maximum force (or stress, if normalized by contact area) corresponds to the onset of necking of the material, while the decaying force is related to the rate of thinning or necking of the polymeric bridge [151,154,155].

4.5.3.2. Filament Failure

At low extension rates or velocities, polymeric filaments can fail in the LVE region [155]. Failure occurs at low rates due to capillary thinning, also referred to as necking instability. Polymeric filaments at high extensional strains with, consequently, very small mid-filament radii are strongly affected by surface tension [154]. The slender filament slowly

thins either with increasing strain or after the cessation of stretching after reaching a high strain due to capillary pressure, which is shown in Equation 4.22 to be proportional to surface tension and inversely proportional to the mid-filament radius [157].

$$p_c \propto \frac{\sigma}{R(z)} \tag{4.22}$$

The mid-filament radius of a polymer melt after stretching decreases in an exponential manner. Additionally, the rate of thinning of the filament is proportional to the melt's surface tension but inversely proportional to the melt's viscosity and the initial radius at the cessation of stretching. As such, filament thinning and break-up can be opposed by increasing the filament's viscosity and lowering its surface tension, which can be achieved in a practical manner by cooling the melt, as is done during drawcasting [156,158-160].

At intermediate extensional strain rates, the LVE region is usually followed by an increase in the elongational viscosity with increasing strain, a phenomenon known as strain hardening. The strain hardening effect becomes more pronounced at higher rates of deformation, as it reflects entanglements in the melt that lock up in extension and effectively strengthen the melt. This deformation-induced strengthening is not seen in shear, and yielding and chain sliding is thought to take place more readily in shear than in extension. As such, comparable rates of deformation in shear and extension could lead to failure in extension but not in shear [161,162].

In the region of intermediate extensional strain rates, the elastic response of the material increases, giving rise to a competition between viscous and elastic deformations. At these intermediate strain rates, the viscoelastic response of the polymer begins to

overcome the effects of surface tension, which reduces the effect of the capillary pressure. The rate of necking at intermediate rates is often less severe than that at very low extensional rates. Failure at intermediate rates usually occurs due to necking instabilities when the mid-filament radius is sufficiently small, often at higher strains that those achievable at very low deformation rates [154,156,158]. If the temperature of the system is lowered during or after extension, the viscosity of the melt increases and its surface tension decrease, which can decline the rate of capillary thinning and preserve the liquid bridge, if desired [109,159,163-165].

At very high extension rates, the elastic response of the polymer is dominant, as deformations are imposed faster than the polymer is able to relax. Failure at high extension rates is typically similar to a glassy or brittle fracture [142,154,158]. With increasing extension rates, failure can occur at the adhesive-probe interface with no extension of the polymer or transfer of material from the base to the probe. This type of failure typically occurs at higher extension rates than those for which brittle fracture is observed [151].

The rate dependence of polymeric filament failure is illustrated in Figure 4.4, in which the critical strain or strain-to-failure ε^* is plotted as a function of a constant strain rate $\dot{\varepsilon}$.

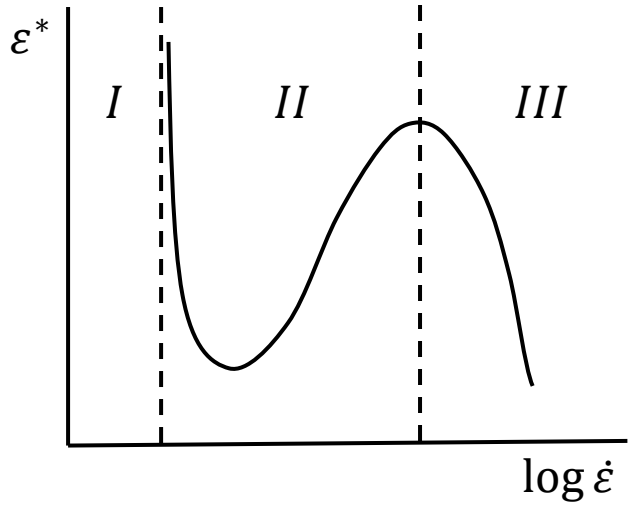

Figure 4.4. Polymer melt critical strain as a function of extension rate

At very low strain rates, region I of Figure 4.4, the polymer behaves almost purely as a fluid, exhibiting a primarily viscous response. In this case, the critical strain is theoretically infinite, neglecting any volume or gravitational restrictions. In region II, the critical strain initially drops from its infinite, asymptotic nature as the increasing strain rate elicits an elastic response from the melt. The magnitude of this elastic response relative to the viscous response increases with increasing strain rate. The critical strain increases accordingly, as a higher degree of elasticity lowers the rate of necking and provides resistance to rupture. At exceedingly high extension rates, region III, the response of the polymer is primarily elastic, inhibiting the polymer's ability to viscously deform, leading to rapid brittle fracture [154,158,166].

4.5.3.3. Tack and Shear Rheology Correlation

A combination of shear rheological experiments and probe-tack tests are usually presented when characterizing PSAs, and the same principles motivate the choice of these

experiments in characterizing the drawcasting process. As previously stated, the ability to draw a structure from a molten film depends on the adherence or bonding of the melt to the pattern as well as the resistance of the melt to deformation. The initial bonding process in which the melt spreads on the pattern or probe is a low-rate process in which the polymer exhibits a viscous or liquid-like response. The elastic and storage moduli (or simply tan δ) in the low frequency range of a shear rheological measurement can be correlated to the tack of the polymer. If the elastic modulus at low frequencies is high, the ability of a melt to wet the probe is reduced. The tack of a polymer is enhanced under conditions in which tan δ is greater than unity, meaning the material has a predominantly viscous response, as a larger contact area between the polymer and probe can form more easily. Conversely, the delamination of the polymer from the probe or pattern that can occur at high rates or low temperatures is due to a predominantly elastic response of the polymer, which is characterized at high frequencies in shear oscillatory testing when the storage modulus is greater than the loss modulus (tan $\delta<1$) [153,167].

4.5.4. Experimentation

4.5.4.1. Shear Measurements

An oscillatory rheometer (Discovery HR-2, TA Instruments) with an environmental test chamber in a parallel plate configuration with 25-mm plates was used for all shear rheological measurements in this work. The LDPE, 9508, and 9108 polymers were pressed to 650-μm thick films and cut to 25-mm diameter discs for each shear measurement. For each material, a strain amplitude sweep was conducted at both 130 and 200 °C in order to

identify a strain amplitude in the material's linear viscoelastic range for both temperatures. In each experiment, the upper plate oscillated at 10 rad/s while the strain amplitude was swept logarithmically from 0.025 to 25%. It was found that all three materials behaved linearly at both temperatures at a strain of 5%.

Frequency sweeps were then performed on each material at temperatures ranging from 130 to 200 °C. In each measurement, the angular frequency of the upper plate was logarithmically swept at a fixed strain amplitude of 5% from 0.1 to 100 rad/s. In some of the experiments, the G' G'' crossover did not occur in the 0.1-100 rad/s frequency range, and the test range in was extended to 500 rad/s in those measurements. Plots of the storage and loss moduli with angular frequency were obtained, and the relaxation time was calculated for each condition from the crossover frequency of the two moduli. The oscillatory data was then transformed to steady state data using the Cox-Merz relation, yielding plots of viscosity versus shear rate for each experimental condition. Curves were then fitted to the η vs $\dot{\gamma}$ plots using the Carreau-Yasuda model in order to obtain the zero-shear viscosity of the material at the temperatures of interest. Finally, the oscillatory data for each material was compiled to a master curve at a reference temperature of 160 °C using the time-temperature superposition principle. The horizontal shift factors were fitted with the Arrhenius model. The rheological model fits and TTS were performed using Trios software (TA Instruments).

4.5.4.2. Tack Measurements

The same parallel plate rheometer used for shear rheological measurements was used in axial tension mode to measure both the tack/adhesion of the polymer melts to the probe as well as the extension behavior or cohesion force exerted by the polymer during drawing. An 8-mm diameter lower plate was used, while the upper plate was replaced with a spherical indenter mimicking the upper patterns used in drawcasting. The spherical indenter was fabricated by fitting an 8-mm diameter stainless steel spherical variance indicator (McMaster-Carr) to an upper parallel plate. Films of the three polymers used in this study were again pressed to 650 μm in thickness and were cut into 8-mm diameter discs. Extensional tests were conducted on each material at a variety of temperatures by monitoring the normal force as the head of the rheometer raised upward at a controlled rate. In each experiment, the oven and test fixture were first allowed to equilibrate at the desired temperature. The environmental test chamber of the rheometer was a "clamshell" type oven that enclosed the fixture during testing at elevated temperatures, so the oven doors were kept closed at all times other than sample loading/unloading. After reaching the desired temperature, the gap between the indenter and the bottom plate was zeroed. The head was raised, and the polymer film of interest was placed on the lower plate. The doors of the environmental test chamber were then closed, and the system was again allowed to equilibrate. The head was then lowered to a gap of 350 μm, meaning the indenter was pressed 300 μm into the melt. The film thickness and gap were kept constant throughout all extensional experiments to ensure that a constant initial contact area was maintained. For the 8-mm diameter spherical indenter, an extension of 300 μm into the molten polymer

film corresponded to a contact area between the polymer and the indenter of approximately 7.5 mm^2. After the head was lowered, the spherical indenter was allowed to dwell in the melt for 10 seconds, after which it was raised 10 mm at a prescribed velocity. The effects of changing the contact time or total strain on the extensional properties of the polymers were not included in this study. Experiments were performed on each material at temperatures ranging from 120 to 200 °C at intervals of 10 °C. In each experiment, a sample was drawn at its prescribed temperature at constant velocities of 50, 100, 500, 1000, 5000, and 10,000 μm/s. Figure 4.5 depicts a polymer sample after an extensional experiment.

Figure 4.5. Polymer melt extensional experiment

Each experiment was performed twice, and the obtained data was averaged. In these experiments, it was found that coating the surface of the stainless-steel spherical indenter with the hydroxyethyl cellulose solution used in drawcasting had little to no effect on the obtained data. Although these differing surfaces would have different wetting relationships with the polymers, the effect on the force measurement was most likely below the

resolution limit of the rheometer. For this reason, the spherical indenter was not coated before each experiment.

For each experiment, it was first recorded whether the polymer filament was able to extend to 10 mm, corresponding to an aspect ratio of roughly 3 if the width of the drawn sample was defined by the initial diameter of the contact area. If a sample failed to attain the 10 mm extension, it was classified as a type I, II, or III failure. Type I failure was defined as the circumstance in which the spherical indenter separated from the molten film without drawing any material. This typically resulted in a depression in the molten film and no material transfer from the film to the indenter. This failure is an adhesive failure between the polymer melt and the probe. A type II failure was identified as when the indenter was able to draw up some of the molten film, but the polymeric bridge between the indenter and the base fractured in a glassy manner, resulting in some material on both the indenter and the bottom plate. Finally, a type III failure was defined as when the polymeric bridge between the indenter and the base experience a necking failure due to thinning of the bridge. This resulted in two distinct regions of material on the indenter and the bottom plate with pointed tips. The three failure types seen in these extensional measurements are shown in Figure 4.6.

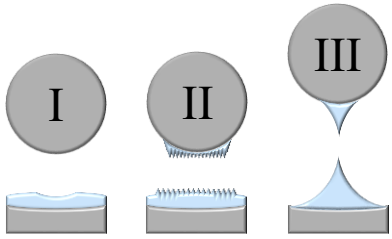

Figure 4.6. Adhesive failure (I), brittle fracture (II), and necking instability (III) observed in extensional experiments

For each “successful” measurement, data such as the cohesive strength and maximum stress could be determined from the resulting force-distance curve. The data from each experiment was truncated when the force decayed to zero after reaching its maximum. It should be noted that a force reading of zero on the rheometer did not mean that the polymeric bridge had broken. Under the majority of experimental conditions, the force reading decayed to zero early in the experiment, while the polymeric bridge was still intact after 10 mm of extension. In these cases, the force exerted by the polymer on the upper plate was below the resolution limit of the rheometer. The design of the environmental test chamber did not allow for monitoring of the evolution of the thinning polymeric bridge during extension, as opening the chamber doors would cause a sudden drop in temperature. It was therefore not possible to determine the degree of extension achieved by all the samples before failure.

An average or effective Weissenberg number was then calculated for each experimental condition using the material’s temperature-dependent relaxation time and an average deformation rate. The average deformation rate was defined as the pulling velocity divided by 600 μm. This distance was chosen in order to restrict the analysis to the period in which the probe is first coming out of the melt. Since the probe is lowered 300 μm into the melt, the observational period was extended to the point where the probe is 300 μm above the melt surface. The Weissenberg numbers for each material were plotted as a function of velocity, and the “failed” versus “successful” experiments were noted.

The force decay after reaching a maximum as a function of the gap in each experiment was fitted with an appropriate curve, and the cohesive strength of the melts in each experiment was determined by integrating the force-distance curves. The cohesive

strength of each material at the temperatures tested was then plotted as a function of velocity, and the data sets for each polymer were combined to reference temperatures using the shift factors obtained from the TTS performed in the shear rheological analysis.

As the success or failure of an extensional experiment as well as the geometry of a drawn structure were believed to be highly dependent on the contact area established before drawing, the effect of changing the dwell time and, effectively, the contact area on the axial force response during extensional measurements was also investigated. Experiments were performed in a similar manner to that described above using the 9508 elastomer at a constant temperature and velocity of 170 °C and 1000 μm/s, respectively. The probe was lowered 300 μm into the molten film in each experiment, while the dwell time was varied between 10 and 180 seconds. As the wetting rate was known to change with temperature, the results of the above experiments on 9508 at the full range of temperatures examined. A constant velocity and dwell time of 1000 μm/s and 10 seconds, respectively, were also plotted to compare the effects of changing the dwell time and changing the temperature on the adhesive and/or cohesive behavior of the polymer melt.

4.6. Sample Fabrication

4.6.1. Pattern Size Iterations

With each reduction of the pattern feature size, the difficulty of drawing structures increased, as the necessary degree of precision increases with smaller patterns. As discussed in Chapter 3, over- or under-dipping leading to drawing failure can occur in smaller-featured patterns at a much smaller angle of misalignment between the pattern and

polymer film than in larger-featured patterns. Furthermore, the precision in positioning of the top pattern relative to the molten film becomes more critical with smaller pattern features. The ability to visualize and precisely control both misalignments between the pattern and polymer film with the F-TIR system and the gap between the pattern and molten film before drawcasting ultimately limits the size of structures that can be produced. For this reason, the feasibility of producing structures via drawcasting with the range of pattern sizes—3-mm diameter ball bearings, 250- and 500-μm diameter BGAs, and 250-, 100-, and 50-μm diameter rounded micropillars—was first explored. Several samples were produced using the LDPE, 9108, and 9508 polymers and each type of upper pattern. The process variables in these experiments such at temperature, speeds, dwell times, etc., were not constant in all the samples produced, as the primary objective in fabricating these samples was to test pattern fabrication and leveling procedures and to demonstrate the versatility of the drawcasting system.

4.6.2. Process Parameter Iterations

A variety of micro-suction cup samples with different experimental conditions were then produced with each polymer of interest using the 500-μm diameter BGA patterns. Five sets of structures were produced for each polymer, with each set having one variable processing parameter while the others were held constant. In every experiment, a 650-μm thick film was used, and the dip depth was approximately 150 μm.

The first set of structures, “T” series, investigated the effect of changing the initial temperature of the base and pattern on the structure array. In this set, the draw speed and

draw height were held at 1000 µm/s and 500 µm, respectively, for all three polymers. The LDPE samples were drawn when the temperature of the system reached 130 °C, while the elastomer samples were drawn when the temperature of the system 160 °C. Dip temperatures ranging from 130 to 190 °C were used for LDPE, while dip temperatures between 160 and 190 °C were used for 9108 and 9508. The cooling time or dwell time before drawing in each experiment was noted.

The second set of structures, "S" series, investigated the effect of changing the draw speed. A constant dip temperature of 160 °C and draw temperature of 130 °C was used for the LDPE samples, while the 9508 and 9108 samples were produced with dip and draw temperatures of 190 and 160 °C, respectively. Draw speeds ranging from 10 to 20000 µm/s were investigated, while the draw height was kept at 500 µm. Again, the dwell time for each sample was noted.

The third set of structures, "D" series, investigated the effect of changing the draw temperature with a constant dip temperature. For each set of polymer samples, the dip temperature was held at 190 °C, while the draw temperatures ranged from 100 to 190 °C, resulting in a wide range of dwell times. The draw speed and draw height for each sample were held at 1000 µm/s and 500 µm, respectively.

The fourth set of structures, "I" series, investigated the effect of changing the dwell time with a constant dip and draw temperature. For each set of polymer samples, the dip and draw temperatures were held at 160 °C, while dwell times between 10 and 50 seconds were used. The draw speed and draw height were again held at 1000 µm/s and 500 µm, respectively.

The final set of structures, “H” series, investigated the effect of changing the draw height with constant dip and draw temperatures and draw speeds. The LDPE samples were produced with dip and draw temperatures of 160 and 130 °C, respectively, while the 9508 and 9108 samples used dip and draw temperatures of 190 and 160 °C. Each sample was drawn at 1000 µm/s at heights ranging from 250 to 1000 µm. The experimental conditions for each sample produced are listed in Table 4.3.

Table 4.3. Parametric Samples

Sample Set	Dip Temperature (°C)	Draw Speed (µm/s)	Draw Temperature (°C)	Draw Height (µm)	Dwell Time (s)
LDPE					
T	130-190	1000	130	500	Varies
S	160	10-20000	130	500	Varies
D	190	1000	100-190	500	Varies
I	160	1000	160	500	10-50
H	160	1000	130	250-1000	Varies
9108					
T	160-190	1000	160	500	Varies
S	190	10-20000	160	500	Varies
D	190	1000	100-190	500	Varies
I	160	1000	160	500	10-50
H	190	1000	160	250-1000	Varies
9508					
T	160-190	1000	160	500	Varies
S	190	10-20000	160	500	Varies
D	190	1000	100-190	500	Varies
I	160	1000	160	500	10-50
H	190	1000	160	250-1000	Varies

Similar to the extensional measurements discussed in Section 4.5.4.2, each of the experiments listed in Table 4.3 was noted as a “success” or “failure.” Cross sections were taken of select samples and images of the obtained structures were obtained with an optical microscope (Leica M165C).

CHAPTER 5. MATERIALS CHARACTERIZATION

The following sections detail the results of experiments characterizing selected material properties of ExxonMobil LGA 105 LDPE and Dow INFUSE 9108 and 9508 elastomers as they relate to the drawcasting process. The thermal, wetting, and rheological properties herein discussed are used both to establish limits on drawcasting process parameters and to serve as a basis for possible future analytical or numerical modeling.

5.1. Thermal Characterization

The results of the STA experiments on 9108, 9508, and LDPE are shown in Figure 5.1. The cooling and second heating segments of the DSC trace are shown, with crystallization indicated by the positive peak, as crystallization is an exothermic process, and melting indicated by the negative peak, as melting is endothermic.

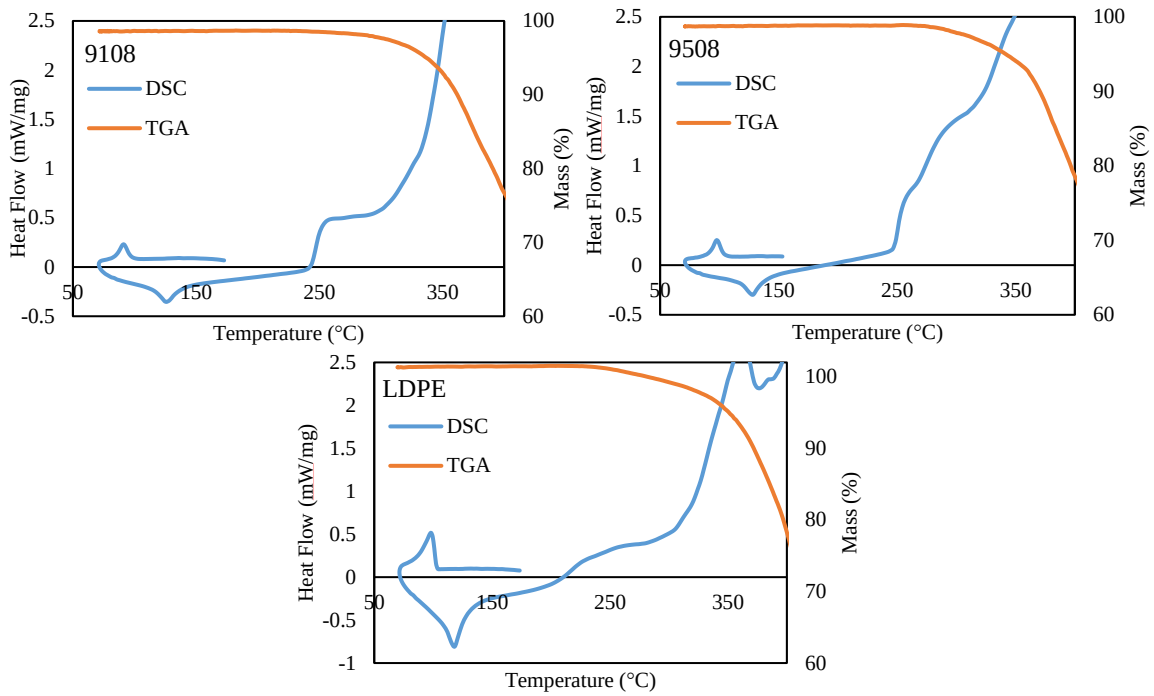

Figure 5.1. STA measurements on 9108, 9508, and LDPE

The melting temperature of each sample was defined as the temperature at the onset of the melting event on the DSC curve, while the degradation temperature was defined as the temperature at which the TGA curve began to deviate from 100%. The glass transition temperatures of all three of the polymers were below room temperature and not captured in these measurements. As drawcasting is a relatively high-temperature process, typically performed above the polymer's melting temperature, low temperature measurements such as those below room temperature were not performed. As stated in Chapter 4, the melting and crystallization peaks were integrated and used along with the heat of fusion of 100% crystalline PE in order to calculate the relative crystallinity of each sample. The glass transition, melting, and decompositions temperatures along with the relative crystalline content of each polymer is given in Table 5.1.

Table 5.1. Thermal Properties of 9108, 9508, and LDPE

Polymer	T_g (°C)	T_m (°C)	T_d (°C)	Crystallinity (%)
Dow 9108	<RT	125	310	6.3
Dow 9508	<RT	125	315	6.4
Exxon LDPE	<RT	110	245	29

The minimum dip temperature used in drawcasting is typically the polymer's melting temperature, as the mobility afforded to a melt enhances its wetting and flow properties, which will be discussed in the following sections. As such, a lower limit of 130 °C was employed for the dip temperature during drawcasting with the three polymers listed in Table 5.1. A slightly lower dip temperature could be used with LDPE films, but the limit of 130 °C was imposed for all the polymers for the sake of comparison. If a sufficient contact area is established between the polymer film and the pattern (which necessitates a dip temperature above T_m), the film may be drawn at a lower temperature. One might assume that the glass transition temperature would serve as the lower limiting draw temperature in drawcasting; however, drawcasting experiments at different ranges of dip and draw temperatures have indicated that the minimum draw temperature may be below the material's melt temperature, but it far exceeds its glass transition temperature. It is clear that the minimum draw temperature is restricted by the material's viscosity rather than its glass transition temperature. The results of rheological experiments will be discussed in later sections, while the results of drawcasting experiments will be detailed in Chapter 6.

5.2. Wetting Measurements

The change in contact area of 9508 elastomer on a 3-mm diameter sphere at 190 °C can be seen in Figure 5.2 at two different stages of the experiment.

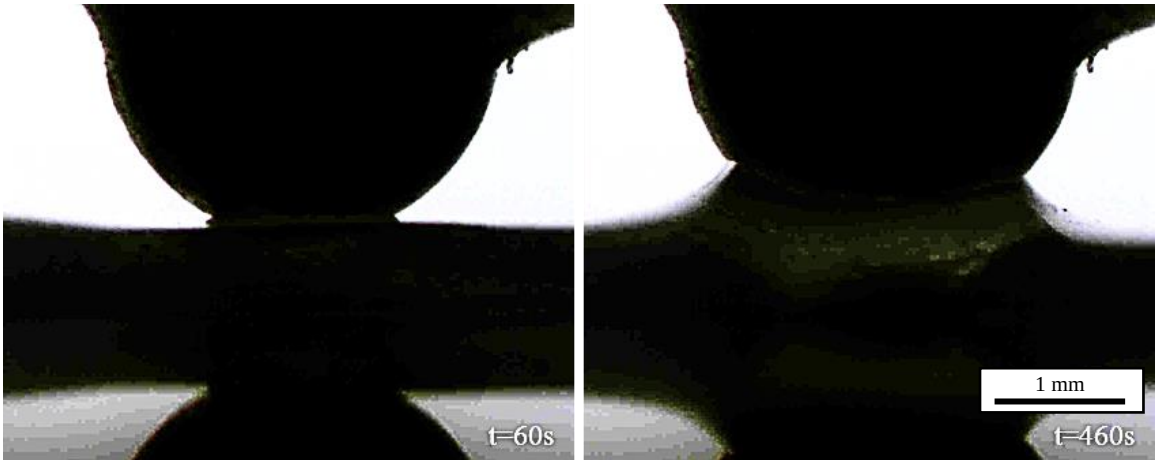

Figure 5.2. 9508 wetting at 190 °C

While each experiment was anticipated to begin as soon as the sphere contacts the molten film, some variation in the sphere position relative to the film occurred between experiments. For this reason, the contact area was normalized to the initial contact area of each experiment to account for any differences in the immersion or dip depth. The results of the wetting experiments on the elastomer and LDPE films are shown in Figure 5.3, with the first 100 seconds of each experiment pictured in the inset to highlight the initial, roughly linear portion of each plot.

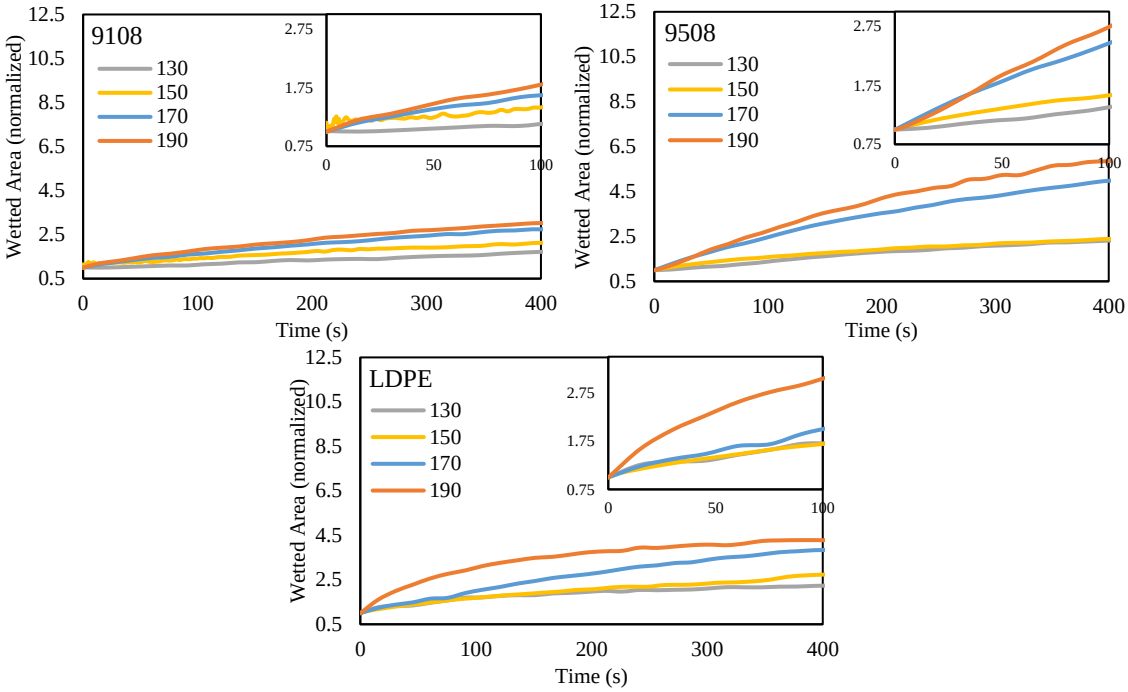

Figure 5.3. Wetting measurements on 9108, 9508, and LDPE

The wetting rate of each polymer sample increased with increasing temperature, as the viscosity of the polymer decreases with temperature, heightening its mobility. As stated in Chapter 4 Equation 4.19, the wetting rate is proportional to the polymer's surface tension and inverse viscosity. In general, a material's surface tension decreases with increasing temperature, as does its viscosity. As the wetting rates shown in Figure 5.3 increase with increasing temperature, the change in viscosity with respect to temperature has a more pronounced effect than that of surface tension. As such, it is possible to reach the same given contact area at a relatively low temperature with a long dwell time or at a higher temperature with a shorter dwell time. The wetted area in each experiment eventually reaches a plateau, indicating that the contact angle between the melt and sphere reached its equilibrium value, and consequently the contact line stopped moving. In terms of the drawcasting system, for a given polymer, temperature, and initial contact area (or dip

depth), there exists a dwell time beyond which the contact area between the polymer and pattern does not increase.

As the dip depth between measurements was non-constant and the data had to be normalized, this data is more useful for qualitative comparisons to other drawcasting results discussed later in this chapter and in Chapter 6. The dip depth establishes the initial contact angle and how far that angle is from its equilibrium value. A more controlled or sophisticated measuring technique could ostensibly allow one to target a specific wetted area or eventual cup volume at a given set of drawcasting conditions. However, measurement of the contact angle of a molten polymer is notoriously problematic, and there are surprisingly few examples in literature of this type of measurement.

In a typical contact angle or wetting measurement, a droplet of low-viscosity liquid such as water or some other liquid with a known surface energy is dispensed onto a surface in a controlled volume [137]. The viscoelasticity of polymer melts precludes them from being dispensed in this manner using any sort of practical or commonly available equipment [156,166]. The most common method found in literature for measuring the changing contact angle and area of molten polymers is to observe the melting of polymer spheres or pellets on a surface in a closed furnace to mitigate thermal gradients [139,140,167,168]. The measurement technique employed in this work was developed to more closely mimic the wetting phenomena in the drawcasting system, as there are inherently temperature gradients and non-ideal geometries in the process itself. The effect of the curvature of the spherical probe used as the wetting surface is thought to play a minimal role, as the effect of gravity on the polymer melt at this scale is negligible, meaning the same wetting measurement (with respect to temperature and initial contact angle) on a 3-

mm diameter sphere. A 500-μm diameter sphere would be very similar, if not identical [171,172].

5.3. Rheological Characterization

5.3.1. Shear Rheology

5.3.1.1. Amplitude Sweeps

Small amplitude oscillatory shear (SAOS) measurements were then performed on the three polymers of interest at a range of temperatures. SAOS, along with appropriate rheological models such as the Cox-Merz Rule and Carreau-Yasuda model discussed in Chapter 4, can be used to determine a variety of viscoelastic material properties. Most notably in this work, frequency sweeps of each material at different temperatures were performed in order to determine the polymers' relaxation times and zero-shear viscosity values at the range of temperatures probed. To correctly ascertain these values, SAOS frequency sweeps must be performed at a strain amplitude within the polymer's linear viscoelastic envelope (LVE), in which the stress response is linear with respect to applied strain. Amplitude sweeps were performed on each polymer at a constant frequency at both 130 and 200 °C in order to define the LVE. The results of these measurements on the 9508 elastomer are shown in Figure 5.4.

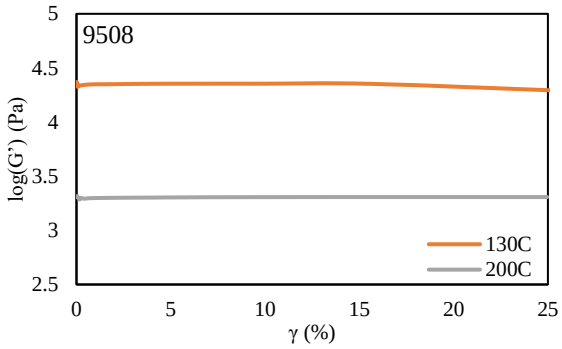

Figure 5.4. Amplitude sweeps performed on 9508

Strain amplitudes were then chosen for frequency test from each set of experiments to ensure the sample was in its LVE at the test temperature.

5.3.1.2. Frequency Sweeps

Frequency sweeps were then performed on each polymer sample at temperatures from 130 to 200 °C. The storage and loss moduli (G' and G'') as well as the complex viscosity (η*) were recorded as a function of frequency at each temperature. Examples of frequency sweeps performed on each material at 160 °C are shown in Figure 5.5, and the frequency sweeps performed at other temperatures are plotted in the Appendix.

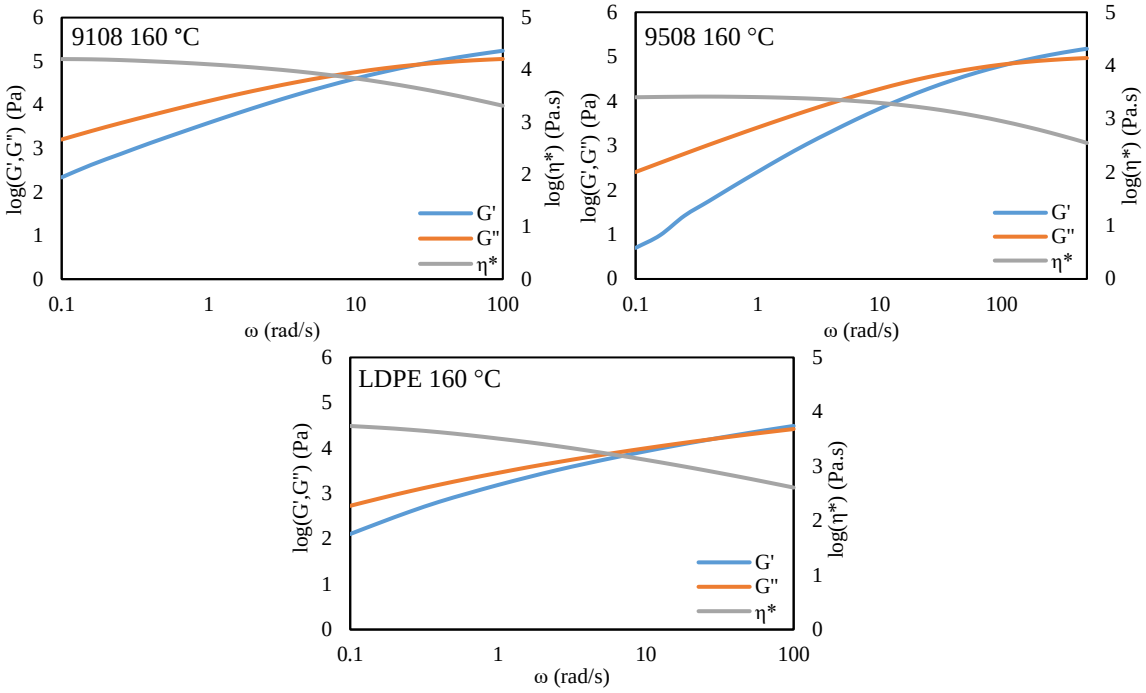

Figure 5.5. Frequency sweeps at 160 °C on 9108, 9508, and LDPE

The frequency at which the storage and loss modulus cross another denotes the point beyond which the polymer behaves as an elastic solid rather than a viscous fluid. The inverse of this crossover frequency is defined as the polymer's relaxation time. As the polymer exhibits different behavior before and after the crossover frequency from which the relaxation time is determined, the relaxation time is generally associated with large-scale changes in the polymer's structure. The relaxation times obtained from the frequency sweeps on each polymer at the range of temperatures tested are plotted as a function of temperature in Figure 5.6.

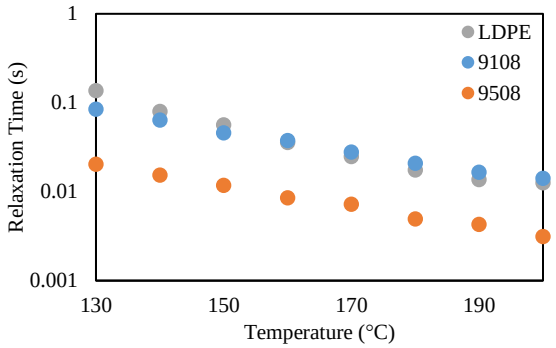

Figure 5.6. Temperature-dependent relaxation times of 9108, 9508, and LDPE

In each material, the relaxation time decreases with increasing temperature, meaning that the viscous-to-elastic behavior transition occurs at higher frequencies at higher temperatures. As molecular chains are more mobile at higher temperatures, the polymer can still viscously dissipate energy at higher frequencies compared to that at a lower temperature. Correspondingly, the structure of the polymer changes more quickly at a higher temperature, which is exemplified by a lower relaxation time.

5.3.1.3. Time-Temperature Superposition

The frequency sweeps of each polymer at a range of temperatures resulted in a large amount of data, with eight data sets for each of the three polymers. The data for each polymer can be combined to a single master curve at a reference temperature using shift factors according to the time-temperature superposition (TTS) principle, detailed in Chapter 4. Additionally, changing the experimental temperature has the same effect on the polymer as does changing the shear rate or frequency, so combining the data using shift factors effectively extrapolates the low (high) temperature data to low (high) frequencies at the reference temperature. The first plot of Figure 5.7 depicts the G' dependence of the

9108 elastomer on frequency at the eight temperatures tested. The data is then shifted to a reference temperature of 160 °C in the second plot of Figure 5.7. The inset of this plot depicts the shift factors, a_T, at their corresponding temperatures, along with the Arrhenius fit to the data.

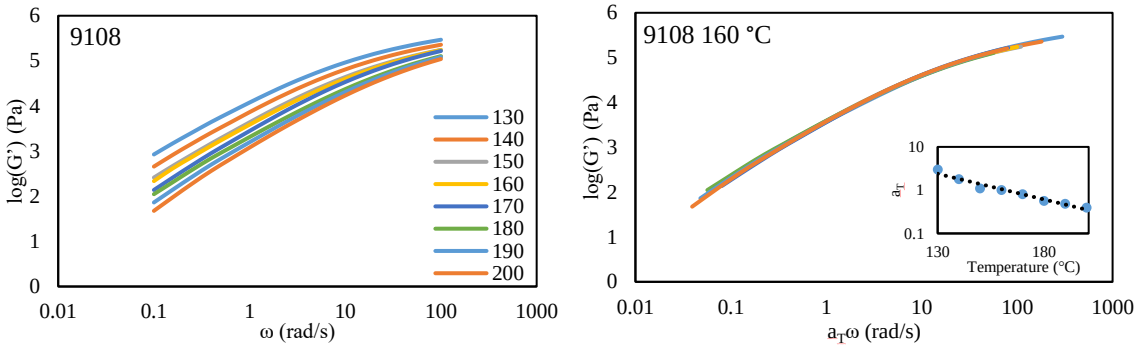

Figure 5.7. 9108 frequency sweeps and TTS at 160 °C

The TTS on the 9108 elastomer shown in Figure 5.7 was performed manually to demonstrate the efficacy of the principle. The Arrhenius fit to the horizontal shift data yielded an activation energy of 43.49 kJ/mol for the 9108 elastomer. The frequency data for 9508 and LDPE were subsequently combined to master curves using an automatic TTS function in Trios software (TA Instruments). The resulting curves, both at a reference temperature of 160 °C, are depicted in Figure 5.8, with the temperature-dependent shift factors and the corresponding Arrhenius fits plotted in the insets.

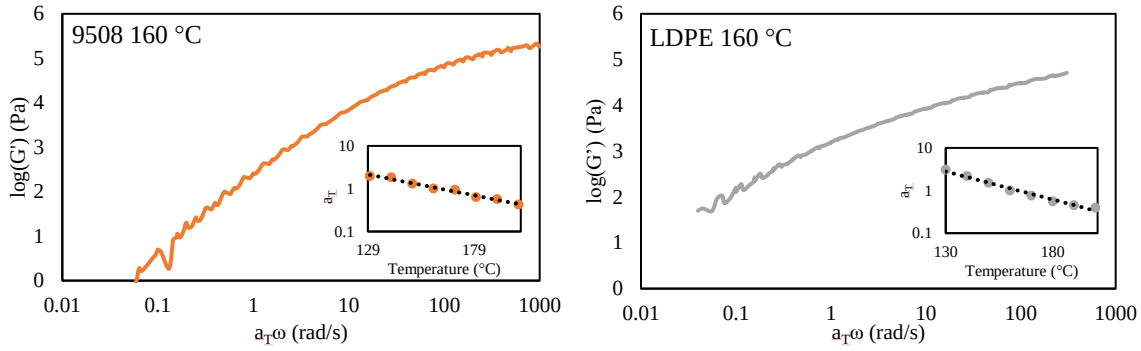

Figure 5.8. 9508 and LDPE TTS at 160 °C

The fitting of the Arrhenius model to the 9508 and LDPE shift factor data resulted in activation energies of 34.98 and 47.37 kJ/mol, respectively. As stated, TTS is performed not only to simplify the data, but also to extend the data to frequency ranges not probed experimentally. The shift factors obtained from TTS are particularly useful, as they can be used to compile master curves of temperature-dependent data sets other than SAOS frequency sweeps, as will be demonstrated in later sections.

5.3.1.4. Application of Rheological Models

Oscillatory data can be transformed to time-dependent data through the Cox-Merz relation, given in Chapter 4 Equation 4.17, which relates steady state and dynamic viscosity at similar shear rates and frequencies. The frequency-dependent data detailed in 5.3.1.2 was converted to steady state viscosity through the Cox-Merz relation for each material and range of temperatures. The steady state viscosity at 160 °C is plotted in Figure 5.9 as a function of shear rate, while the steady state viscosity at other temperatures is plotted in the Appendix.

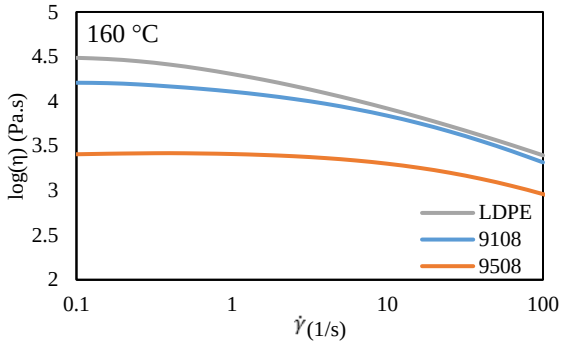

Figure 5.9. Steady state viscosity versus shear rate plots at 160 °C for 9108, 9508, and LDPE

The viscosity of each material was found to decrease with increasing shear rate, indicating that the three polymers used in this study were shear thinning. At low shear rates, the viscosity plateaus and finally reaches a constant value known as the zero-shear viscosity (η_0). A model is typically fit to $\eta(\dot{\gamma})$ plots in order to extrapolate the data to zero shear rate. The Carreau-Yasuda model, defined in Chapter 4 Equation 4.18, was fitted to the $\eta(\dot{\gamma})$ plots of each material at the range of temperature investigated in order to obtain each polymer's temperature-dependent zero-shear viscosity. The obtained values are plotted in Figure 5.10.

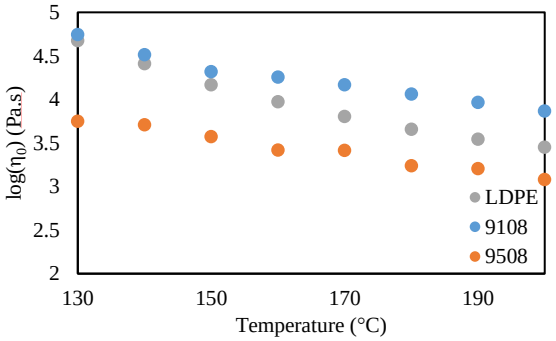

Figure 5.10. Zero-shear viscosity versus temperature plots for 9108, 9508, and LDPE

As do the relaxation times, the zero-shear viscosity of each polymer tested decreases with increasing temperature. The relationships between zero-shear viscosity or relaxation time and temperature are useful for comparison with other temperature-dependent behavior or data, as they are not dependent on any other experimental conditions such as elapsed time or frequency.

5.3.2. Tack Measurements

5.3.2.1. Adhesive vs. Cohesive Failures and Correlation with Shear Rheology

Tack or extensional measurements were then performed on each of the polymers of interest at a range of extensional velocities and temperatures. As described in Chapter 4, an 8-mm diameter sphere was brought in contact with a molten film, and the axial force was recorded as a function of the gap as the sphere was drawn upward from the film at a constant velocity. Table 5.2 lists the tack experiments performed. Experiments in which the polymer filament was able to stretch to a final length of 10 mm are shaded in green, while experiments in which the polymer filament ruptured or did not adhere to the spherical probe are shaded in red with the failure mode noted.

Table 5.2. Tack Measurements on 9108, 9508, and LDPE

	Velocity (μm/s)	Temperature (°C)							
		130	140	150	160	170	180	190	200
9108	50								
	100								
	500	I	I	I	I				
	1000					II	I		
	5000					I		II	
	10000							I	
9508	50								
	100								
	500								
	1000								
	5000	I	I						
	10000								
LDPE	50								
	100								
	500								
	1000								
	5000	II	II						
	10000	I	I						

As discussed in Chapter 4, the experiments in which the polymer filament was not able to stretch to a final height of 10 mm were classified by their failure mechanism. A type I failure, defined as when the spherical indenter makes an impression on the polymer film but fails to draw up any material, is indicative of an adhesive failure between the melt and the probe. These failures are seen most often in Table 5.2 at higher velocities and are more prevalent at lower temperature than other types of failures. The adhesive failure occurs when the viscosity of the polymer is too high to form a sufficient contact area with the

spherical probe or to deform in response to the pulling of the probe. In these cases, the film exhibits the behavior of a purely elastic solid.

As has been discussed, polymers can behave as elastic solids not only at low temperatures, but at sufficiently high deformation rates as well. This is exemplified by the sets of experiments at constant temperatures in which a type I failure occurs at higher rates. For example, at 140 °C, the 9508 elastomer was able to be drawn to 10 mm at velocities ranging from 50 to 1000 μm/s, but a type I failure is seen when the velocity is increased to 5000 μm/s. This indicates that, similar to the temperature-dependent G'/G'' crossover frequency measured in SAOS, there exists an extensional velocity below which the polymer behaves as a viscous liquid and above which it behaves as an elastic solid and is unable to be extended or drawn. Furthermore, this limiting velocity is clearly also temperature-dependent, as the type I failures occurring in Table 5.2 are not at a constant velocity across the entire temperature range investigated.

When considering the temperature dependence of the zero-shear viscosities and relaxation times of the three polymers investigated in section 5.3.1, the temperature and velocity dependence of the failures in the tack measurements are mostly consistent. At higher temperatures, the relaxation time is lower, meaning that tan $\delta=1$ occurs at higher frequencies. As such, the bond between the melt and the probe can be upheld at higher velocities at a high temperature than those same velocities at a lower temperature.

Type II failures were defined by a glassy fracture in the polymeric filament, meaning the spherical probe was able to draw some polymer up from the film, but the bridge fractured before it could be drawn further. This type of failure is a cohesive failure within the polymer, but it reflects a strong elastic response of the material. Type II failures

inevitably lead to type I failures with increasing velocity because in a type II failure, some viscous deformation occurs, but at higher velocities, the viscous response is be dampened. This is evidenced in the shear frequency sweeps performed in 5.3.1, in which the loss modulus reflecting the viscous response of the polymer decreased with frequency at every temperature. No type III failures were observed in this set of tack measurements, as the failure mechanism was defined at the moment the extension was complete. However, if the stretched polymer filament is allowed to dwell above its melting temperature, the bridge will eventually thin and exhibit necking failure as described in Chapter 4.

The relative Weissenberg numbers calculated for each experiment in Table 5.2 are shown in Figure 5.11.

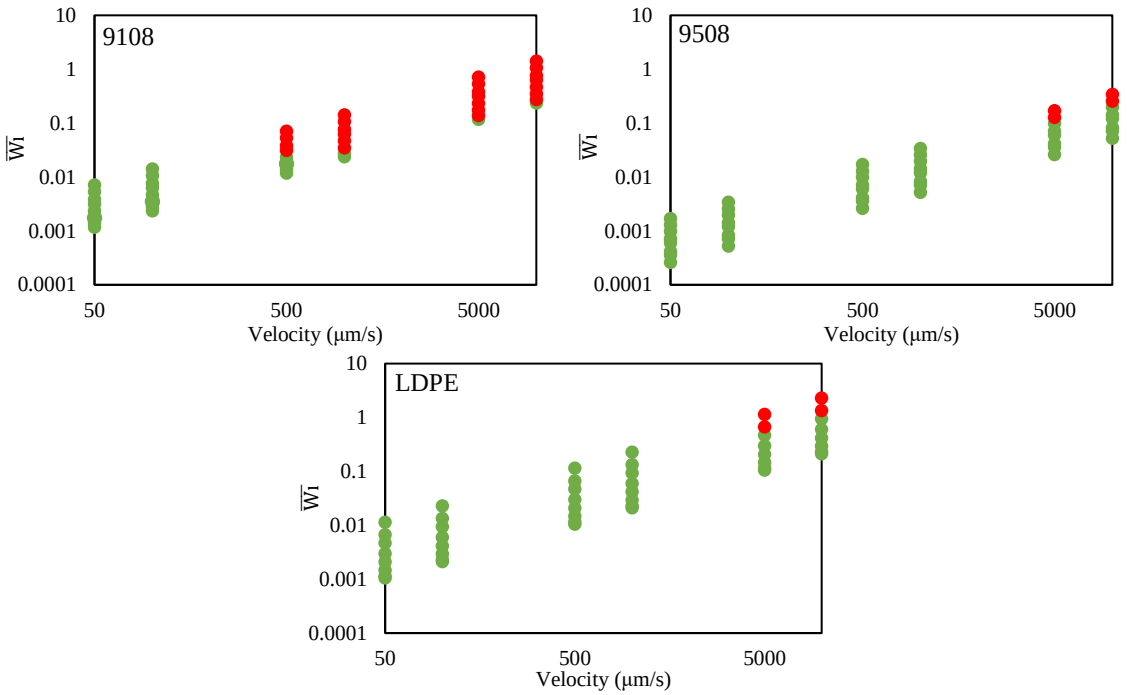

Figure 5.11. Average Weissenberg number versus velocity plots for 9108, 9508, and LDPE

In Figure 5.11, the successful extensional experiments are plotted with green dots, while the experiments exhibiting adhesive failure are plotted with red dots. This data indicates that there is a critical Weissenberg number, independent of velocity and temperature, above which, drawing in the current configuration is not possible. This critical Weissenberg number would still be dependent on a number of experimental factors including the immersion depth of the probe in the melt and the time the probe is permitted to dwell in the melt before being raised. These caveats are also present in conventional probe-tack tests performed on pressure-sensitive adhesives, and consequently the test methods for PSAs are not standardized and are heavily debated. As the Weissenberg number is a product of a material's relaxation time and the imposed deformation rate, raising the temperature will lower the Weissenberg number, promoting a viscous response and facilitating deformation. Conversely, raising the deformation rate would increase the Weissenberg number, evoking a more elastic response from the polymer melt.

5.3.2.2. Force Measurements and Time-Temperature Superposition

The force response at each experimental condition was plotted with respect to the increasing gap between the probe and the base. An example of these plots for each polymer at 160 °C are shown in Figure 5.12. The results of experiments performed at other temperatures are plotted in the Appendix.

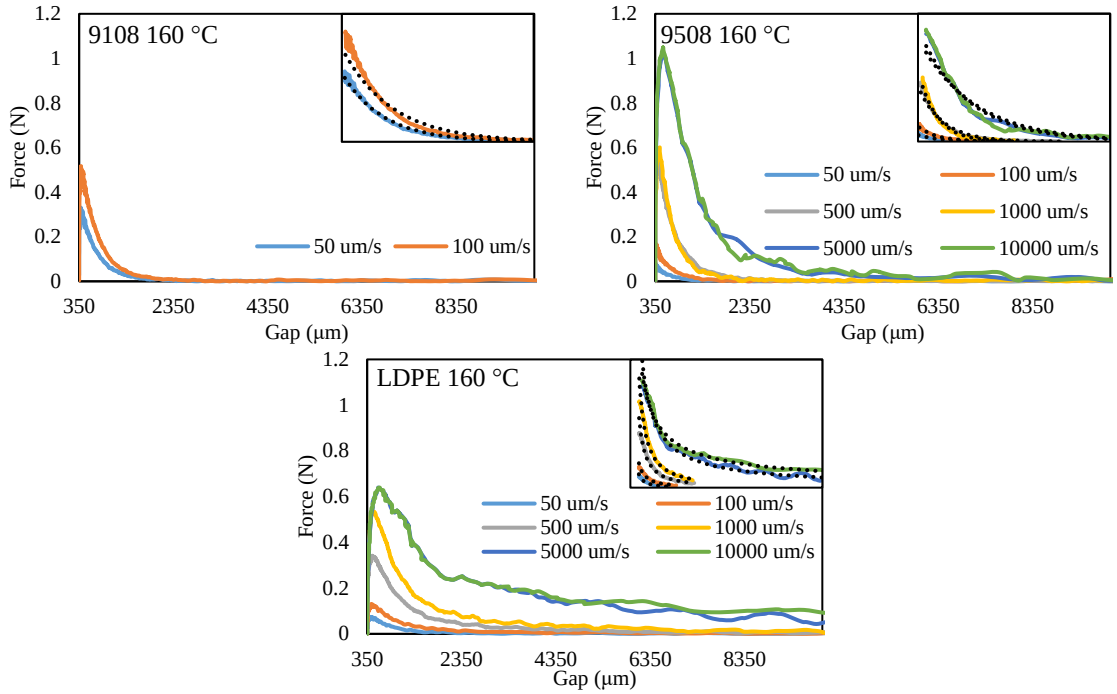

Figure 5.12. Axial force versus distance plots at 160 °C for 9108, 9508, and LDPE

As discussed in Chapter 4, the local maximum of the tensile force is correlated to the onset of necking instability in the polymer melt. Before the onset of necking, the deformation of the polymer in response to the moving probe is roughly homogeneous. As is evidenced most strongly in the LDPE plot, the onset of necking is slightly delayed at higher deformation rates, which further reflects the increasing elastic behavior of the melts with increasing extensional velocity.

The plots presented in Figure 5.12, as well as the remaining plots in the Appendix, can be split into two regimes: before and after the maximum in the axial force. As the decay of the axial force with increasing gap after the onset of necking is closely related to the thinning of the polymer filament, this regime is of particular interest regarding the drawcasting process. The thinning behavior of the filament with temperature, deformation velocity, and position will dictate the final geometry of a drawn structure. The insets of

each plot in Figure 5.12 depict the force decay with increasing gap at each experimental velocity. In these plots, the curves are truncated to the point where the force first reaches zero. Trend lines were added to each of these curves to highlight the apparent rate of force decay in each experiment. The force decay of both the 9108 and 9508 elastomer displayed exponential behavior, while the LDPE samples exhibited force decay obeying a power law.

In the plots of 9108 and 9508, the force decay to zero occurs over a narrower relative gap change than the LDPE, indicating that the rate of necking or filament thinning in the elastomers is higher than in LDPE at comparable deformation conditions. Additionally, the plateauing of the axial force in the LDPE experiments at higher velocities after the initial force drop is indicative of strain hardening in the material. This strain hardening is most likely a result of molecular branching, which causes chain entanglements in extension to lock up more readily than in linear polymers. The apparent lack of strain hardening in 9108 and 9508 at the velocities investigated indicates either a lack of or a much lower degree of branching in comparison to the LDPE samples. The branching present in LDPE and not in the elastomers could also be responsible for the difference in the force decay trends. The source of these trends may be elucidated with extensional viscosity testing of the polymer melts, in which a constant strain rate is applied to the polymer rather than a constant velocity. These experiments were not conducted in the present work, as a constant extensional velocity was used to mimic the conditions employed in the drawcasting process.

The plots of force versus gap for each successful experiment denoted in Table 5.2 were then integrated to determine the polymer's cohesive strength at each experimental

condition. The cohesive strength of each polymer is plotted in Figure 5.13 with respect to the elongational velocity at 160 °C.

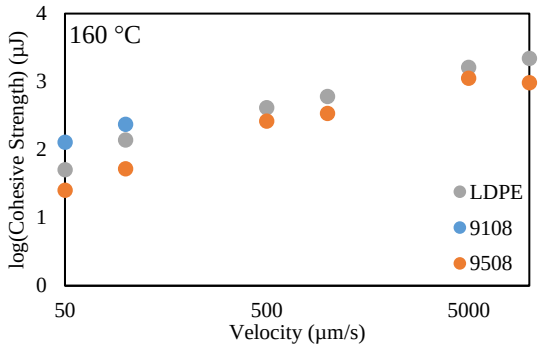

Figure 5.13. Cohesive strength versus velocity plots at 160 °C for 9108, 9508, and LDPE

In each polymer sample, the cohesive strength increases with velocity. With an increasing speed or rate of deformation, the melt exhibits an increasingly elastic response, as indicated by the increase in the storage modulus with frequency in the SAOS frequency sweeps shown in section 5.3.1.2. Accordingly, Figure 5.14 shows that the cohesive strength as well as the storage modulus decreases with increasing temperature at a constant velocity and frequency, respectively.

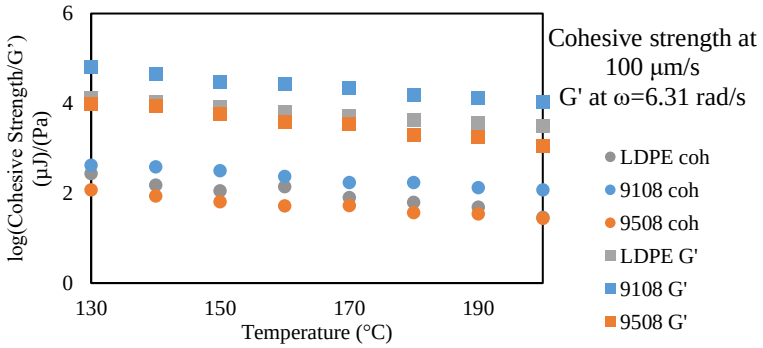

Figure 5.14. Cohesive strength and storage modulus versus temperature plots at constant velocity and frequency for 9108, 9508, and LDPE

This increase in cohesive strength with velocity or decrease with temperature is analogous to a respective increase or decrease in the melt's resistance to deformation. The increase in cohesive strength with increasing velocity at a constant temperature, originating from the increase in the storage modulus, eventually leads to the filament failures at high velocities documented in Table 5.2. Similarly, the decrease in cohesive strength with temperature at a constant velocity, originating from the decreasing storage modulus, allows the polymer to successfully be drawn at a given velocity at higher temperatures when drawing was not possible at the same velocity and a lower temperature.

Extensional measurements were then performed on the 9508 elastomer at a constant temperature and velocity of 170 °C and 1000 µm/s, respectively, with dwell times varying from 10 to 180 seconds. Similar to that of Figure 5.13, data from measurements on the 9508 elastomer was replotted with respect to temperature using the values of cohesive strength obtained at different temperatures and a velocity of 1000 µm/s. The results of these measurements are shown in Figure 5.15.

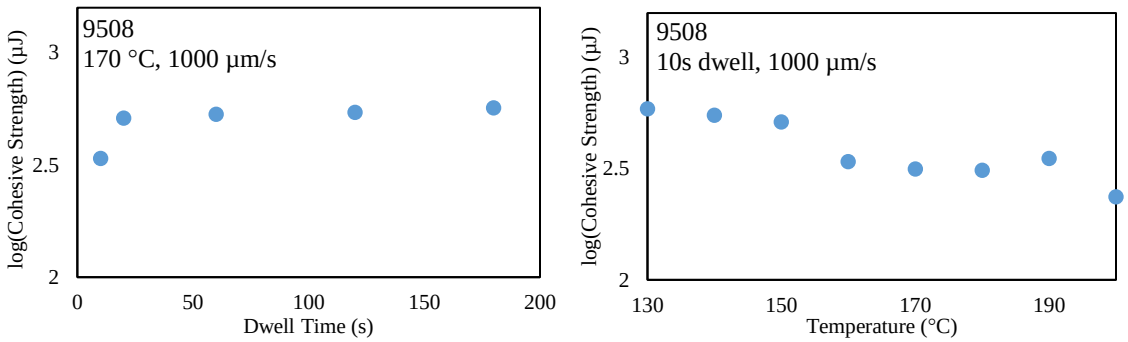

Figure 5.15. Cohesive strength of 9508 versus dwell time at constant temperature (left) and versus temperature at constant dwell time (right)

In first second set of experiments, the temperature was held constant, while the contact areas in each experiment increased with longer dwell times. In the second set of experiments, the dwell times were all held constant at 10 seconds, but the contact areas in each experiment were also different due to the dependence of the wetting rate of the polymer melt on temperature. As wetting rate increases with temperature, the contact area with a constant dwell time increases with temperature as well.

In first plot of Figure 5.15, the cohesive strength is shown to increase with dwell time, exhibiting slightly logarithmic behavior. This behavior is reflective of the wetting rate of the polymer, which initially increases rapidly and subsequently reaches a steady state. In this set of experiments, the viscoelastic behavior of the polymer was the same in each case, as the temperature and the velocity were held constant between experiments. The measured increase in cohesive strength was purely due to the changing contact area, as deforming the probe with a larger contact area is effectively deforming a larger volume of material, and the resistance to deformation accordingly increases. However, a larger contact area also means that there is a stronger adhesive force between the melt and the probe. In each case, this adhesive force between the melt and probe exceeded the melt's cohesive resistance to deformation.

In the second plot of Figure 5.15, the cohesive strength is shown to decrease with increasing temperature, which reflects the melt's decrease in viscosity and lower resistance to extensional deformation. The decrease in the measured cohesive strength with temperature despite an increasing contact area indicates that the reduction in viscosity has a much more notable effect on the melt behavior than do the contributions to the contact area.

As the extensional measurements on the three polymer samples generated a large amount of data that was dependent on both time and temperature, the cohesive strengths measured in each experiment was plotted with velocity, and the time-temperature superposition method was again used to collapse the data to a single reference temperature of 160 °C for each polymer. The shift factors generated from the TTS performed in 5.3.1.3 were used to shift the curves from each experimental temperature to a new velocity. Figure 5.16 illustrates the TTS process performed on the 9108 polymer.

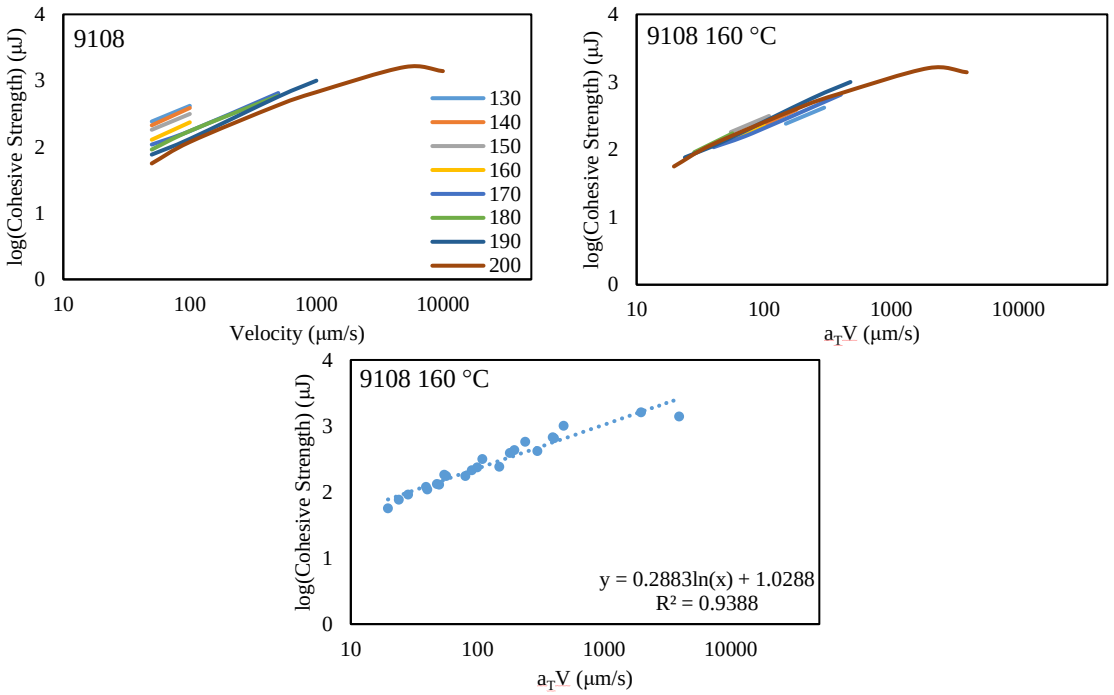

Figure 5.16. TTS of cohesive strength of 9108 with respect to velocity at 160 °C

The first plot in Figure 5.16 depicts the dependence of the cohesive strength of 9108 on velocity for each experimental temperature. The same data is replotted in the second frame of Figure 5.16 with respect to the new shifted velocities, $a_T V$, at each temperature. As it was evident that the data now lay on a single curve, a trend line exhibiting a logarithmic

dependence on velocity was fit to the data. Using this trend line, the data could be extrapolated to higher or lower velocities at 160 °C, or it could be used in conjunction with the horizontal shift factors to extrapolate the data to new velocities and temperatures. These extrapolations would hold true for temperatures at which the material is in the same phase, i.e., between T_m and T_d, and for velocities in which the material exhibits a primarily viscous response.

This process was repeated using the extensional data for the 9508 elastomer and LDPE. The resulting plots are given in Figures 5.17 and 5.18.

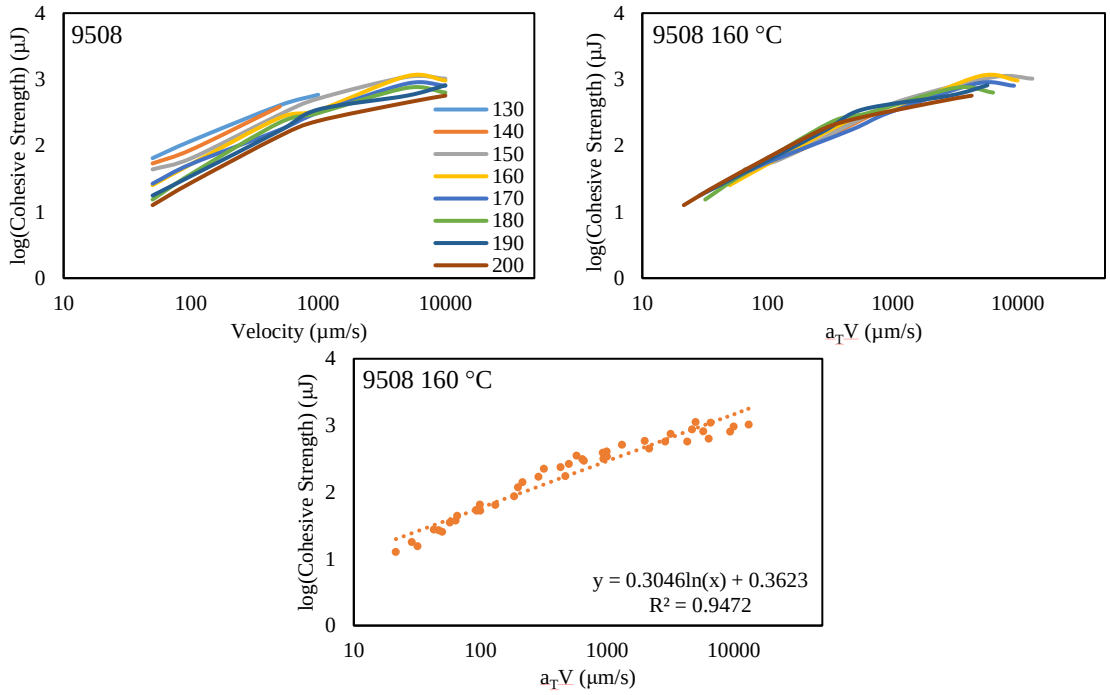

Figure 5.17. TTS of cohesive strength of 9508 with respect to velocity at 160 °C

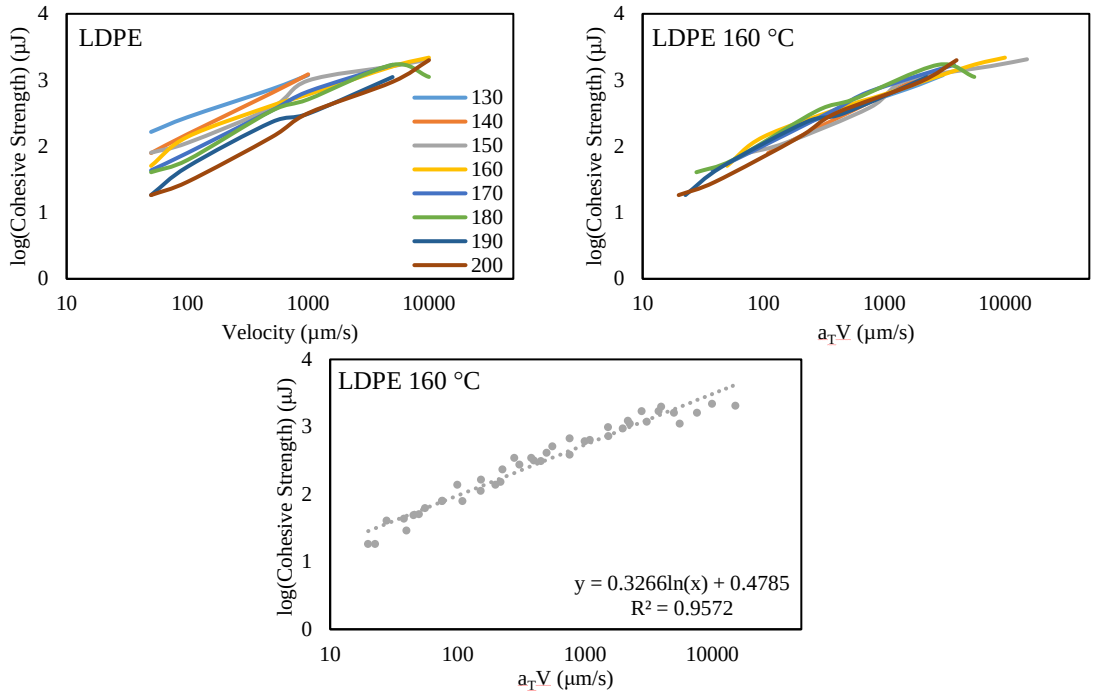

Figure 5.18. TTS of cohesive strength of LDPE with respect to velocity at 160 °C

The cohesive strength of all three polymers exhibited a power law dependence on velocity at the temperatures investigated. The equations for each power law fit are given on the respective plots along with an "R^2" value, which indicates the variance of the data from the trend line. This value is often referred to as the "coefficient of determination," with a value of one being a perfect fit. The high R^2 values for each trend line (greater than approximately 0.94 in each case) support the veracity of the experimental data as well as the extension of TTS to elongational data using shift factors obtained in shear measurements.

CHAPTER 6. SAMPLE FABRICATION

The following sections showcase a variety of micro-suction cup samples produced using the drawcasting process. Samples were first produced at a range of sizes corresponding to the patterns described in Chapter 3 in order to test the pattern fabrication procedures and refine the patterns or process as needed. Samples were then produced at a constant size with varying processing parameters. Sets of samples were fabricated in which one parameter varied while the rest were held constant in order to ascertain the effect of a given parameter on the ability to draw an array of cups and the resulting cup structure. At the end of this chapter, samples produced using the drawcasting system with a variety of patterns, methods, and materials other than those discussed in the bulk of this work are presented.

6.1. Size Iterations

Micro-suction cup arrays were drawn with hemispherical and rounded micropillar patterns with pattern element diameters ranging from 3 mm to 100 μm. The samples depicted in this section are meant to serve as a representative of the varying structure arrays fabricated with a given pattern size. Differences in the geometry of structures produced as they relate to the various process conditions were not quantified in this work, as restrictions in measurement capabilities such as the lack visualization during extensional measurements and the uncertainty associated with melt wetting experiments do not allow

for direct analytical comparisons. However, qualitative observations as they relate to the measured material properties are discussed.

Samples were first drawn using the 3-mm diameter ball bearing patterns from 9108, 9508, and LDPE molten films. A sample was produced in each material at the same process conditions. The heaters were held at 160 °C during drawing, and the pattern was held isothermally for 40 seconds in the melt before being raised 1 mm at 1 mm/s. The obtained structures are shown in Figure 6.1 with measurements of selected structural features to highlight the disparity between the three samples.

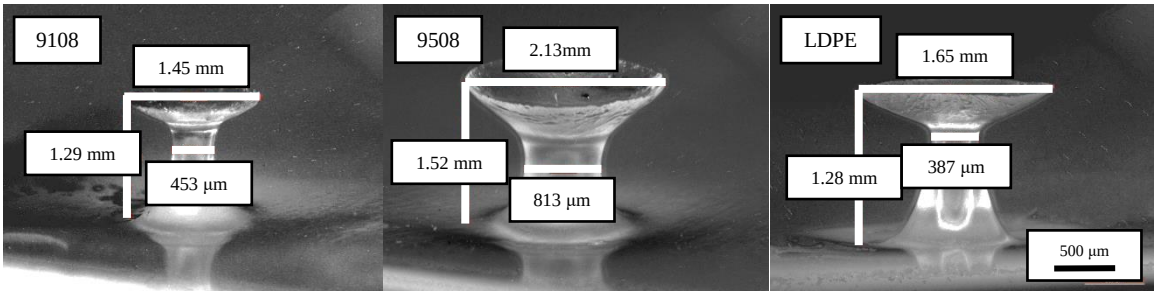

Figure 6.1. 9108, 9508, and LDPE micro-suction cups drawn with 3-mm diameter patterns

The differences in the cup diameter and overall height between the three samples are due to a combination of the different wetting rates and necking behavior of the materials, discussed in the previous chapter, as well as slightly differing dip depths between process runs. As discussed in Chapter 3, the current configuration of the drawcasting testbed only allows the dip depth to be monitored by viewing the approach of the pattern toward the melt from its side. Precisely monitoring the gap between the molten polymer film and patterns becomes more difficult with decreasing pattern size, as the overall gap between the upper and lower components of the drawcasting testbed becomes smaller and more difficult to visualize.

Samples were then drawn using 500-µm diameter BGA patterns. Structures were typically drawn to the same height as the diameter of the pattern feature used. Two samples drawn from LDPE films with different drawing parameters are shown in Figure 6.2.

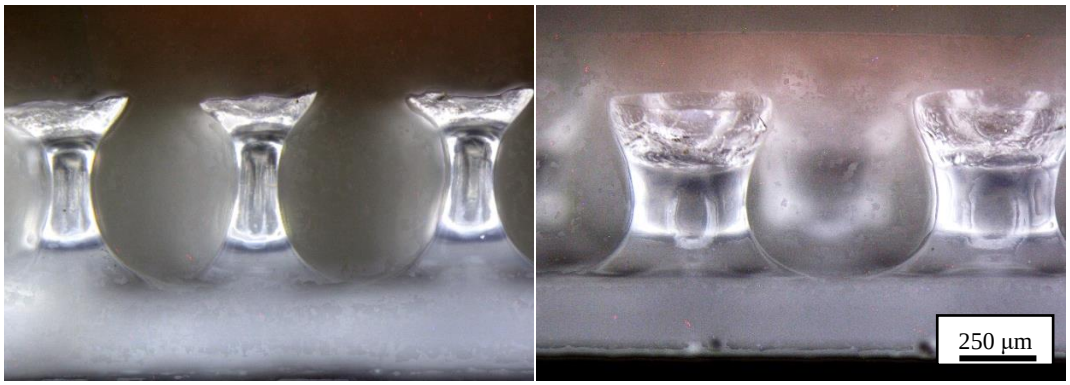

Figure 6.2. LDPE micro-suction cups drawn with 500-µm diameter patterns

The structure in the first image of Figure 6.2 was drawn at 150 °C and 5 mm/s and a 20-second dwell, while the second structure was drawn at 140 °C and 1 mm/s with no dwell. These samples were produced to demonstrate the ability to draw a wide range of structure geometries with the same material by changing the processing parameters. Arrays of 500-µm samples were also drawn using the 9108 and 9508 elastomers, which are shown in Figure 6.3. Finally, a side view of the drawing process with a 500-µm diameter pattern and LDPE film is given in Figure 6.4.

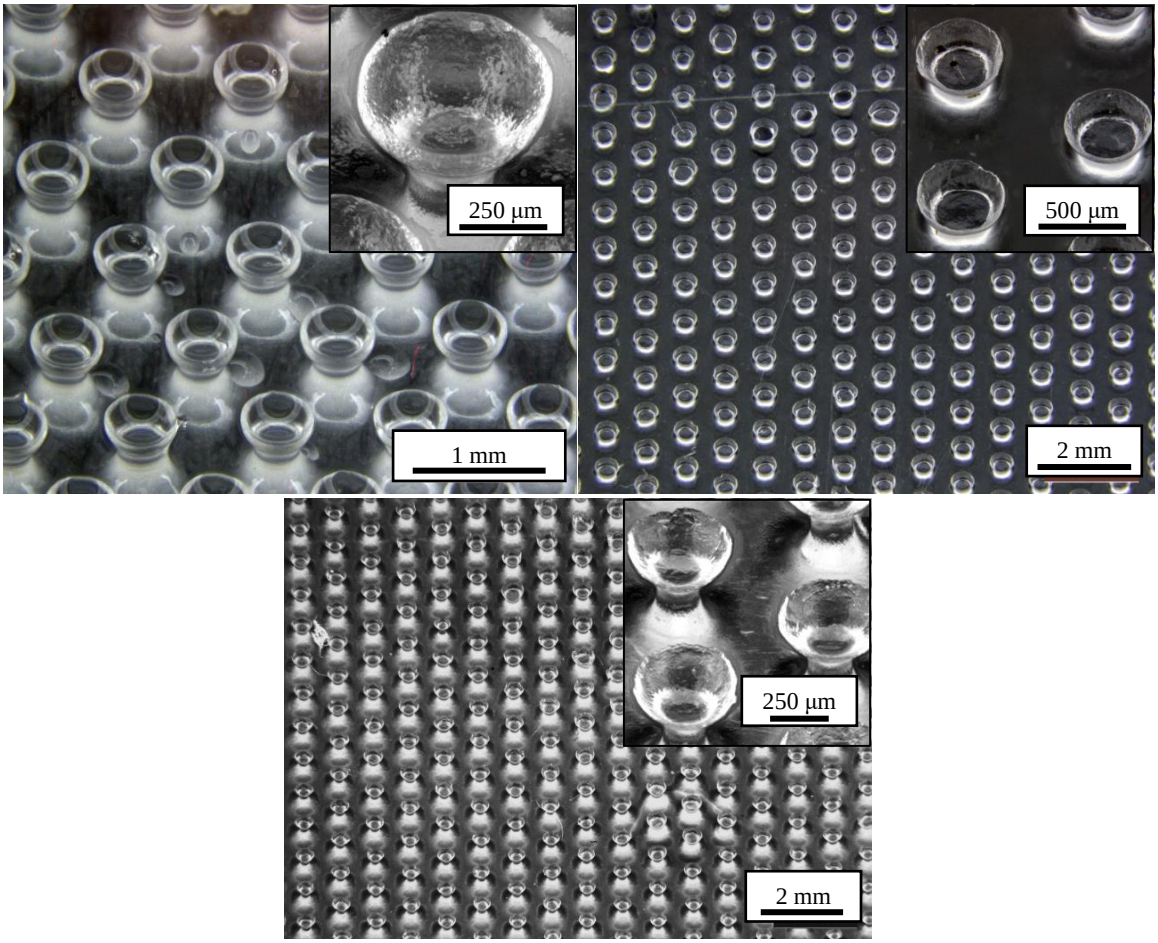

Figure 6.3. 9508 (top) and 9108 (bottom) micro-suction cup arrays drawn with 500-µm diameter patterns

Figure 6.4. LDPE drawing with 500-µm diameter pattern

Structures were then drawn using both the 250-µm diameter BGA patterns and rounded micropillar patterns. While the 3-mm and 500-µm diameter patterns could be leveled to the molten films to some extent by eye, patterns 250 µm in diameter and below

relied entirely on the F-TIR system for leveling. The gap between the pattern and polymer film as well as the dip depth was again approximated using the microscope providing a side view. Several structure arrays were drawn using LDPE and 9108 and 9508 elastomers. Examples of these arrays with various spacings are shown in Figure 6.5.

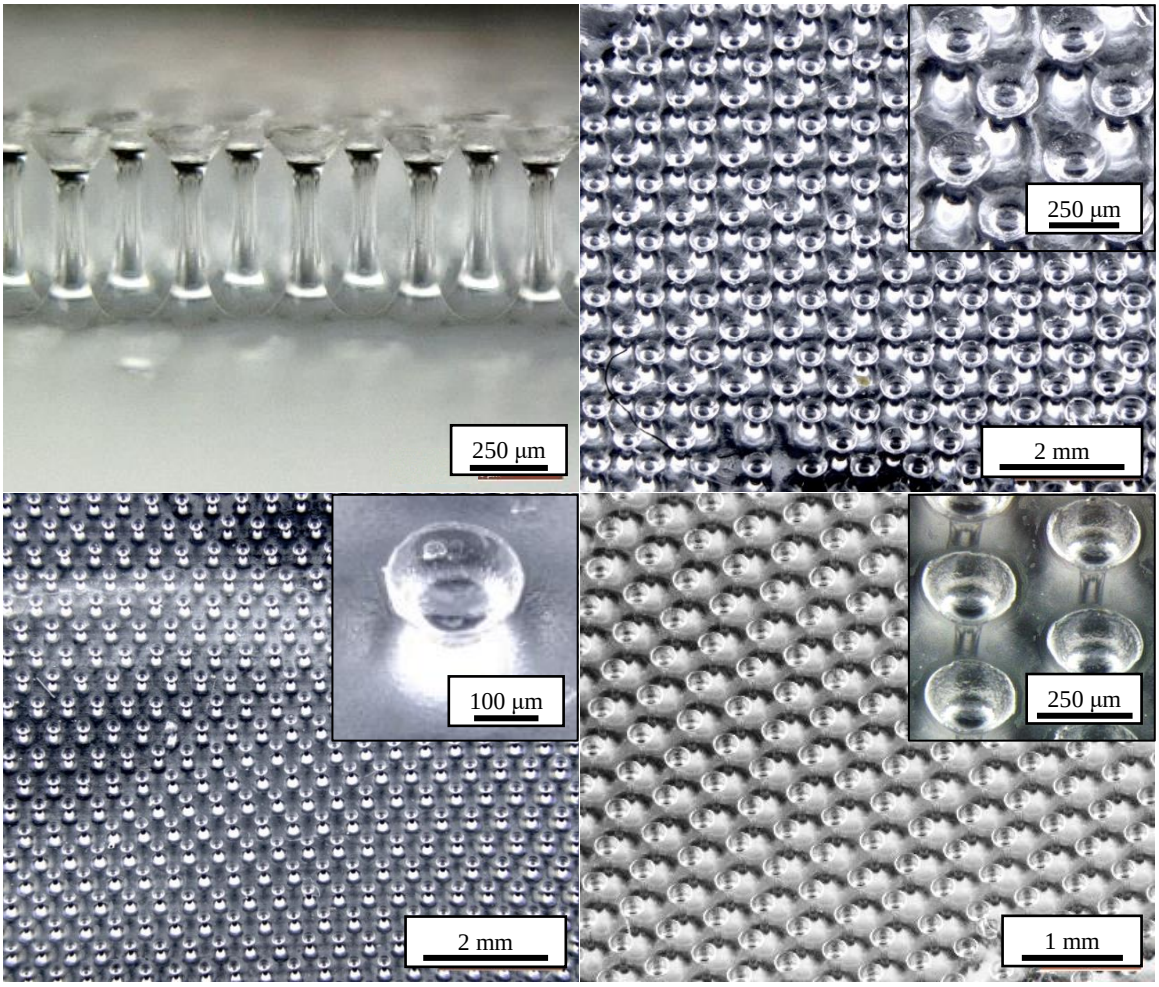

Figure 6.5. LDPE (top left), 9108 (top right), and 9508 (bottom) micro-suction cup arrays drawn with 250-µm diameter patterns

Finally, micro-suction cup arrays were drawn using the 100-µm diameter rounded micropillar patterns in both LDPE and the 9508 elastomer. As discussed, the difficulty in both aligning the pattern to the melt surface and achieving a precise dip depth without over- or under-dipping increases significantly with each reduction in the feature size of the

pattern and desired structures. The rounded caps of the 250-µm diameter micropillars were approximately 75 µm in height, while the caps of the 100-µm diameter micropillars were less than 30 µm in height. This reduction in cap height, along with the increased difficulty in visualizing the pattern's interaction with the melt from the side view of the microscope, made large-area, uniform structure arrays much more difficult to produce at this feature size. However, a number of uniform structure arrays were obtained with the 100-µm diameter patterns, and examples of structures drawn using the 9508 elastomer are shown in Figure 6.6.

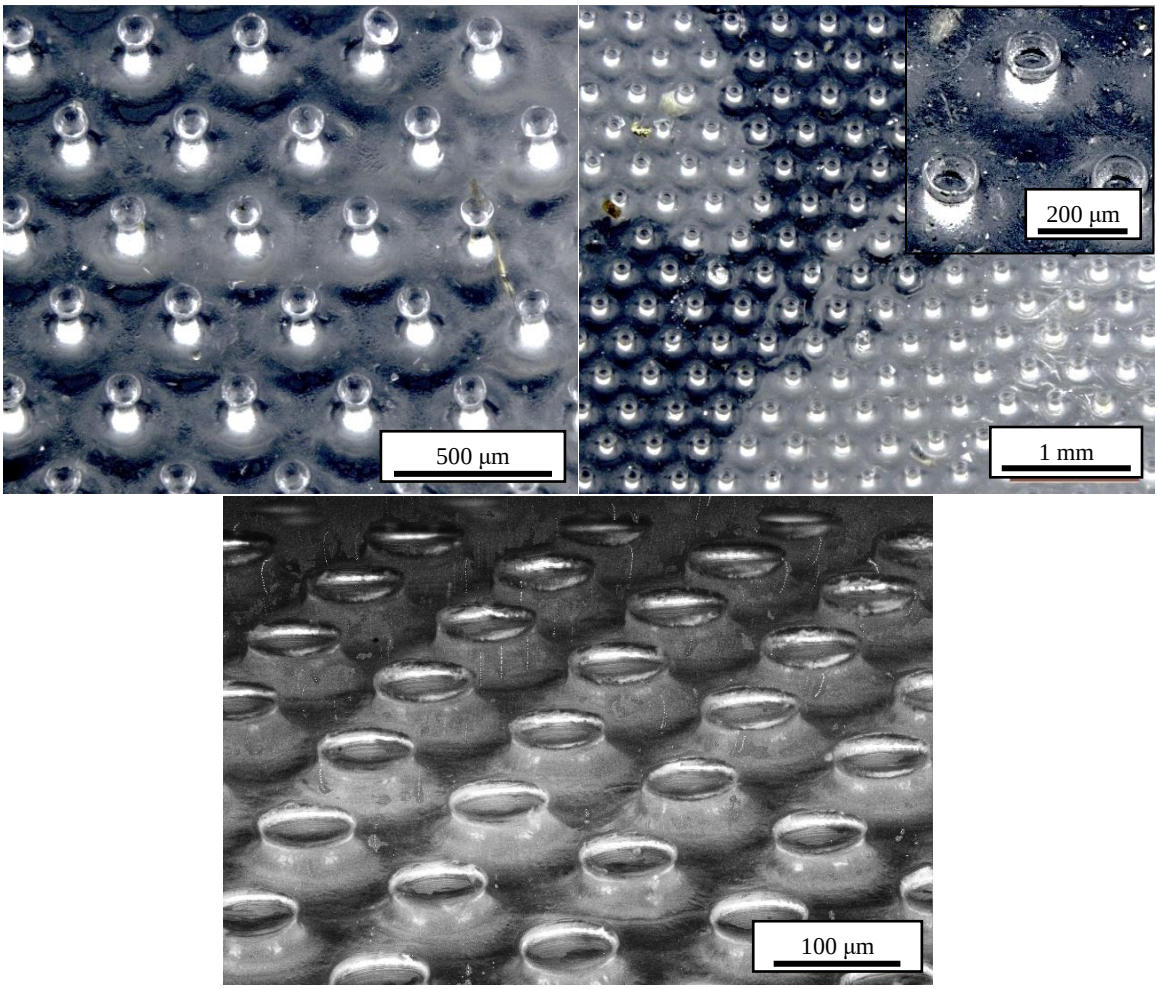

Figure 6.6. 9508 micro-suction cup arrays drawn with 100-µm diameter patterns

While under-dipping often leads to either a sharp, needle-like structure or no structure at all being drawn, over-dipping results in goblet-like structures with high side walls, as the pattern extended too far into the melt and allowed the melt to wet and adhere to the sides of the micropillars during drawing. These structures, shown in Figure 6.7, are undesirable from the perspective of the micro-suction cup arrays' potential application as a dry adhesive. Tall sidewalls restrict the cups' ability to spread out on a surface and form a negative pressure cavity with a tight seal at the edges, as the sidewalls can buckle or curl when pressed onto a surface.

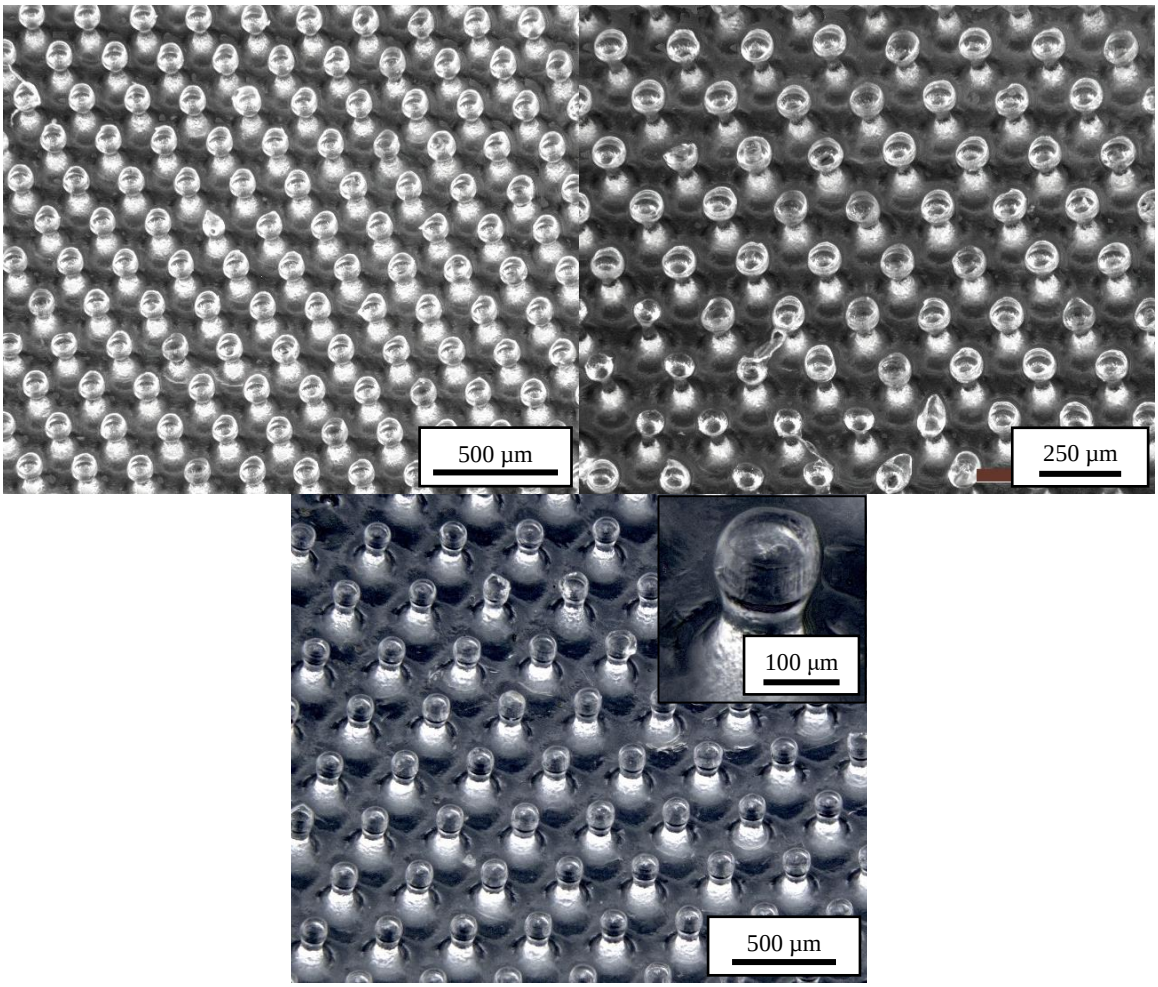

Figure 6.7. 9508 over-dipped micro-suction cup arrays drawn with 100-µm diameter patterns

Although micro-suction cup arrays were drawn successfully with the 100-µm diameter patterns, drawing with the 50-µm diameter rounded micropillars arrays has, as of yet, been unsuccessful. One hundred microns may serve as an approximate and practical lower limit for the diameter of pattern and subsequent structure array that can be produced over a meaningful area with the current drawcasting method and configuration. More uniform and smaller diameter structures can certainly be drawn with the current system in very small numbers, as there is less room for error when using a small upper pattern with few features, but sample arrays of very small size are not thought to be of practical use. An alteration to the upper patterns and drawcasting method that may facilitate drawing of smaller structures and larger areas is currently under investigation and will be further discussed in the following chapter.

6.2. Parametric Samples

Arrayed micro-suction cup samples were prepared using 9108, 9508, and LDPE films with variety of process parameters. In each set of samples, one parameter was varied while all others were held constant. The 500-µm diameter BGA patterns were used in each experiment, as these larger patterns afforded better visualization during dipping, and the leveling process was generally simpler when using larger patterns. Films for these experiments were pressed to a thickness of 650 µm. An approximate dip depth of 150 µm was used in each experiment; however, it could not be guaranteed that this dip depth was consistent between samples. The position of the pattern relative to the film surface during drawcasting was observed optically, which did not afford the necessary level of precision to ensure an exact dip depth. For this reason, a quantitative comparison of measurements

of the structure arrays' structural features such as measurements of the cup and stem diameters with respect to a varying process parameter would have been insubstantial, as the contact area between the polymer melt and pattern as it is being drawn up directly affects the shape and size of the resulting cup. In this study, the effect of changing the process parameters on the overall success or failure of a drawcasting experiments was primarily considered.

The process parameters investigated in this study included the dip temperature, draw speed, draw temperature, draw height, and dwell time. In a number of experiments, the draw temperature was lower than the dip temperature, which meant the pattern was lowered into the melt at the dip temperature, and the heaters were turned off and cooling fans were turned on. The pattern dwelled in the melt until the system reached the desired draw temperature. As a result, the dwell time was also non-constant, and the dwell or cooling times were recorded. The data obtained from these experiments serves to both complement and append the extensional measurements on the rheometer discussed in Chapter 5. The temperature was held constant during extensional measurements on the rheometer, while drawcasting experiments facilitated investigation into the effects of cooling during the process.

In the following data sets, the sample nomenclature is as follows: "polymer-experiment series-sample number." The 9108 elastomer is referred to in the data sets as "1," 9508 is referred to as "5," and LDPE is referred to as "E." The processing conditions used to produce samples using the 9108 elastomer are listed in Table 6.1. The rows shaded in green correspond to conditions that resulted in a successful sample array, while those shaded in red represent failed drawing attempts.

Table 6.1. 9108 Parametric Samples

Sample	Dip Temperature (°C)	Draw Speed (µm/s)	Draw Temperature (°C)	Draw Height (µm)	Dwell Time (s)
Dip Temperature					
1T1	160	1000	160	500	0
1T2	170				12
1T3	180	1000	160	500	23
1T4	190				32
Draw Speed					
1S1	190	10	160	500	32
1S2		50			
1S3		100			
1S4		500			
1S5		1000			
1S6		5000			
1S7		10000			
1S8		15000			
1S9		20000			
Draw Temperature					
1D1	190	1000	100	500	112
1D2			110		100
1D3			120		81
1D4			130		69
1D5			140		47
1D6			150		45
1D7			160		32
1D8			170		25
1D9			180		18
1D10			190		0
Dwell Time					
1I1	180	1000	180	500	10
1I2					20
1I3					30
1I4					40
1I5	180	1000	180	500	50
Draw Height					
1H1	190	1000	160	250	32
1H2				500	
1H3				750	
1H4	190	1000	160	1000	32

Samples drawn from 9108 films with a dip temperature of 160 and 170 °C, draw temperature of 160 °C (1T1 and 1T2), and speed of 1000 μm/s were unsuccessful, while the higher dip temperatures tested with the same draw temperature and speed were found to successfully draw patterns. In extensional measurements on the rheometer, samples could not be drawn at a speed of 1000 μm/s below a temperature of 190 °C, but samples were drawn successfully on the drawcasting testbed at draw temperatures as low as 100 °C (1D1). These seemingly contrasting results are a consequence of the varying dwell times and dip temperatures between experiments. In the experiments on the rheometer, the dip and draw temperatures were always equal, and the dwell time was held constant throughout the experiments at 10 seconds. The success of samples 1T3 through 1D10 in Table 6.1 and the discrepancy between their complementary rheometer experiments can all be attributed to the higher degree of contact area established with the drawcasting samples. This larger contact area was established both due to higher dip temperatures relative to the draw temperatures and, in most cases, a longer dwell time, as was shown in the results of the wetting experiments described in Chapter 5.

The failed samples in the dip temperature and dwell time sets of experiments ("T" and "I" series, respectively) were all adhesive failures, or Type I failures as identified in Chapter 4. In these experiments the contact between the melt and the pattern was insufficient to deform the bulk material. This contact can clearly be encouraged by either raising the dip temperature, as proved by the transition between samples 1T2 and 1T3 in which the dip temperature was raised from 170 to 180 °C, or increasing the dwell time, as shown in comparison of samples 1I4 and 1I5 in which the dwell time was increased from 40 to 50 seconds. This behavior again reflects the results of the wetting experiments in

Chapter 5 in that a sufficient degree of contact between a probe and polymer melt at given temperatures can be reached by either increasing the dwell time or raising the temperature at which the two make contact.

Sample 1H4, which was produced with a 190 °C dip temperature, 160 °C draw temperature, speed of 1000 μm/s, and dwell time of approximately 30 seconds was the only sample that exhibited a cohesive or necking failure, defined as a Type III failure in Chapter 4. In the extensional experiments, attempts to draw 9108 at 160 °C at 1000 μm/s with a 10-second dwell led to an adhesive failure. Raising the temperature to 190 °C and increasing the dwell time allowed a sufficient contact area to form between the melt and pattern to deform the melt. However, the extension of the filament to 1000 μm at 1000 μm/s led to a necking failure. As samples were successfully drawn at similar conditions with a lower draw height (experiments 1H1-3), it is apparent that the increased degree of stretching allowed the melt to relax and neck to the point of failure. Increased draw heights and higher-AR structures could be attained with higher draw speeds and/or cooling rates, as the cohesive strength of the polymer melts was found in Chapter 5 to increase with an increased velocity or a decreased temperature (see Figures 5.13-5.14 for reference). As discussed in Chapter 5, a higher draw speed promotes a more elastic response from the melt and suppresses the excessive viscous flow that leads to necking failures. There is undoubtedly a limit to which increasing the draw speed facilitates the drawing of successful samples, as some viscous response of the material is clearly necessary for deformation to be possible. Increasing the cooling rate has a similar effect to increasing the draw speed, as lowering the temperature effectively increases the strength of the melt by encouraging an elastic response from the polymer melt.

A similar set of experiments was then performed with 9508 elastomer films. The processing conditions used in this study are presented in Table 6.2, with successful samples once again shaded in green and failed samples shaded in red.

Table 6.2. 9508 Parametric Samples

Sample	Dip Temperature (°C)	Draw Speed (µm/s)	Draw Temperature (°C)	Draw Height (µm)	Dwell Time (s)
Dip Temperature					
5T1	160	1000	160	500	0
5T2	170				13
5T3	180	1000	160	500	25
5T4	190				42
Draw Speed					
5S1	190	10	160	500	27
5S2		50			
5S3		100			
5S4		500			
5S5		1000			
5S6		5000			
5S7		10000			
5S8		15000			
5S9		20000			
Draw Temperature					
5D1	190	1000	100	500	124
5D2			110		109
5D3	190	1000	120	500	83
5D4			130		69
5D5			140		55
5D6			150		48
5D7			160		27
5D8			170		17
5D9			180		11
5D10			190		0
Dwell Time					
5I1	160	1000	160	500	10
5I2	160	1000	160	500	20
5I3					30
5I4					40
5I5					50
Draw Height					
5H1	190	1000	160	250	27
5H2				500	
5H3				750	
5H4				1000	

As was seen in experiments with the 9108 elastomer, the tests with very similar dip and draw temperatures failed to draw structures from the melt. The draw temperatures in experiments 5T1 and 5T2 were both 160 °C, while the dip temperatures were 160 and 170 °C, respectively. In the elongational experiments performed on the rheometer, the 9508 elastomer was successfully drawn at 160 °C and 1000 μm/s, the same speed used in 5T1-4. Samples 5T1 and 5T2 exhibited a Type I adhesive failure, meaning the pattern was unable to withdraw any polymer melt from the film. As the remaining samples in this series with higher dip temperatures and subsequently longer dwell times were drawn successfully, the viscosity of the polymer at the draw temperature (160 °C) is not the cause of the failure for the first two samples. Therefore, the failure of these samples must be attributed to a lack of contact established between the pattern and polymer melt. As previously discussed, this contact area can be increased by raising the dip temperature (as seen in samples 5T3-4) or increasing the dwell time.

The draw conditions used for sample 5T2 (160 °C, 1000 μm/s, 12 s dwell) were nearly identical to a successful rheometer experiment (160 °C, 1000 μm/s, 10 s dwell). The adhesive failure in the case of sample 5T2 due to insufficient contact area is most likely a result of the inhomogeneity of the drawcasting system with respect to the conditions in the rheometer. The temperature distribution in the rheometer is more uniform than that in the drawcasting system. As a result, the acceptable ranges for drawing samples using the drawcasting system as compared to the rheometer are slightly more restrictive. These same distinctions can be used to explain the failure of sample 5I1.

Finally, samples 5D1 and 5D2 also exhibited Type I adhesive failure. This behavior can be attributed to the high viscosity and predominantly elastic response of the polymer

at the low drawing temperatures of 100 and 110 °C. As the extensional experiments on 9508 discussed in Chapter 5 show a trend of failing at lower velocities as the temperature is decreased, and the experiment performed at 130 °C and 5000 μm/s exhibited a Type I adhesive failure, it follows that this same failure was be seen in the material at lower speeds and lower temperatures.

Finally, micro-suction cup arrays were drawn from LDPE films. The process conditions used in these experiments are listed in Table 6.3, with the successful samples shaded in green and failed samples shaded in red.

Table 6.3. LDPE Parametric Samples

Sample	Dip Temperature (°C)	Draw Speed (µm/s)	Draw Temperature (°C)	Draw Height (µm)	Dwell Time (s)
Dip Temperature					
ET1	130	1000	130	500	0
ET2	140	1000	130	500	15
ET3	150				28
ET4	160				40
ET5	170				53
ET6	180				76
ET7	190				100
Draw Speed					
ES1	160	10	130	500	40
ES2		50			
ES3		100			
ES4		500			
ES5		1000			
ES6		5000			
ES7		10000			
ES8		15000			
ES9		20000			
Draw Temperature					
ED1	190	1000	100	500	127
ED2			110		102
ED3			120		97
ED4			130		100
ED5			140		75
ED6			150		61
ED7			160		44
ED8			170		24
ED9			180		12
ED10	190	1000	190	500	0
Dwell Time					
EI1	160	1000	160	500	10
EI2					20
EI3					30
EI4					40
EI5					50
Draw Height					
EH1	160	1000	130	250	40
EH2				500	
EH3				750	
EH4				1000	

Attempts to draw structures with similar dip and dwell temperatures and little to no dwell time failed with the LDPE films as they did with 9108 and 9508 films, as seen by the adhesive (Type I) failures exhibited by samples ET1 and ED10. The dip and draw temperatures used in these samples (130 and 190 °C, respectively) were successfully used to elongate filaments in the extensional rheological tests, however. Once again, these results are due to the difference in dwell times. In the extensional measurements on the rheometer, samples were successfully elongated at 130 and 190 °C with a speed of 1000 μm/s and a 10-second dwell time. When these same conditions were employed in the drawcasting process with no dwell time, samples were unable to be drawn, as the polymer was not given time to form the necessary contact area with the pattern to deform the melt. As indicated by the wetting results as well as the successful elongation at similar conditions in Chapter 5 and by the success of the samples drawn in the "I" series of experiments, increasing the dwell time at a given temperature increases the contact area and, consequently, reduces the chance of an adhesive failure during drawing.

Additionally, samples were unable to be elongated on the rheometer at 130 °C at velocities 5000 μm/s and higher, while samples were successfully produced using the drawcasting system at dip and draw temperatures of 160 and 130 °C, respectively, and velocities ranging from 5000-20000 μm/s (ES6-9). As has been observed and discussed with previous LDPE samples as well as elastomer samples, the higher temperature of the melt and pattern when they first make contact, along with the increased dwell time, allows for a larger contact area between the melt and the pattern and facilitates drawing.

As previously stated, the dip depth between experiments was not constant. Therefore, quantitative comparisons between the structural features of cups prepared with

different conditions could not be reasonably made. The cup diameter and structure height are likely the structural features to be most directly influenced by the dip depth, meaning a small change in the dip depth between two otherwise identical experiments would have a more noticeable effect on the cup diameter than on the minimum stem diameter, for example. As the mid-filament diameter and necking behavior of the polymer melt is highly dependent on the polymer's viscoelastic behavior, the stem size and shape are more directly affected by the draw temperature, speed, and height. Images taken of the structures resulting from the fifth set of experiments with each type of polymer film are shown in Figure 6.8 to illustrate the effect of increased draw height on the stem diameter.

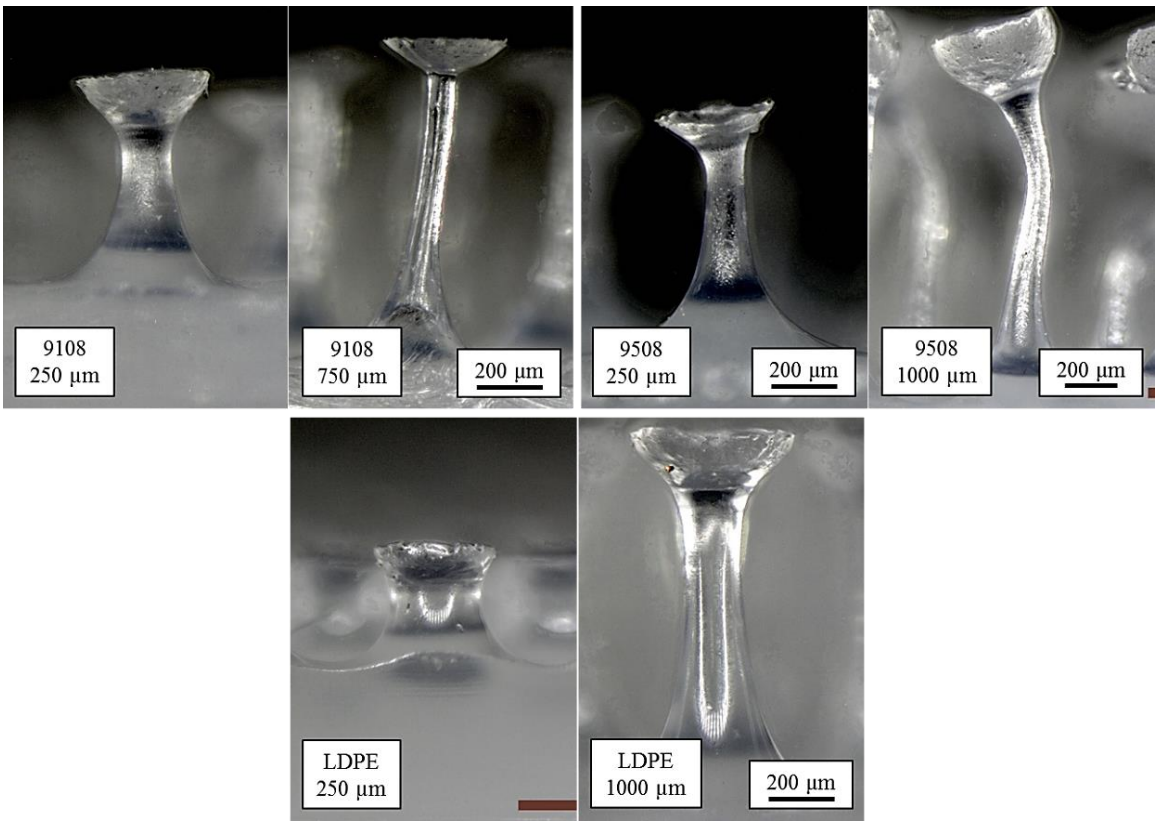

Figure 6.8. 9108, 9508, and LDPE micro-suction cups drawn to varying heights

6.3. Alternative Methods, Materials, and Patterns

A number of elements and capabilities of the drawcasting system were not fully investigated in this work. The upper and lower heater of the drawcasting system can be programmed independently, and a temperature gradient could be imposed on the material. A differing pattern and base temperature were used with 500-μm diameter patterns to draw LDPE structures, which are shown in Figure 6.9.

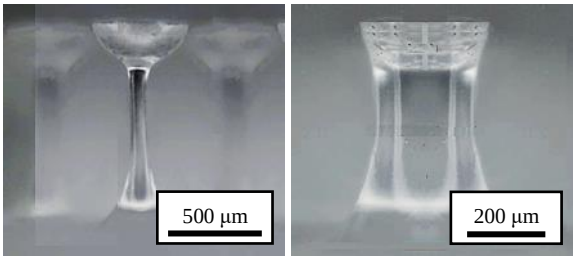

Figure 6.9. LDPE structures drawn with different temperature conditions

The structure in the first image of Figure 6.9 was drawn with both heaters at 150 °C, while the second structure was drawn with a base temperature of 160 °C and pattern temperature of 100 °C. Imposing a temperature gradient clearly had a notable effect on the structures' stem profiles.

The drawcasting system can also be used with an array of other polymers than those employed in this work. Suction cup arrays have been produced in other thermoplastics such as high-density polyethylene (HDPE) and polystyrene (PS), and in immiscible polymer blends in order to create composite structures with different thermal and mechanical properties. Structures have also been drawn using thermally curable PDMS resin by

gradually heating the system during drawing. PDMS suction cups are depicted in Figure 6.10.

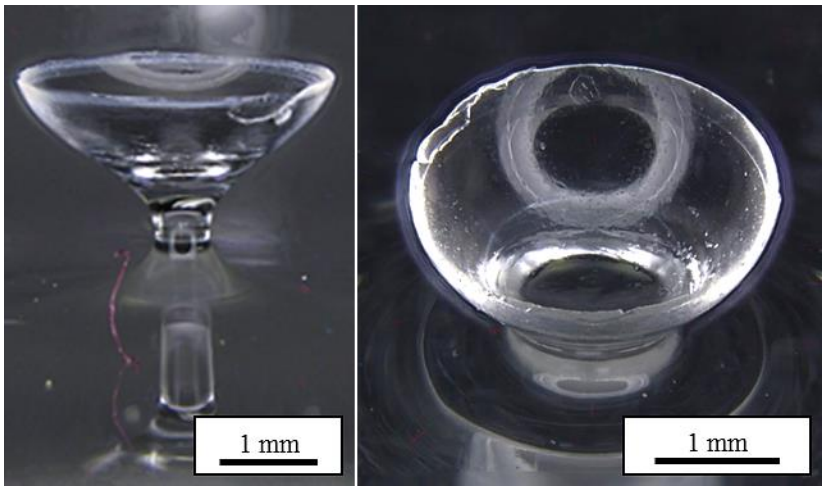

Figure 6.10. PDMS suction cups

The structures produced during drawcasting can be altered in a number of ways other than altering the material or process conditions listed above. As an example, a sample was drawn with the heated base positioned on an x-y translation stage, which was shifted during drawing in order to create structures with curved stems, as shown in Figure 6.11.

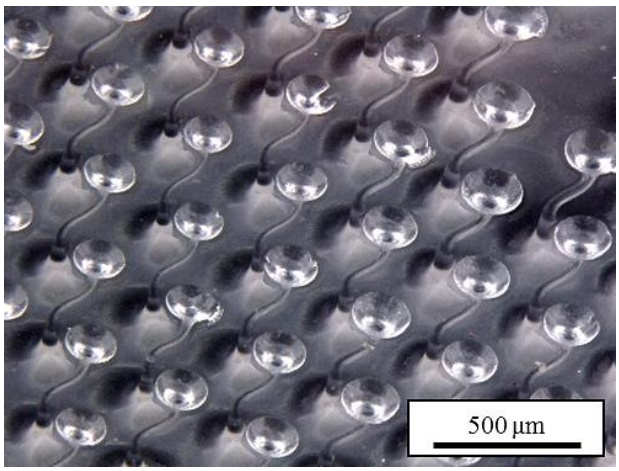

Figure 6.11. Micro-suction cup array with curved stems

Curved or tilted structure arrays such as those in Figure 6.11 could be used to create surfaces with anisotropic properties, such as the directional adhesion displayed by the angled mushroom structure arrays discussed in Chapter 2. Conventional microneedle arrays have also been fabricated using the drawcasting system with upper hemispherical patterns using both LDPE and 9508 films. These structures, shown in Figure 6.12, were drawn in a stepwise manner, in which the pattern was drawn upward in increments with a constant cooling rate until the material necked completely.

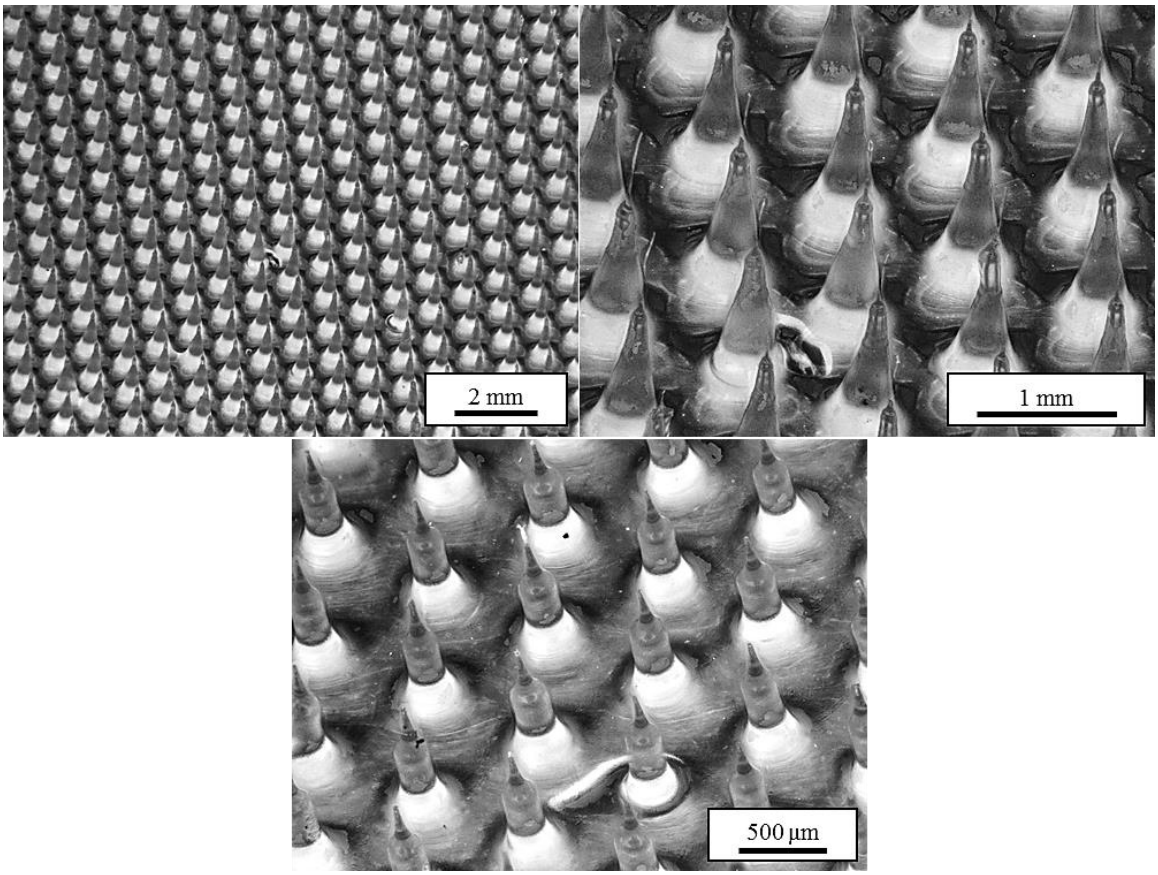

Figure 6.12. LDPE (top) and 9508 (bottom) microneedles

Microneedles were also drawn using polystyrene. In these structures, the pattern was raised at a constant rate to a programmed height while cooling, forming very thin, high-AR structures. Once the system cooled below the polymer's T_g, the pattern was raised upward very quickly, causing the necks to fracture at their thinnest points, resulting in the sharp-tipped structures shown in Figure 6.13.

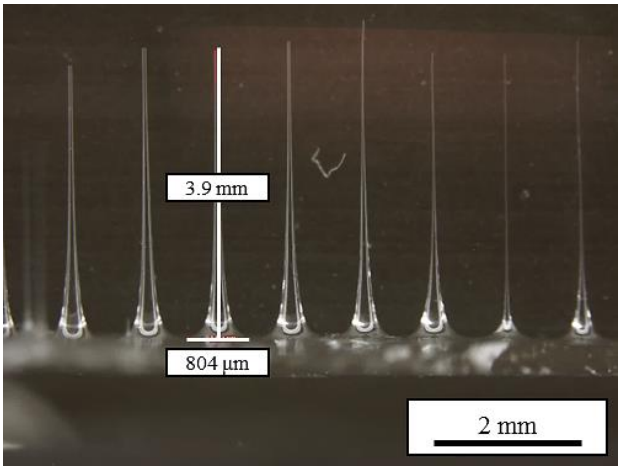

Figure 6.13. Polystyrene microneedles

Finally, the upper pattern used in drawcasting could ostensibly be any shape or size that one could fabricate, which could be used for a wide variety of applications. For example, an asymmetric teardrop-shaped pattern could be used to draw structures with anisotropic properties such as directional adhesion. Different materials and pattern shapes could be used to create surfaces for applications in areas such as microfluidics, self-cleaning, oleophobicity or –philicity, anti-reflection, controlled emissivity, and surface waveguides, among others.

CHAPTER 7. CONCLUSIONS AND RECOMMENDATIONS

7.1. Conclusions

In this thesis, the development and characterization of the drawcasting process with thermoplastic polymers has been discussed. The drawcasting process is the first of its kind that can be used to produce arrays of high-AR polymer surface structures with unique geometries and tip architectures. The current methods most frequently used to make such structures, including photo- and soft lithography as well as drawing lithography, are not suitable for fabricating such diverse structure arrays over large areas.

New molding and lithographic techniques were developed to fabricate the upper hemispherical patterns used for drawcasting in sizes ranging from 3 mm to 50 μm in diameter, and the process was used to successfully produce arrays of polymer structures from 3 mm to 100 μm in diameter. While there is a significant amount of literature concerning viscous drawing techniques for producing microneedle arrays, only one instance was found of drawing polymer resins or melts with a tip shape other than a sharp point. High-AR pillars were drawn by Paek and Kim with microspheres at their tips [114,173]. These pillars were unable to be drawn in an array larger than 5x5, and the group reported the difficulty in achieving parallelism between the drawing pattern and polymer resin as the main hindrance to drawing larger areas. Although parallelism is less critical when drawing microneedles, it remains an issue in any viscous drawing process. The F-TIR technique developed in this work allowed us to draw structure arrays on a much larger scale than any reported in literature. The smallest patterns successfully used in this work

to draw structures were the 100 μm rounded micropillar arrays. These micropillars were arranged hexagonally on a 27x27 mm substrate with an inter-pillar spacing between 100 and 200 μm, resulting in an upper drawcasting pattern containing thousands of structures. The maximum linear dimensions of the patterns used in this work were restricted by the size of the pattern heater and components, but a larger upper heater base in conjunction with the F-TIR leveling technique would certainly facilitate drawing structure arrays over an even larger area.

The work in this thesis was motivated to scale the process up to larger areas and a continuous production system. In this work, we not only developed a new process and multiple new patterning techniques, but also identified and characterized material properties and process parameters that influence the structures obtained from drawcasting. In order to apply the process to a different material, one would need an understanding of that material's thermal, wetting, and rheological behavior. The drawcasting process is highly rate- and temperature-dependent, and the geometry of the structures obtained have been observed to vary widely with process parameters such as dip or draw temperature, dwell time, draw speed, and draw height. We used STA to determine the glass transition, melting, and degradation temperatures of three polymer samples in order to identify a working temperature range for drawcasting with each polymer. Shear and extensional rheological testing was conducted in order to quantify the viscoelastic response of the polymers as functions of temperature and deformation rate. Shear rheological testing is particularly useful for determining a sample's relaxation time and zero-shear viscosity, while the extension studies proved to be good indicators as to whether a given set of parameters such as temperature, dwell time, and drawing velocity would yield a successful

drawcasting sample. Discrepancies between the results of the extensional experiments in Chapter 5 and those of the parametric studies in Chapter 6 can largely be understood with knowledge of the dependence of the contact area on time and temperature. Furthermore, the thermophysical, wetting, and rheological data, along with knowledge of the pattern geometry, is essential for development of a thermofluid model. While such modeling is out of the scope of this thesis, some initial modeling work performed by collaborators will be discussed later in this chapter and is presented in the Appendix.

7.2. Recommendations

7.2.1. Process Control

One parameter that was not studied in this work and needs further investigation is the effect of cooling on the process and obtained structures. In the current drawcasting system, regulation of the cooling rate is not possible. However, the time at which cooling begins (i.e., when the pattern is in the melt or after the pattern has been drawn up) has been shown to greatly affect the final structures, as cooling the melt begins to raise its viscosity and slows the rate of necking while the material is still molten. The ability to precisely control the cooling rate using a device such as a Peltier heat pump would grant further control over the drawcasting process and obtained structure arrays.

Additionally, the ability to closely monitor the evolution of the structures during drawing with respect to temperature, time, and draw height would be critical in order to develop an accurate predictive model of the drawcasting process. Quantifying the rate of necking at various heights along a polymeric filament during drawing along with the

volume of polymer being displaced from the molten reservoir would undoubtedly aid in process modeling. Furthermore, correlating the necking rates to process parameters such as temperatures, draw speeds, dip depth, dwell time, etc., could allow one to predict not only whether a given set of parameters would successfully draw an array, but also the geometry of those structures.

Throughout this work, the parallelism between the pattern and the surface of the polymer film as well as precise knowledge of the gap between the two were consistently found to be the most difficult parameters to control, as well as some of the most critical. Development of accompanying fixture such as the PDMS molding fixture, polymer film press, and the F-TIR system tremendously enhanced our abilities to produce films and patterns with parallel surface and to orient them with respect to one another. It is not yet known what the lower resolution limit of the current F-TIR system is and, accordingly, for how small of a pattern it will be effective. For example, a pattern with elements with a 10 μm diameter may be too small to resolve on the F-TIR system to the degree necessary to align such a pattern to the polymer film. In such a scenario, a camera with a higher resolution or better lighting within the system itself could extend the useful range of F-TIR. Currently, the dip depth cannot be controlled to the level of precision necessary for drawcasting with very small diameter patterns (<100 μm) and precise quantitative measurements such as the wetting experiments in Chapter 5. Excellent control of the dip depth would also allow one to see more clearly the effect of changing process parameters on the resulting structure geometry in parametric experiments like those presented in Chapter 6. There are a number of schemes through which one might monitor this gap more closely, such as using distance sensors or more precise cameras and optimized lighting

schemes. These costly methods were out of the scope of the current work, but improvements to the dip depth precision are crucial in order to use the drawcasting system to produce arrays of sub-100-µm diameter structures or to scale the process up to pattern large areas.

7.2.2. Adhesion Testing and Modeling

As discussed previously, the micro-suction cup arrays produced in this work were developed for use as dry skin adhesives. The 500-µm diameter structure arrays have been proven to pick up clean glass slides, as shown in Figure 7.1.

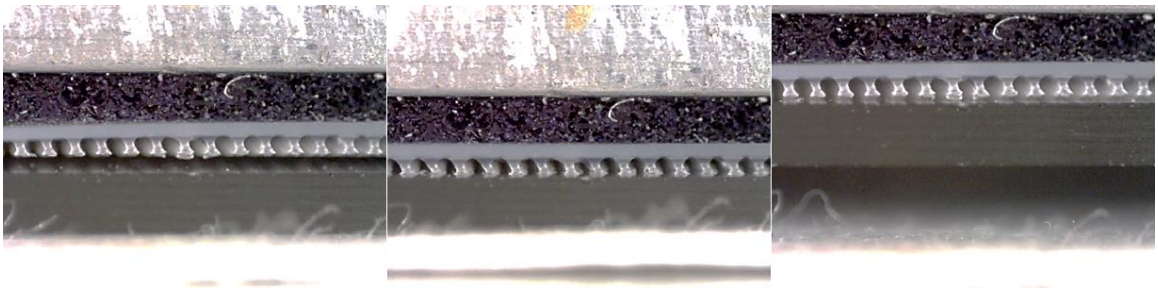

Figure 7.1. Glass pickup by 500-µm diameter micro-suction cup array

The adhesive strength of these cups, however, has not been quantified. The topography of human skin from a variety of areas and subjects has been analyzed by collaborators in order to ascertain the ideal scale of structures that could make adequate contact to form a suction seal. Human skin has varying degrees of roughness, with lines or furrows ranging from 20-200 µm in depth. These lines divide the surface of the skin into polygonal cells, the size of which is dependent on the area of the body being examined as well as other factors such as age and gender [174]. Numerical modeling of the contact and subsequent deformation of the

cups with human skin was also performed by collaborators. The average degree of rotation a cup of a given size would need in order to make the best possible contact with the skin surface was calculated at various points. The deviation of a rotated cup from the actual skin topography was then calculated to estimate the actual contact of the cup rim and the amount of deformation a given cup would need to make complete contact. Images related to the modeling as well as selected results are included in the Appendix. Based on the results of this work, micro-suction cup arrays with cup radii ranging from 30 to 100 μm are believed to be the best suited for dry skin adhesives. Cups in that size range had, on average, a minimal gap between the skin and the cup rim. Preliminary adhesion testing has been performed by collaborators using samples of 100-μm diameter cup arrays on silicone substrates. Tests were performed on both flat silicone samples and silicone samples molded with skin replicas to give similar topographical and mechanical properties to human skin. Some adhesion was demonstrated between the cup arrays and silicone skin replicas. Selected data from these initial tests is shown in the Appendix. The adhesive performance of the micro-suction cup arrays has not yet been shown to rival that of similarly sized flat mushroom arrays. This could be due to non-uniformity in the cup arrays arising from imprecise leveling. Additionally, the geometry of the structure has yet to be optimized. In order for the cups to spread out on the surface of an adherend and form a suction seal with a negative pressure cavity, the stem of the cup must be sufficiently stiff such that the cup can spread without the stem buckling. Fabricating more uniform samples with a more optimized geometry for further adhesive testing is currently one of the focuses of this project.

7.2.3. Electroforming and Modeling

In order to perform more testing and fabricate arrays of structures with even smaller diameters in a reliable manner, we are considering an alteration to the drawcasting upper patterns and overall method with regard to the temperature regimes used and the process by which the upper patterns are fabricated. Producing structures reliably over a larger area becomes significantly more difficult as the structures are scaled down, predominantly because of poor visualization of the pattern/polymer surface, which often causes one to over- or under-shoot when trying to make contact with the surface. Extending the rounded micropillar patterns too deep into the melt results in the goblet-like structures shown in Chapter 6. In order to avoid over-dipping and curtail the reliance of the process on visual methods and estimation, we are attempting to induce local melting at the contact points between the pattern and polymer film. If the polymer film is below its melting temperature and a pattern at a much higher temperature is brought into contact with it, an ensuing temperature gradient within the polymer film will result in a finite molten volume around the contact points between the pattern and film surface. Additionally, the F-TIR method could potentially be used to determine the proximity of the pattern to the film and the dip depth before local melting occurs, rather than relying on the side view given by the optical microscope. This theory was validated using a 500-μm diameter pattern at 190 °C and a 9508 film at 100 °C. The pattern was left in contact with the film for 30 seconds before being raised 500 μm and cooled to room temperature. The resulting cup array is shown in Figure 7.2.

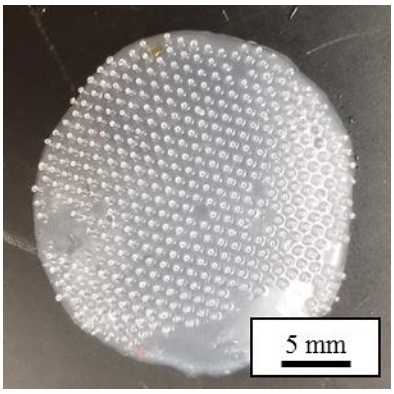

Figure 7.2. 500-µm diameter micro-suction cup array drawn using local melting

A great deal of thermal modeling has been performed by collaborators to predict the melt volume of a given polymer film as a function of film thickness, film temperature, pattern temperature, and contact time. It was found that the epoxy micropillar patterns currently used would not be able to effect a necessary melt volume to draw desired structures due to the poor thermal conductivity of the epoxy and its glass substrate. A pattern comprised of a high thermal conductivity material would be needed for successful and efficient local melting and drawing. Selected results from these modeling efforts are provided in the Appendix.

Currently, we are attempting to fabricate rounded micropillar patterns with diameters of 100 µm and below by using an electroforming process, in which metal is electrodeposited onto a conductive substrate acting as a cathode in an electrolytic bath containing metallic salt compounds. Current is applied to the bath by an immersed anode, causing the metallic ions in the solution to deposit on the desired substrate [175]. To achieve electroformed patterns for drawcasting, master patterns and PDMS molds are created in the same methods described in Chapter 3. The PDMS molds are cleaned thoroughly in hexane and acetone and subsequently sputtered with a 50-nm thick layer of gold (UniFilm

Multisource Sputtering System). After sputtering, a cross-section of a PDMS sample was examined in an SEM to confirm the coverage of gold in the holes of the mold, which is shown in Figure 7.3.

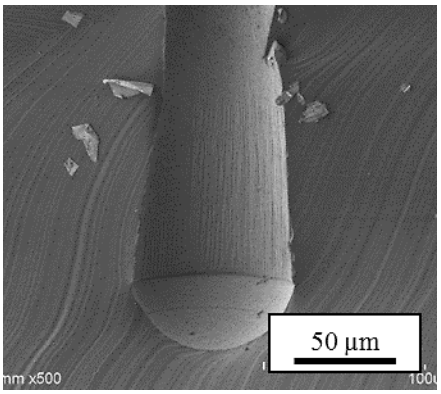

Figure 7.3. Cross-section of Au-sputtered PDMS mold

The stability of the middle portion of the sample in Figure 7.3 under the electron beam relative to the exposed PDMS indicates the gold successfully coated the holes in the negative mold. The sputtered PDMS samples were fixed to aluminum substrates with a conductive RTV silicone (Silicone Solutions SS-27S), and the electroforming was performed by B&E Electroforming Co. A small area of the first electroformed sample is shown in Figure 7.4.

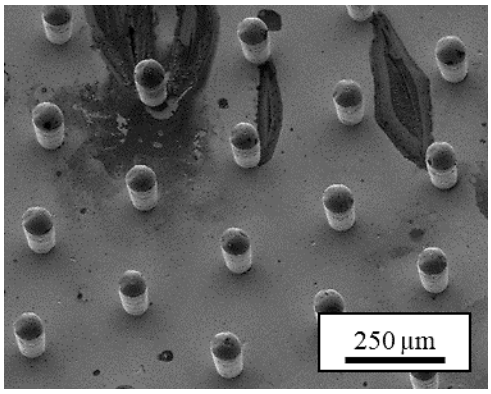

Figure 7.4. Electroformed rounded micropillar array

While the area shown in Figure 7.4 is mostly uniform, the majority of the sample was unusable, consisting of hollow pillars or pillars without caps. Such pillars are depicted in Figure 7.5.

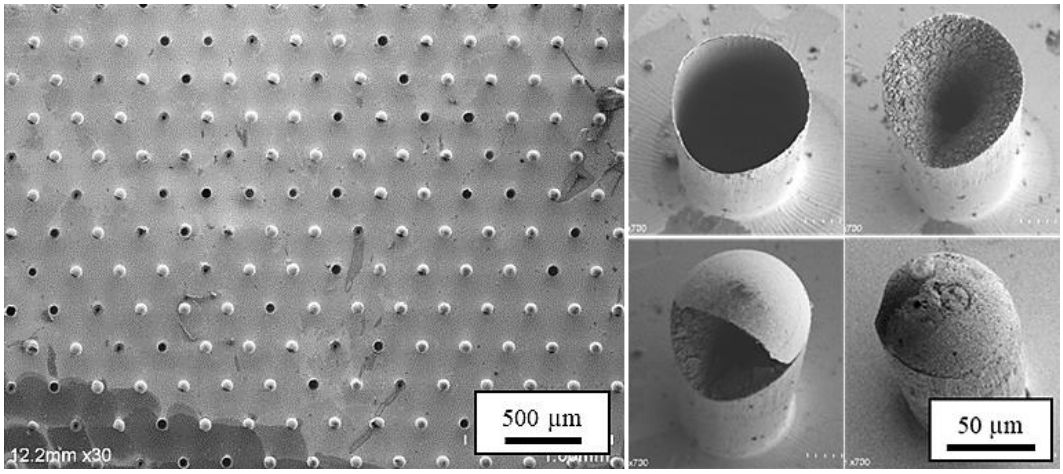

Figure 7.5. Electroforming defects

The defects seen in Figure 7.5 are most likely due to surface contamination or insufficient sputtering. The cleaning and sputtering processes are currently being investigated and refined to ensure more uniform patterns are produced during electroforming. If the electroforming process proves to be a viable method to produce metal

replicas of the rounded micropillars produced photolithographically, the drawcasting process could not only be extended to smaller features sizes by locally melting the polymer film, but larger patterns could also be produced more easily than by molding. Currently, the top pattern sizes are limited by the photolithographic patterning capabilities at the Georgia Tech microfabrication facility (excluding the heater and component sizes, as those can be easily sized up). The equipment in the Georgia Tech cleanroom allows for processing wafers up to four inches in diameter. Multiple electroformed patterns can be produced from a single silicon master, and they could easily be stitched together to form a larger area pattern. Additionally, the electroformed patterns would be significantly more robust than the pattern silicon wafers, which snap easily during PDMS demolding, or the epoxy patterns, which can easily detached from the glass substrate if dropped or scratched.

7.2.4. Continuous Processing

Finally, the ultimate objective in the development of the drawcasting process is for it to be implemented in a continuous manner for manufacturing. Two roll-to-roll concepts for the drawcasting process are presented in Figure 7.6.

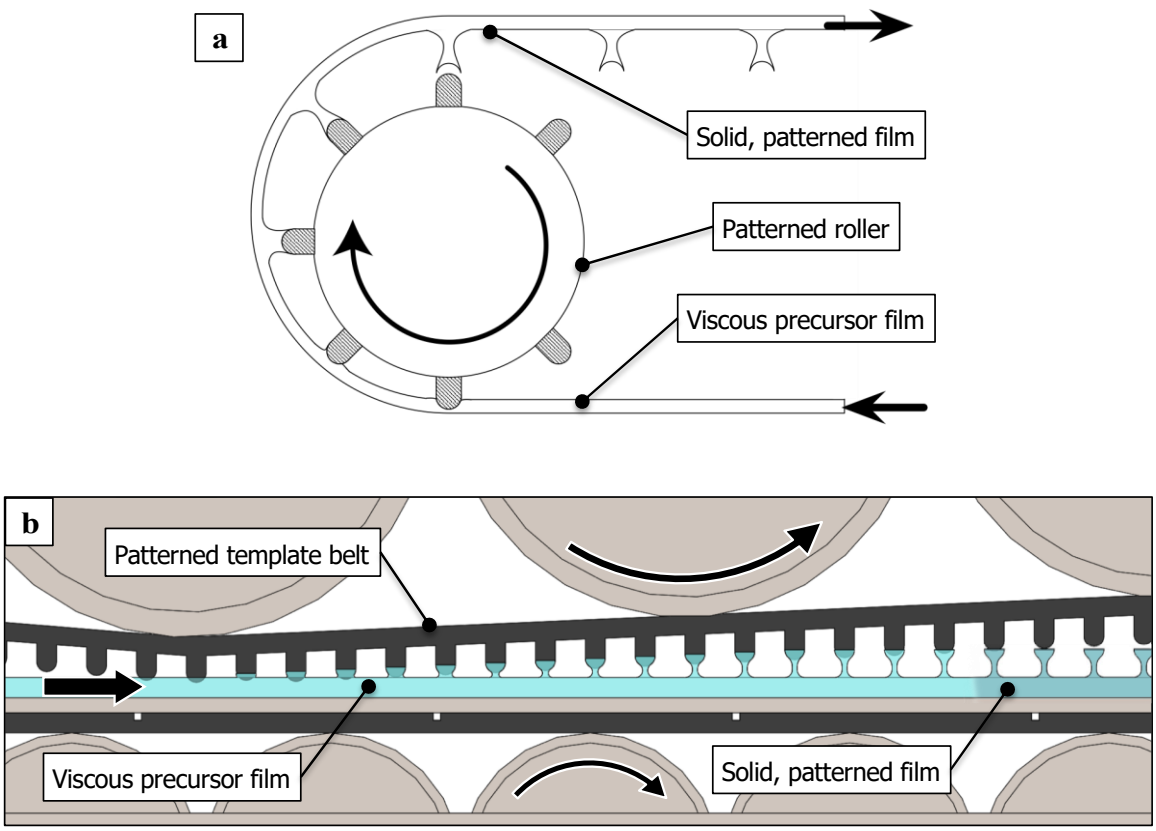

Figure 7.6. Roll-to-roll drawcasting concepts

Similar to the current drawcasting system, structures produced in these theoretical processes would rely on parameters such as speed, temperature ranges, and precise control of the pattern position relative to the film surface. Scaling up the drawcasting process to significantly larger areas or a continuous system will be heavily dependent on the aforementioned parameters as well as the ability to fabricate robust patterns over large areas. More sophisticated methods of detection of the distance between the pattern surface and polymer film would be necessary.

If one were to gain more precise control over parameters such as cooling and pattern positioning, the effects of changing all of the available processing parameters on the resulting structure geometry could be more clearly distinguished and used in conjunction

with thermofluid models, resulting in a refined, predictable, and adjustable process for fabricating structured polymer surfaces.

APPENDIX

This appendix presents additional images to supplement schematics and data given in the body of this thesis. Complete data sets are given where an exemplary plot was presented in previous chapters. Additionally, some modeling work and preliminary performance testing performed by industry collaborators is given.

Figure A.1 depicts the current drawcasting testbed that was developed throughout this work.

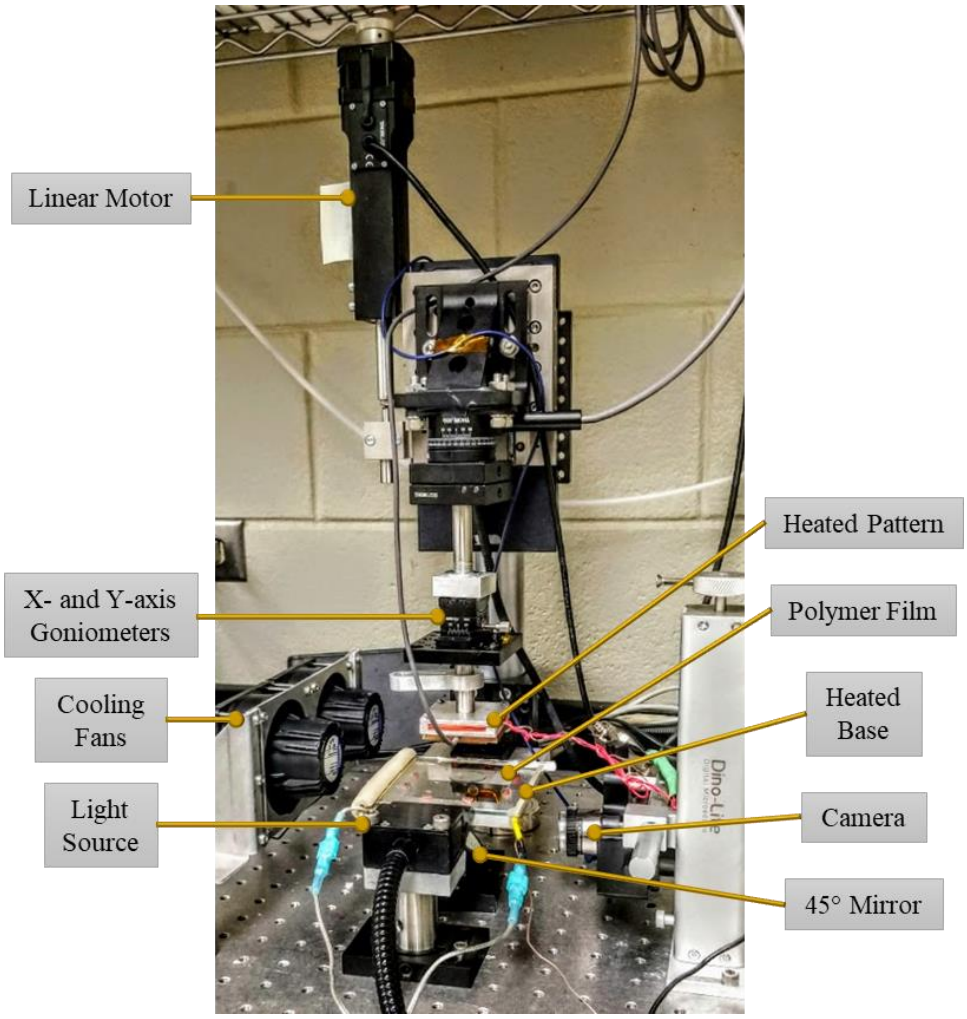

A.1. Drawcasting testbed

Figures A.2 through A.4 depict frequency sweeps performed on the 9108, 9508, and LDPE samples used in this work, respectively. The sweeps performed at 160 °C were depicted in Chapter 5, and as such, sweeps performed at 130-200 °C excluding those at 160 °C are shown in Figures A.2 through A.4.

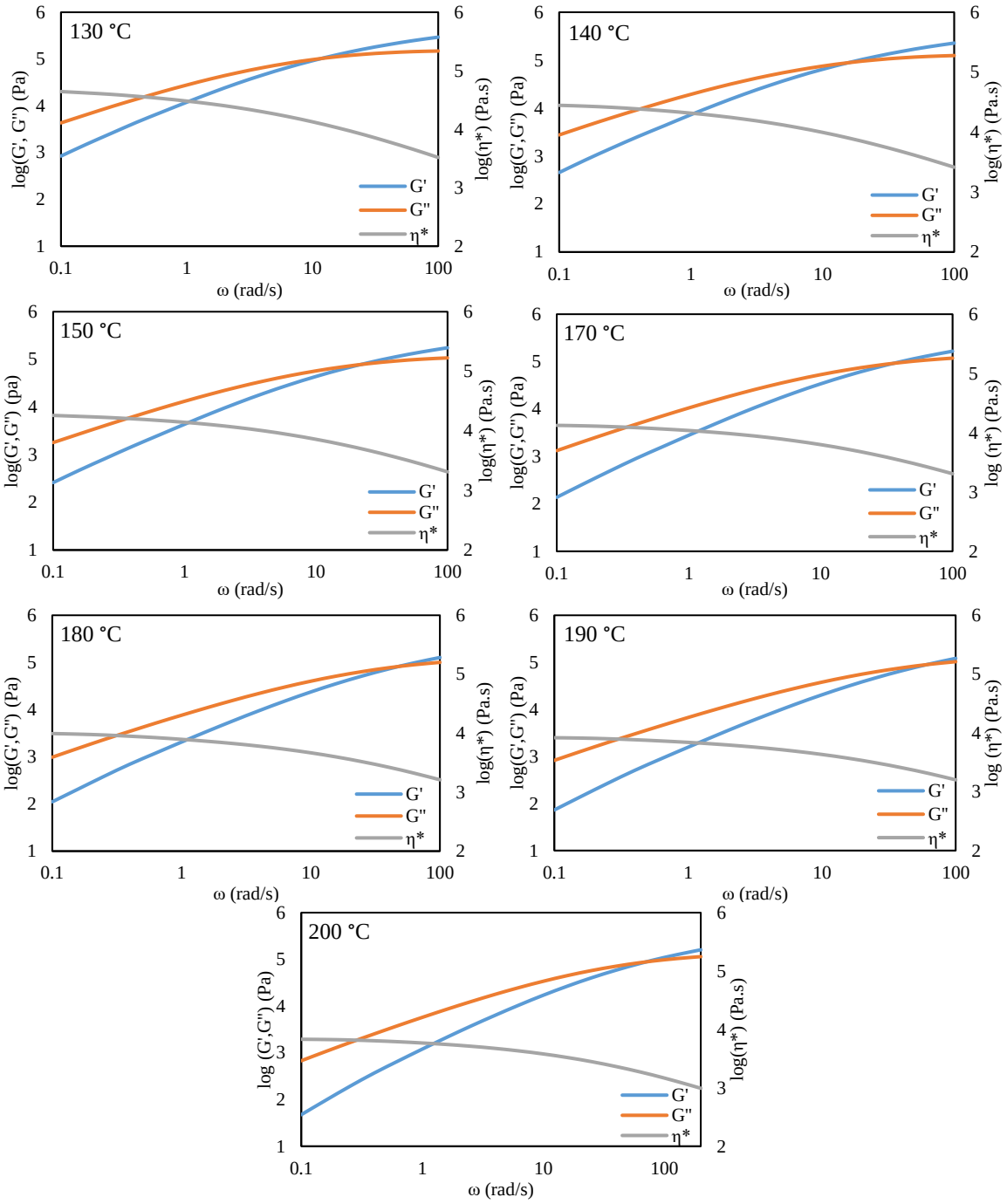

Figure A.2. Frequency sweeps at 130-200 °C on 9108

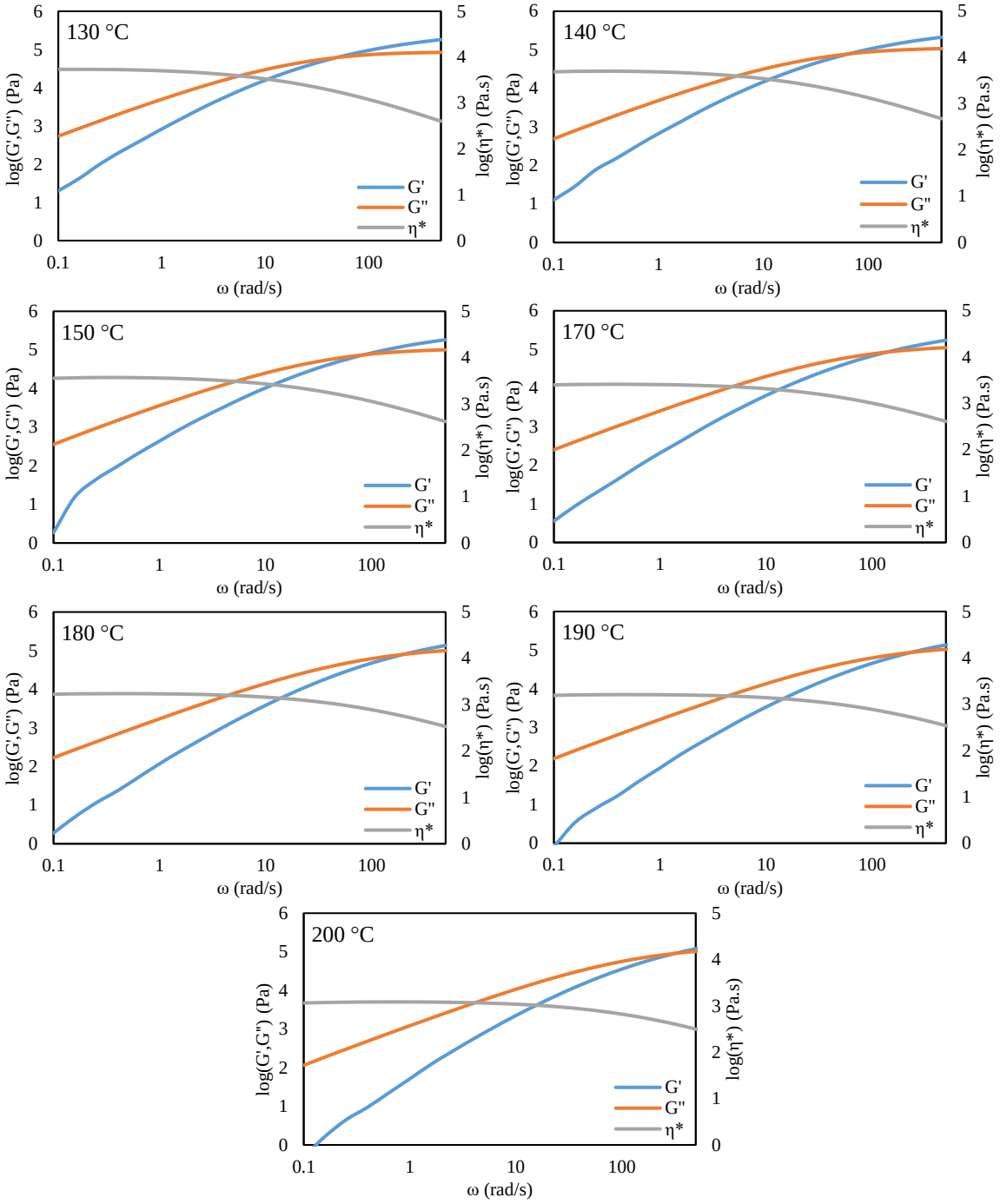

Figure A.3. Frequency sweeps at 130-200 °C on 9508

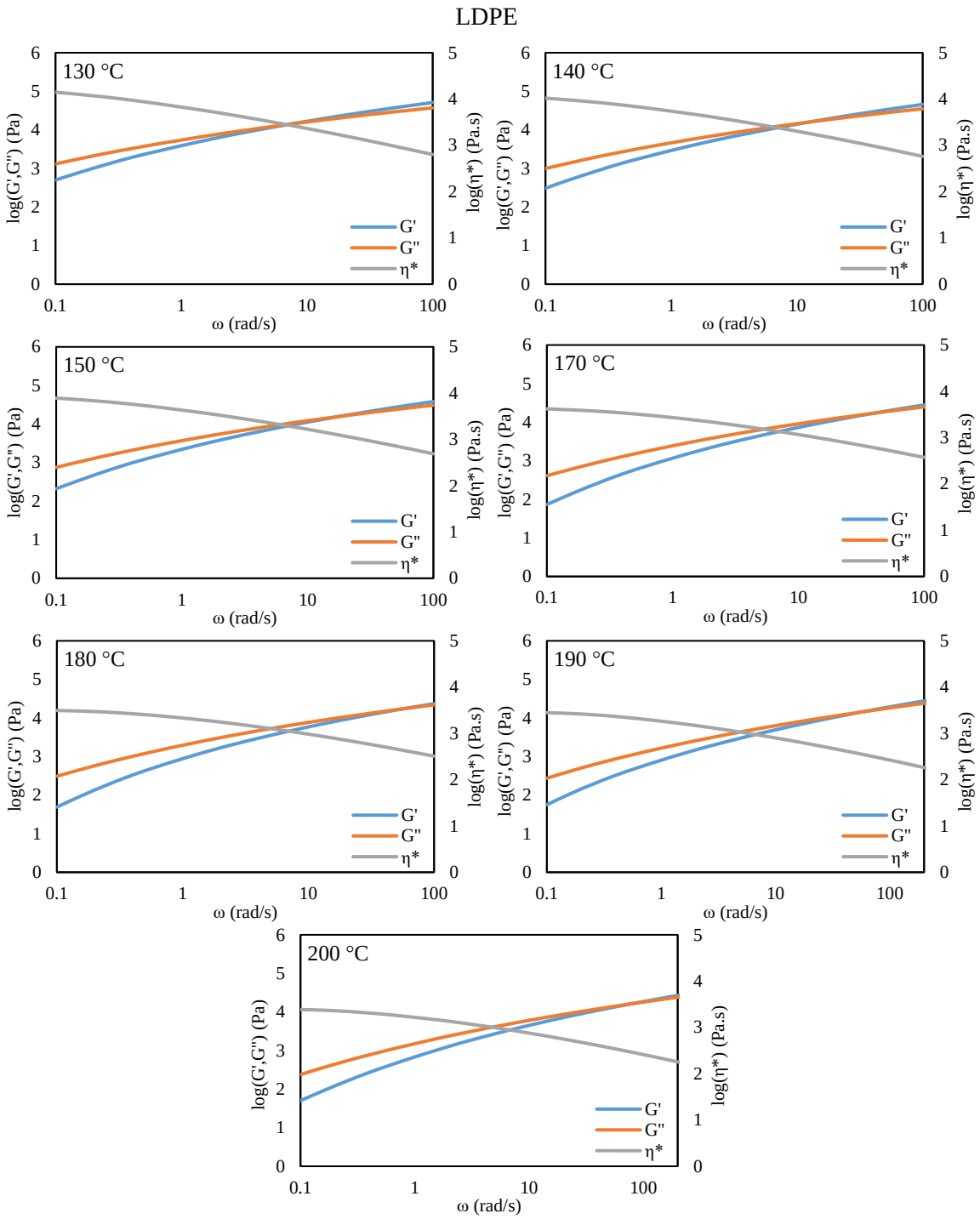

Figure A.4. Frequency sweeps 130-200 °C on LDPE

As discussed in Chapters 4 and 5, the frequency-dependent data at each temperature for each polymer investigated was transformed to shear rate-dependent plots through the

Cox-Merz relation. Figure A.5 depicts the transformed data for each polymer at temperatures from 130-200 °C, excluding the plots at 160 °C, as those plots are shown in Chapter 5.

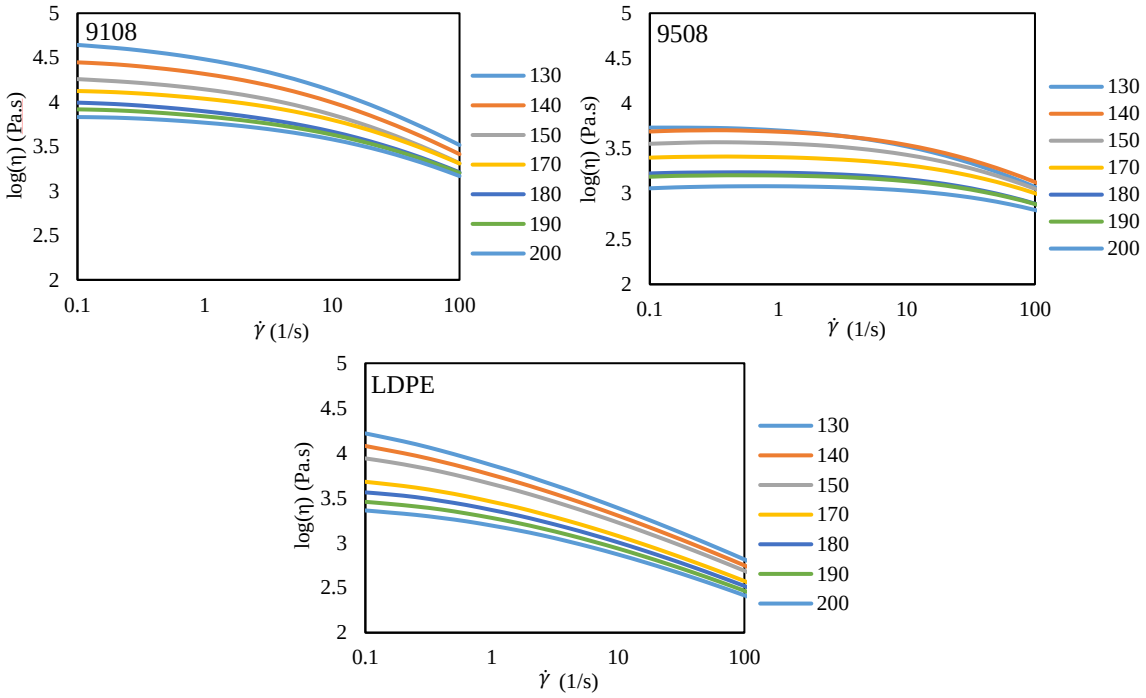

Figure A.5. Steady state viscosity versus shear rate plots at 130-200 °C for 9108, 9508, and LDPE

The force-distance plots obtained from extensional tests on each polymer at temperatures ranging from 130-200 °C are presented in Figures A.6 through A.8. As with previous data, these plots at 160 °C are given in the body of this thesis. In each plot, the force decay after reaching a maximum is plotted in the inset.

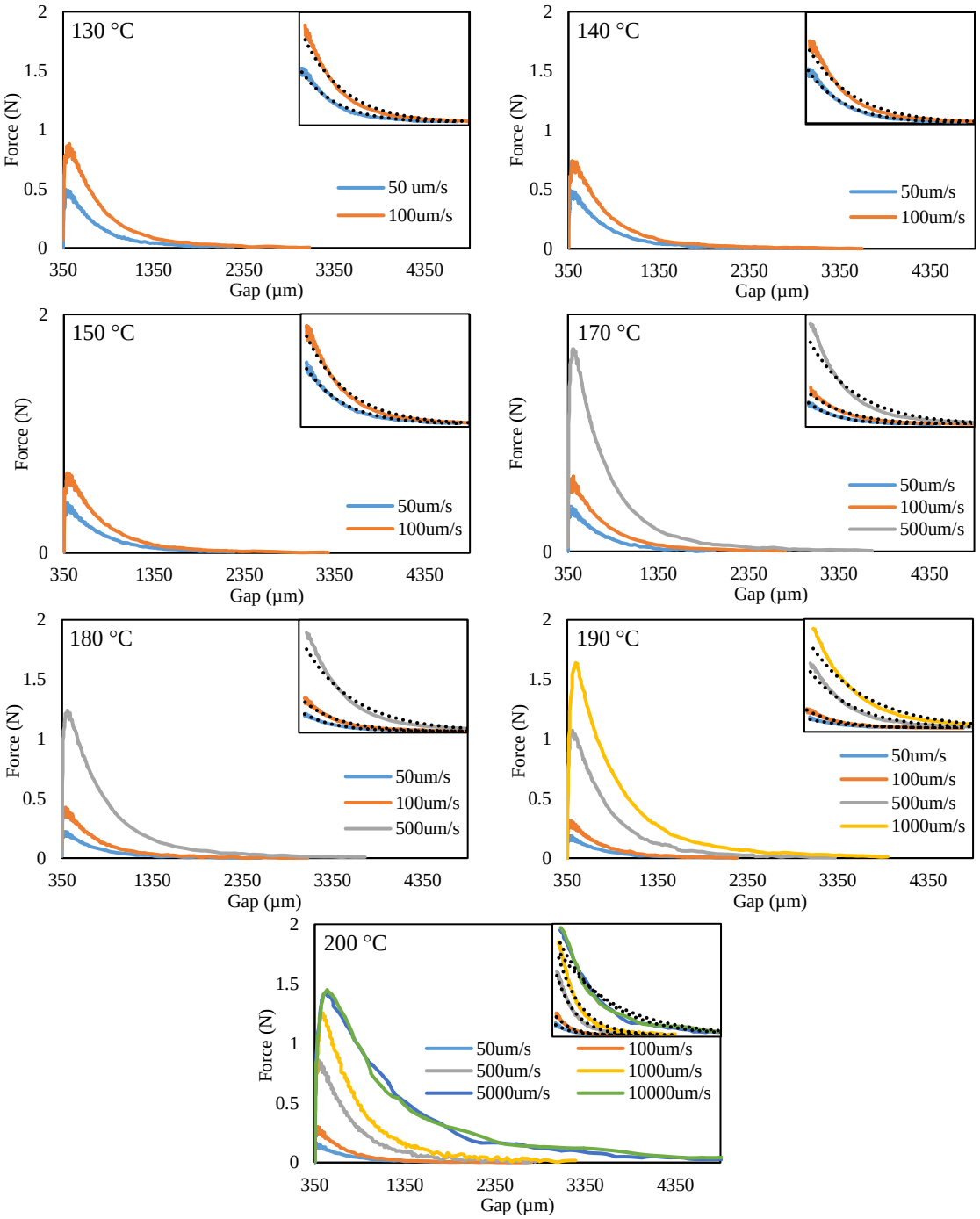

Figure A.6. Axial force versus distance plots at 130-200 °C for 9108

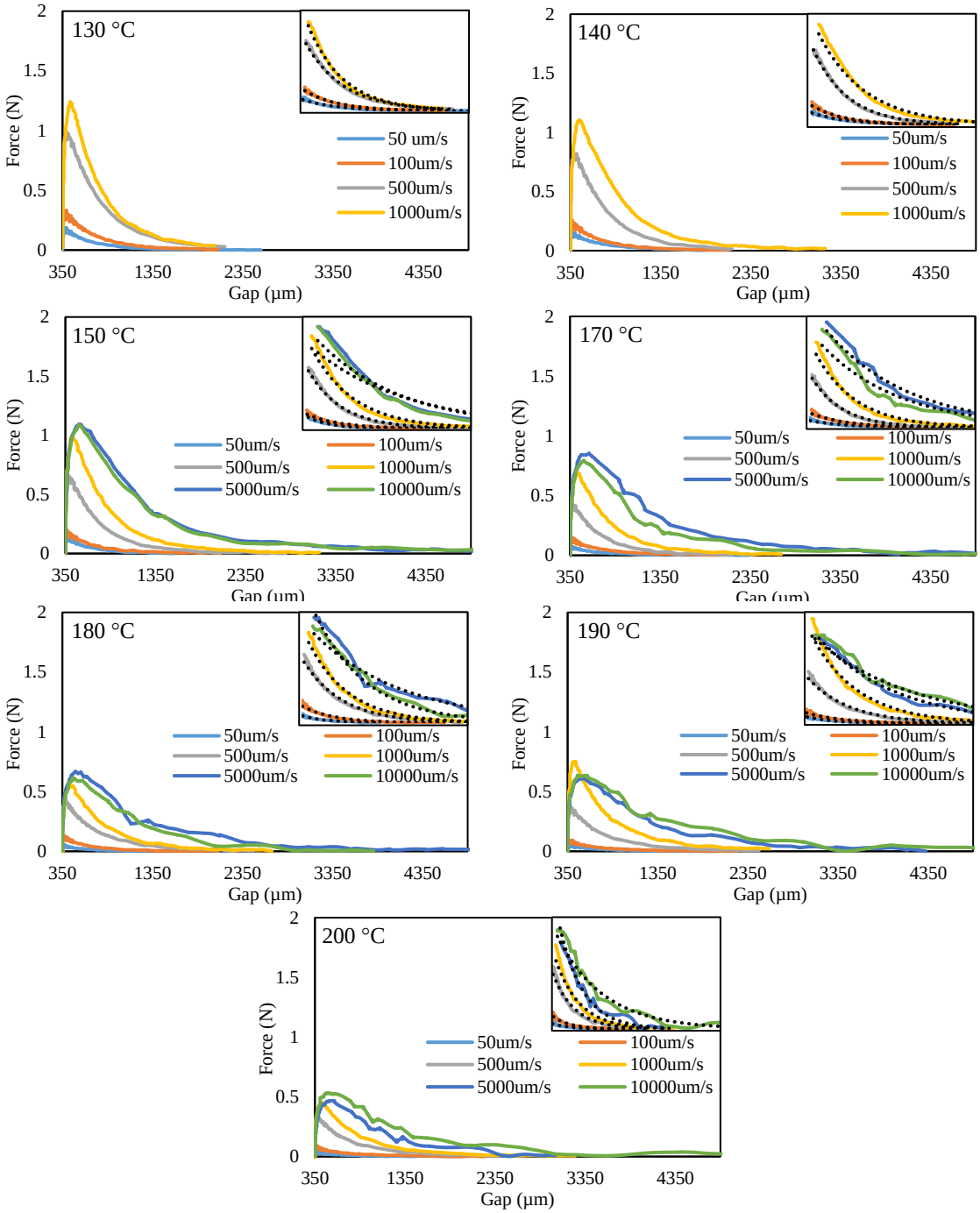

Figure A.7. Axial force versus distance plots at 130-200 °C for 9508

LDPE

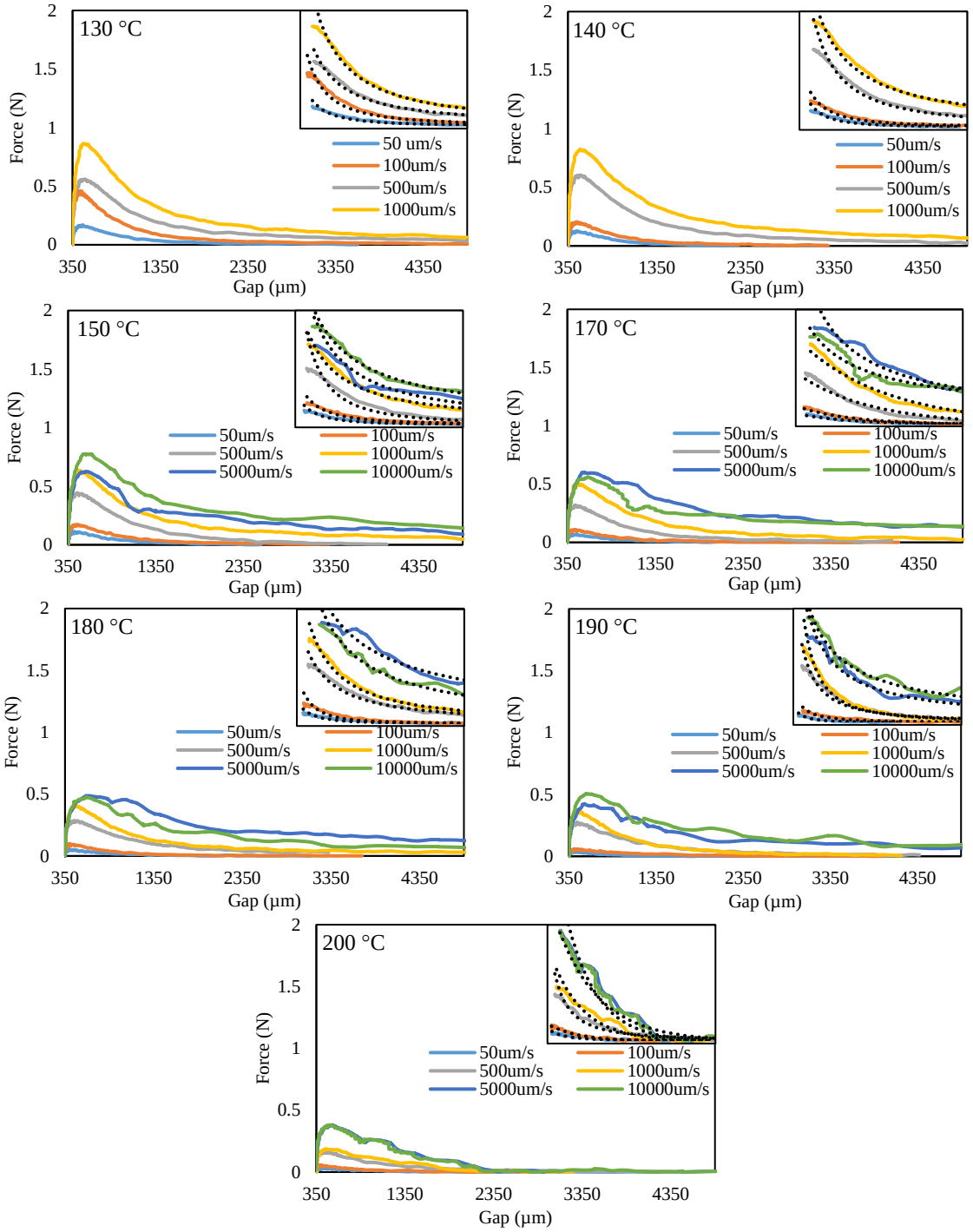

Figure A.8. Axial force versus distance plots at 130-200 °C for LDPE

Molds of human skin were prepared by collaborators using a quick-curing PVS commonly used in dental impressions on subjects of different genders, races, and ages from

different areas of the body including the hands, forearms, and backs. These molds were then scanned with a confocal microscope in order to create a digital map of the sample's topography. One such scan (excluding height data) is depicted in Figure A.9.

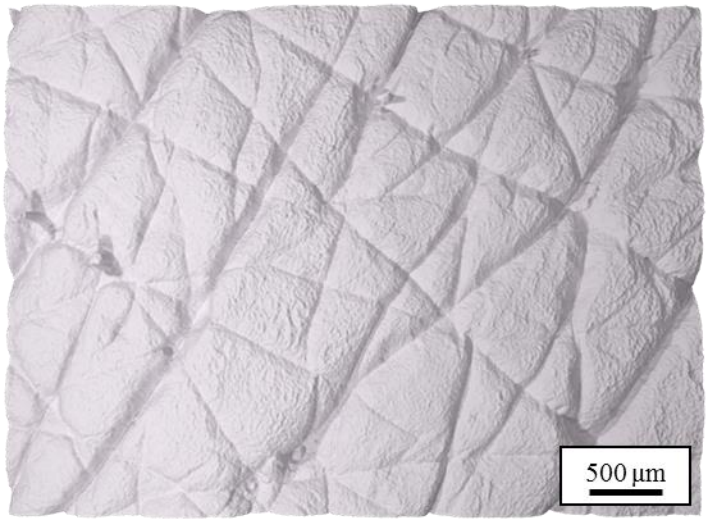

Figure A.9. Topographical scan of skin sample

Topographical models were then constructed and used to calculate the average degree of rotation needed for a cup of a given size to make complete contact with the surface. This process is depicted schematically in Figure A.10.

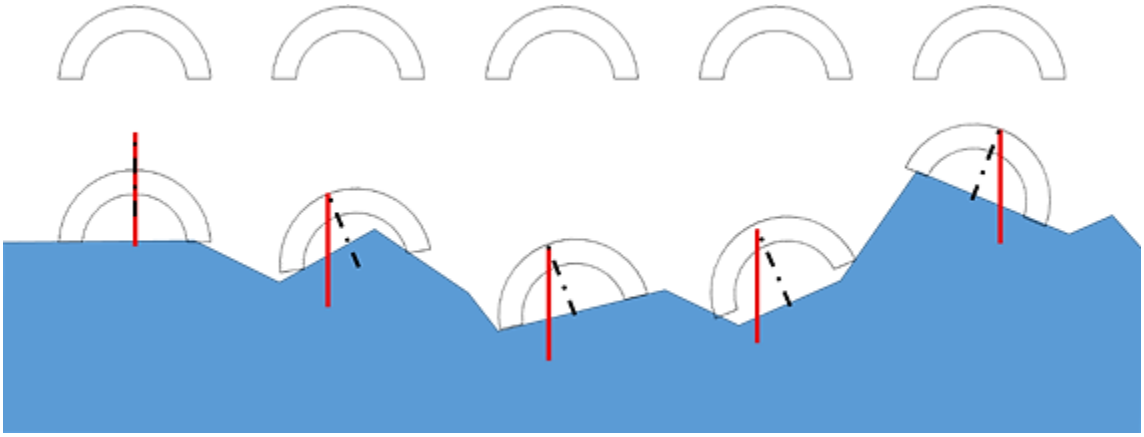

Figure A.10. Cup rotation with respect to skin topography

The average degree of rotation calculated for each cup size was then applied to a model cup and overlaid on various skin samples in order to estimate the deviation of the rotated cup from the skin topography. These results could be used not only to select an optimum cup size for a given skin type, but also to estimate the degree of compliance a cup would need to make conformal contact with the skin to create a seal. This information could guide material selections in the future. Plots of these overlays are shown in three dimensions in Figure A.11, while similar plots are shown in two dimensions in Figure A.12.

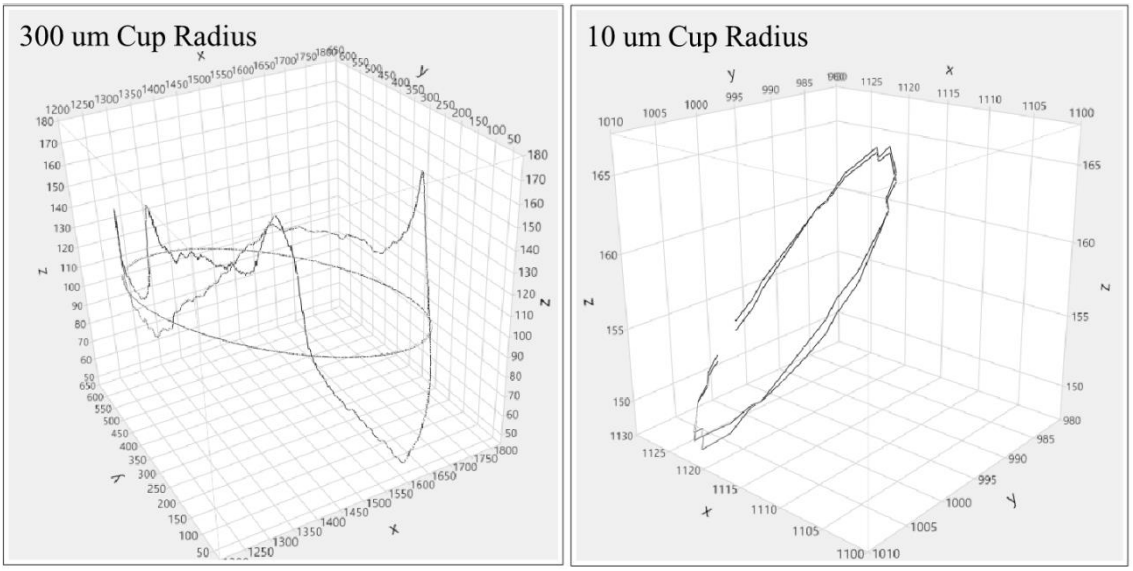

Figure A.11. 3-d overlay of rotated cup on skin topography

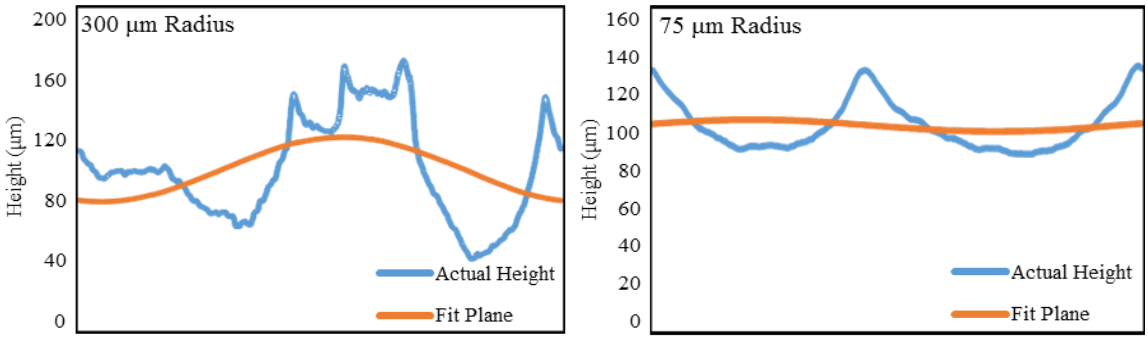

Figure A.12. 2-d overlay of rotated cup on skin topography

A number of other factors either have been or will be considered by our collaborators in the modeling and optimization efforts of the micro-suction cups as skin adhesives. These include the following:

- Pressure differential generated by a cup of a given size
- Elastic modulus of a cup with respect to its ability to spread out on a surface (rather than rotating about the stem)
- Leakage rate at the rim
- Stress relaxation of the cup leading to a loss of negative pressure
- Effect of compliance of the skin on required pre-load
- Environmental factors such as sweat or humidity
- Contamination or hair on the skin surface

Micro-suction cup arrays with 100-µm diameter structures were prepared, and a small area (500x500 µm) was used for adhesion testing on flat glass, a flat silicone substrate, and the silicone substrate molded from negative molds taken of skin. The sample was attached to a probe and lowered to make contact with the substrate and reach a specified preload (from -80 to -150 gf). The sample was then raised at a constant rate while the normal force on the probe was monitored. The contact area of the cups with the glass

substrate was also measured during testing using a similar F-TIR system to the one described in the body of this work. Initial results of a 100-µm diameter sample on glass and flat silicone are shown in Figure A.13, in which the positive peak in the force indicates adhesion between the cup array and the substrate.

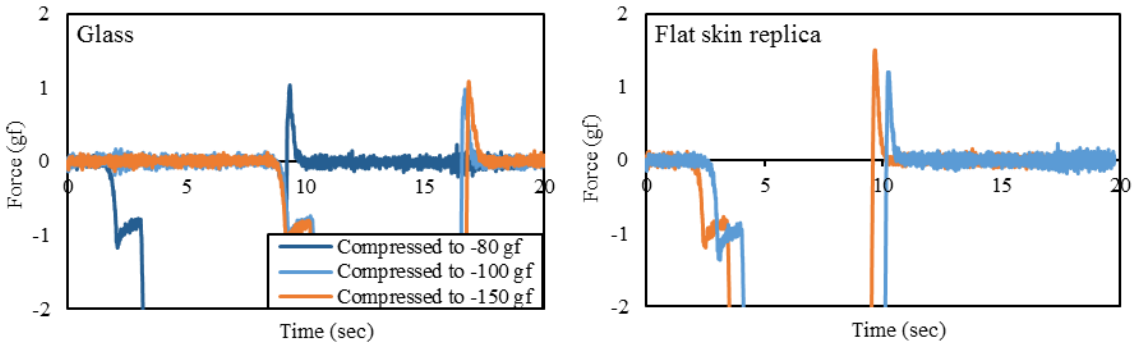

Figure A.13. Adhesion testing with 100-µm diameter sample on glass and silicone

As discussed in Chapter 7, electroforming is being investigated as a means to create upper patterns for drawcasting in order to induce local melting and draw structures from a finite molten volume. Thermal modeling was performed by collaborators first to determine if this method could be carried out using the current epoxy patterns, and second to calculate the time- and temperature-dependence of the molten volume achieved with both an epoxy and a nickel pattern that would be fabricated through electroforming. Properties of the 9508 polymer obtained in this work through thermal and rheological measurements were used in the models. Figure A.14 depicts modeling performed on epoxy and nickel pillars with a semi-infinite 9508 film in which the base of the upper pattern (the copper or glass substrate) was set at 190 °C, while the film was set at 100 °C.

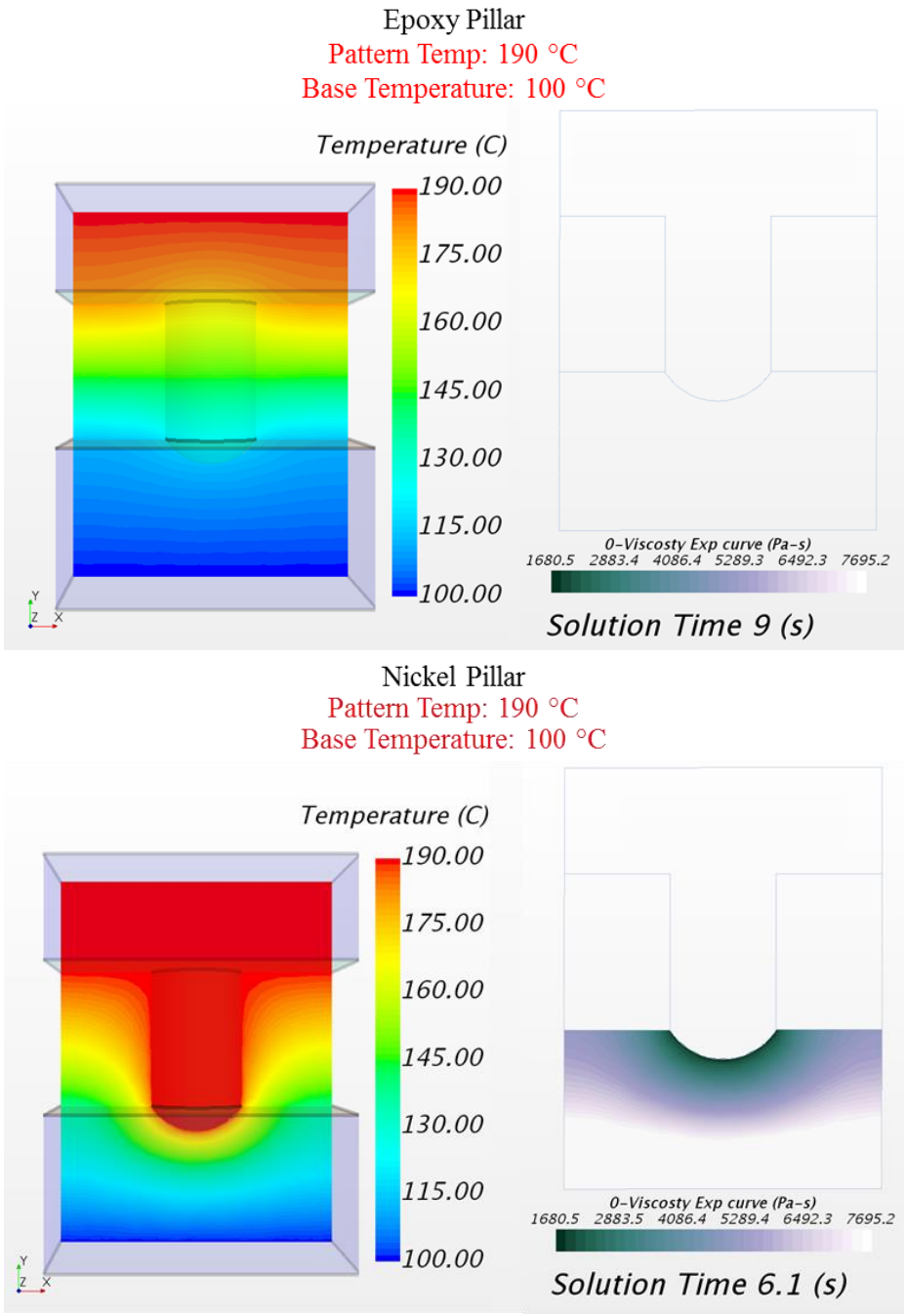

Figure A.14. Thermal modeling of epoxy and nickel micropillars at 190 °C in contact with 9508 at 100 °C

Figure A.14 depicts both the temperature (left) and viscosity (right) gradients of the system after a given experimental time. The temperature gradients were modeled using the

experimentally determined heat capacity of the 9508 polymer as well as the thermal conductivities of the epoxy and nickel [176,177], while the viscosity gradients were defined using knowledge of the polymer's zero-shear viscosity as a function of temperature. In the top image of Figure A.14, it is clear that heating the base of the epoxy micropillar to 190 °C fails to raise the temperature of the film above the polymer's melting temperature. This is further reflected by the viscosity gradient, which indicated no change in the film's viscosity around the area in contact with the pillar. This large thermal gradient is a consequence of the poor thermal conductivity of the epoxy. The bottom image of Figure A.14 shows the effect of changing the micropillar material from epoxy to nickel, which has a much higher thermal conductivity. The polymer film surrounding the area in contact with the pillar can successfully be raised above its melting temperature (125 °C), as evidenced by the light blue, green, yellow, and red colors visible within the film. Additionally, there is clearly a gradient of the zero-shear viscosity within the film corresponding to the temperature gradient.

This experiment was repeated a number of times by assigning a range of temperatures to the pattern and the film. In some cases, the rounded micropillars were arrayed to visualize the effect of neighboring pillars on the melt volume produced within the 9508 film. Figure A.15 shows the results of a simulation using arrayed epoxy and nickel pillars with respective pattern and base temperatures of 160 °C and 120 °C.

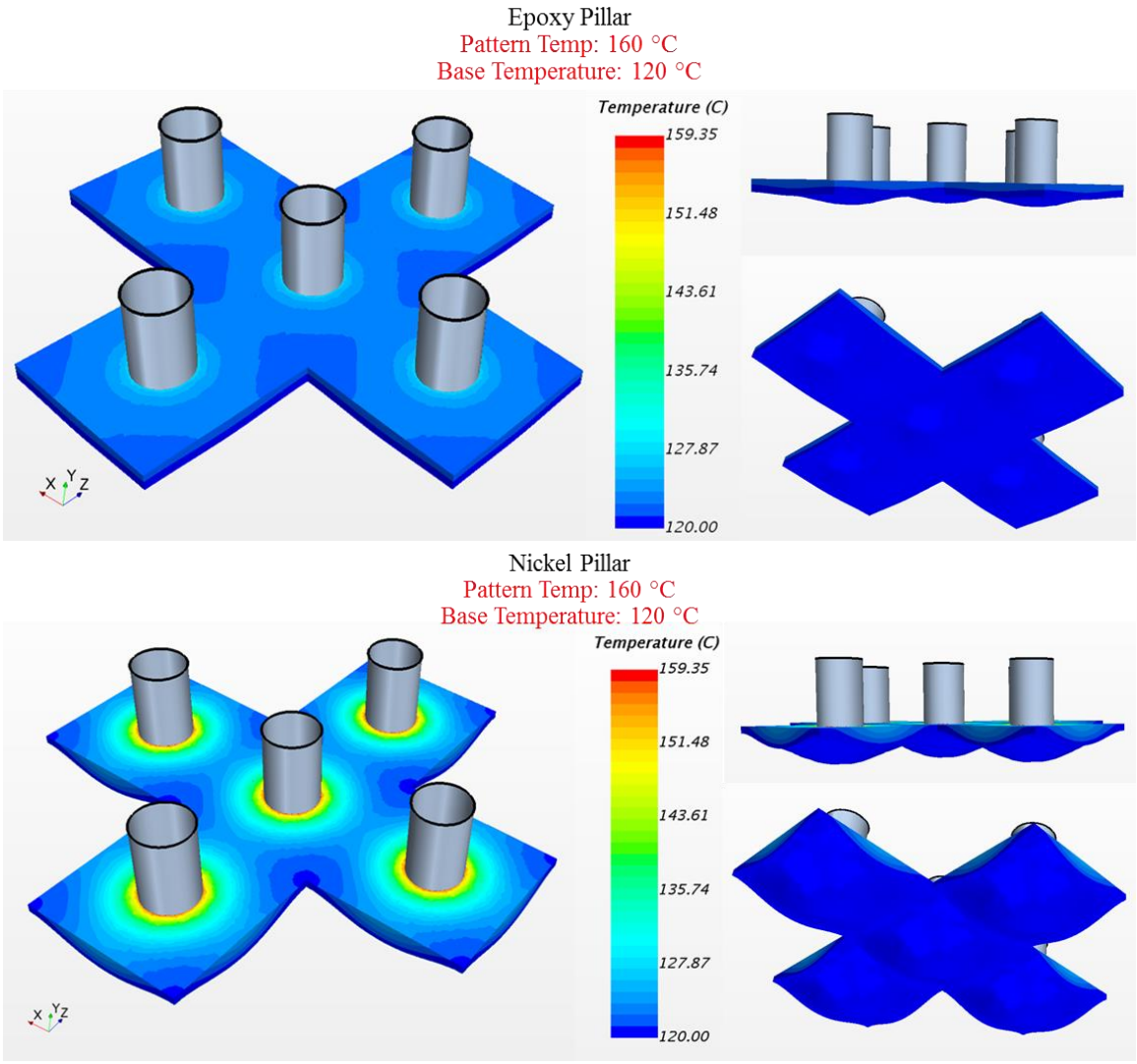

Figure A.15. Thermal modeling of epoxy and nickel micropillars at 160 °C in contact with 9508 at 120 °C

With the temperature of the film prescribed to be very close to the polymer's melt temperature, it can be seen in the top image of Figure A.15 that an epoxy pattern at 160 °C does produce some molten volume. However, the effect is much more pronounced with the nickel pattern shown in the bottom image. The melt volumes produced by the epoxy and nickel pillars were computed, and it was found that the melt volume increased by 31% when the pillar material was changed from epoxy to nickel. These modeling results further emphasize the potential benefit of using a high thermal conductivity material for the upper

patterns to induce local melting. Efforts to improve the electroforming process to produce pristine metallic rounded micropillar arrays are ongoing, and we hope to extend this process to micropillars with diameters of 50 μm in the future.

REFERENCES

[1] W. Federle, M. Riehle, A. Curtis and R. Full, "An Integrative Study of Insect Adhesion: Mechanics and Wet Adhesion of Pretarsal Pads in Ants," *Integrative and Comparative Biology*, pp. 1100-1106, 2002.

[2] J. Eisenhaure and S. Kim, "A Review of the State of Dry Adhesives: Biomimetic Structures and the Alternative Designs They Inspire," *Micromachines*, pp. 1-38, 2017.

[3] L. Heepe and S. Gorb, "Biologically Inspired Mushroom-Shaped Adhesive Microstructures," *Annual Review of Materials Research,* pp. 173-203, 2014.

[4] S. Wang, K. Liu, X. Yao and L. Jiang, "Bioinspired Surfaces with Superwettability: New Insight on Theory, Design, and Applications," *Chemical Reviews,* pp. 8230-8293, 2015.

[5] Z. Han, X. Feng, Z. Guo, S. Niu and L. Ren, "Flourishing Bioinspired Antifogging Materials with Superwettability: Progresses and Challenges," *Advanced Materials,* vol. 30, no. 13, pp. 1-32, 2018.

[6] Z. Han, Z. Mu, W. Yin, W. Li, S. Niu, J. Zhang and L. Ren, "Biomimetic Multifunctional Surfaces Inpired from Animals," *Advances in Colloid and Interface Science,* vol. 234, pp. 27-50, 2016.

[7] B. Bhushan, "Bioinspired Structured Surfaces," *Langmuir,* vol. 28, no. 3, pp. 1698-1714, 2012.

[8] H. Zhu, Z. Guo and W. Liu, "Biomimetic Water-Collecting Materials Inspired by Nature," *Chemical Communications,* vol. 52, no. 20, pp. 3863-3879, 2016.

[9] X. Gao, X. Yan, X. Yao, L. Xu, J. Zhang, B. Yang and L. Jiang, "The Dry-Style Antifogging Properties of Mosquito Compound Eyes and Artificial Analogues Prepared by Soft Lithography," *Advanced Materials,* vol. 19, no. 17, pp. 2213-2217, 2007.

[10] J. Ju, H. Bai, Y. Zheng, T. Zhao, R. Fang and L. Jiang, "A Multi-Structural and Multi-Functional Integrated Fog Collection System in Cactus," *Nature Communications,* vol. 3, pp. 1-6, 2012.

[11] M. Liu, S. Wang and L. Jiang, "Nature-Inspired Superwettability Systems," *Nature Reviews Materials,* vol. 2, no. 17036, pp. 1-17, 2017.

[12] B. Su, Y. Tian and L. Jiang, "Bioinspired Interfaces with Superwettability: From Materials to Chemistry," *Journal of the American Chemical Society,* vol. 138, no. 6, pp. 1727-1748, 016.

[13] L. Boesel, C. Greiner, E. Arzt and A. Campo, "Gecko-Inspired Surfaces: A Path to Strong and Reversible Dry Adhesives," *Advanced Materials,* vol. 22, no. 19, pp. 2125-2137, 2010.

[14] K. Liu, J. Du, J. Wu and L. Jiang, "Superhydrophobic Gecko Feet with High Adhesive Forces Towards Water and their Bio-Inspired Materials," *Nanoscale,* vol. 4, pp. 768-772, 2012.

[15] T. W. Kim and B. Bhushan, "The Adhesion Model Considering Capillarity for Gecko Attachment System," *Journal of the Royal Society Interface,* pp. 319-327, 2008.

[16] B. Soltannia and D. Sameoto, "Strong, Reversible Underwater Adhesion via Gecko-Inspired Hydrophobic Fibers," *ACS Applied Materials & Interfaces,* pp. 21995-22003, 2014.

[17] K. Autumn, P. Niewiarowski and J. Puthoff, "Gecko Adhesion as a Model System for Integrative Biology, Interdisciplinary Science, and Bioinspired Engineering," *Annual Review of Ecology, Evolution, and Systematics,* vol. 45, pp. 445-470, 2014.

[18] P. Niewiarowski, A. Stark and A. Dhinojwala, "Sticking to the Story: Outstanding Challenges in Gecko-Inspired Adhesives," *Journal of Experimental Biology,* vol. 219, pp. 912-919, 2016.

[19] M. K. Kwak, H.-E. Jeong and K. Suh, "Rational Design and Enhanced Biocompatibility of a Dry Adhesive Medical Skin Patch," *Advanced Materials,* vol. 23, no. 34, pp. 3949-3953, 2011.

[20] K. Liu, X. Yao and L. Jiang, "Recent Developments in Bio-Inspired Special Wettability," *Chemical Society Reviews,* vol. 39, no. 8, pp. 3240-3255, 2010.

[21] M. Kamperman, E. Kroner, A. del Campo, R. McMeeking and E. Arzt, "Functional Adhesive Surfaces with “Gecko” Effect: The Concept of Contact Splitting," *Advanced Engineering Materials,* vol. 12, no. 5, pp. 335-348, 2010.

[22] W. H. Banks and C. C. Mill, "Tacky Adhesion-A Preliminary Study," *Journal of Colloid Science,* vol. 8, no. 1, pp. 137-147, 1953.

[23] A. Biswas, I. Bayer, A. Biris, T. Wang, E. Dervishi and F. Faupel, "Advances in Top-Down and Bottom-Up Surface Nanofabrication: Techniques, Application, and Future Prospects," *Advances in Colloid and Interface Science,* pp. 2-27, 2012.

[24] W. Khaled and D. Sameoto, "Fabrication and Characterization of Thermoplastic Elastomer Dry Adhesives with High Strength and Low Contamination," *ACS Applied Materials & Interfaces,* pp. 6806-6815, 2014.

[25] D. Brodoceanu, C. Bauer, E. Kroner, E. Arzt and T. Kraus, "Hierarchical Bioinspired Adhesive Surfaces--A Review," *Bioinspiration and Biomimetics,* vol. 11, no. 5, p. 051001, 2016.

[26] C. Zhang, D. McAdams and J. Grunlan, "Nano/Micro- Manufacturing of Bioinspired Materials: a Review of Methods to Mimic Natural Structures," *Advanced Materials,* vol. 28, no. 30, pp. 6292-6321, 2016.

[27] B. Aksak, M. Murphy and M. Sitti, "Adhesion of Biologically Inspired Vertical and Angled Polymer Microfiber Arrays," *Langmuir,* pp. 3322-3332, 2007.

[28] W. G. Bae, D. Kim, M. K. Kwak, L. Ha, S. M. Kang and K. Suh, "Enhanced Skin Adhesive Patch with Modulus- Tunable Composite Micropillars," *Advanced Healthcare Materials,* vol. 2, no. 1, pp. 109-113, 213.

[29] P. Glass, H. Chung, N. Washburn and M. Sitti, "Enhanced Wet Adhesion and Shear of Elastomeric Micro-Fiber Arrays with Mushroom Tip Geometry and a Photopolymerized p(DMA-co-MEA) Tip Coating," *Langmuir,* vol. 26, no. 22, pp. 17357-17362, 2010.

[30] S. Gorb, M. Varenberg, A. Peressadko and J. Tuma, "Biomimetic Mushroom-Shaped Fibrillar Adhesive Microstructure," *Journal of the Royal Society Interface,* pp. 271-275, 2007.

[31] H. Hu, H. Tian, X. Li, J. Shao, Y. Ding, H. Liu and N. An, "Biomimetic Mushroom-Shaped Microfibers for Dry Adhesives by Electrically Induced Polymer Deformation," *ACS Applied Materials & Interfaces,* pp. 14167-14173, 2014.

[32] Y. Wang, H. Hu, J. Shao and Y. Ding, "Fabrication of Well-Defined Mushroom-Shaped Structures for Biomimetic Dry Adhesive by Conventional Photolithography and Molding," *ACS Applied Materials and Interfaces,* vol. 6, no. 4, pp. 2213-2218, 2014.

[33] J.-K. Chen, F.-H. Wang, J.-Y. Chang and S.-K. Fan, "Thermally Switchable Adhesion of Polystyrene-block-poly(n-isopropylacrylamide) Copolymer Pillar Aray Mimicking Climb Altitude of Geckos," *Applied Physics Letters,* vol. 101, no. 12, 2012.

[34] D. Sameoto and C. Menon, "Deep UV Patterning of Acrylic Masters for Molding Biomimetic Dry Adhesives," *Journal of Micromechanics and Microengineering,* vol. 20, p. 115037, 2010.

[35] T. Kim, J. Park, J. Sohn, D. Cho and S. Jeon, "Bioinspired, Highly Stretchable, and Conductive Dry Adhesives Based on 1D-2D Hybrid Carbon Nanocomposites for All-in-One ECG Electrodes," *ACS Nano,* pp. 4770-4778, 2016.

[36] M. Murphy, B. Aksak and M. Sitti, "Gecko-Inspired Directional and Controllable Adhesion," *Small,* vol. 5, no. 2, 2009.

[37] M. Murphy, B. Aksak and M. Sitti, "Adhesion and Anisotropic Friction Enhancements of Angled Heterogeneous Micro-Fiber Arrays with Spherical and Spatula Tips," *Journal of Adhesion Science and Technology,* pp. 1281-1296, 2007.

[38] J. DeFranco, B. Schmidt, M. Lipson and G. Malliaras, "Photolithographic Patterning of Organic Electronic Materials," *Organic Electronics,* pp. 22-28, 2006.

[39] R. Zaouk, B. Park and M. Madou, "Introduction to Microfabrication Techniques," in *Microfluidic Techniques: Reviews and Protocols*, Totowa, Humana Press, Inc, 2006, pp. 5-16.

[40] K.-S. Chen, A. Ayon, X. Zhang and S. Spearing, "Effect of Process Parameters on the Surface Morphology and Mechanical Performance of Silicon Structures after Deep Reactive Ion Etching (DRIE)," *Journal of Microelectromechanical Systems,* vol. 11, no. 3, pp. 264-275, 2002.

[41] T. Wienhold, S. Kraemmer, S. Wondimu, T. Siegle, U. Bog, U. Weinzierl, S. Schmidt, H. Becker, H. Kalt, T. Mappes, S. Koeber and C. Koos, "All-Polymer Photonic Sensing Platform Based on Whispering-Gallery Mode Microgoblet Lasers," *Lab on a Chip,* pp. 3800-3806, 2015.

[42] A. Bell, "Micro-Scale Bio-Inspired Structured Polymer Surfaces for Tissue Adhesion," The University of Leeds School of Mechanical Engineering, 2015.

[43] M. Liu, Y. Zheng, J. Zhai and L. Jiang, "Bioinspired Super-antiwetting Interfaces with Special Liquid-Solid Adhesion," *Accounts of Chemical Research,* vol. 43, no. 3, pp. 368-377, 2010.

[44] A. Ji, L. Han and Z. Dai, "Adhesive Contact in Animal: Morphology, Mechanism, and Bio-Inspired Application," *Journal of Bionic Engineering,* vol. 8, no. 4, pp. 345-356, 2011.

[45] L. Heepe, L. Xue and S. Gorb, Bio-Inspired Structured Adhesives, Springer International Publishing, 2017.

[46] V. Tinnemann, L. Hernandez, S. Fischer, E. Arzt, R. Bennewitz and R. Hensel, "In Situ Observation Reveals Local Detachment Mechanisms and Suction Effects in Micropatterned Adhesives," *Advanced Functional Materials,* vol. 29, no. 14, pp. 1-11, 2019.

[47] J. Karp and R. Langer, "Dry Solution to a Sticky Problem," *Nature,* vol. 477, pp. 42-43, 2011.

[48] T. Sun, L. Feng, X. Gao and L. Jiang, "Bioinspired Surfaces with Special Wettability," *Accounts of Chemical Research,* vol. 38, no. 8, pp. 644-652, 2005.

[49] K. Liu and L. Jiang, "Multifunctional Integration: From Biological to Bio-Inspired Materials," *ACS Nano,* vol. 5, no. 9, pp. 6786-6790, 2011.

[50] K. Liu and L. Jiang, "Bio-Inspired Design of Multiscale Structures for Function Integration," *Nanotoday,* vol. 6, no. 2, pp. 155-175, 2011.

[51] T.-i. Kim, H. E. Jeong, K. Suh and H. Lee, "Stooped Nanohairs: Geometry- Controllable, Unidirectional, Reversible, and Robust Gecko- like Dry Adhesive," *Advanced Materials,* vol. 21, no. 22, pp. 2276-2281, 2009.

[52] B. Persson and S. Gorb, "The Effect of Surface Roughness on the Adhesion of Elastic Plates with Application to Biological Systems," *The Journal of Chemical Physics,* vol. 119, no. 21, pp. 11437-11444, 2003.

[53] W. Federle, "Why are so many adhesive pads hairy?," *Journal of Experimental Biology,* vol. 209, pp. 2611-2621, 2006.

[54] R. Hensel, K. Moh and E. Arzt, "Engineering Micropatterned Dry Adhesives: From Contact Theory to Handling Applications," *Advanced Functional Materials,* vol. 28, no. 28, 2018.

[55] N. Glassmaker, A. Jagota, C.-Y. Hui, W. Noderer and M. Chaudhury, "Biologically Inspired Crack Trapping for Enhanced Adhesion," *Proceedings of the National Academy of Sciences of the United States of America,* pp. 10786-10791, 2007.

[56] M. Zhou, N. Pesika, H. Zeng, Y. Tian and J. Israelachvili, "Recent Advances in Gecko Adhesion and Friction Mechanisms and Development of Gecko-Inspired Dry Adhesive Surfaces," *Friction,* vol. 1, no. 2, pp. 114-129, 2013.

[57] Y. Tian, N. Pesika, H. Zeng, K. Rosenberg, B. Zhao, P. McGuiggan, K. Autumn and J. Israelachvili, "Adhesion and Friction in Gecko Toe Attachment and Detachment," *PNAS,* vol. 103, no. 51, pp. 19320-19325, 2006.

[58] M. Kwak, C. Pang, H.-E. Jeong, H.-N. Kim, H. Yoon, H.-S. Jung and K.-Y. Suh, "Towards the Next Level of Bioinspired Dry Adhesives: New Designs and Applications," *Advanced Functional Materials,* vol. 21, no. 19, pp. 3606-3616, 2011.

[59] K. Autumn and N. Gravish, "Gecko Adhesion: Evolutionary Nanotechnology," *Philosophical Transactions of the Royal Society A,* vol. 366, no. 1870, 2008.

[60] B. Persson, "Wet Adhesion with Application to Tree Frog Adhesive Toe Pads and Tires," *Journal of Physics: Condensed Matter,* vol. 19, no. 37, 2007.

[61] D.-M. Drotlef, L. Stepien, M. Kappl, W. Barnes, H.-J. Butt and A. del Campo, "Insights into the Adhesive Mechanisms of Tree Frogs Using Artificial Mimics," *Advanced Functional Materials,* vol. 23, no. 9, pp. 1137-1146, 2013.

[62] M. Kappl, F. Kaveh and W. Barnes, "Nanoscale Friction and Adhesion of Tree Frog Toe Pads," *Bioinspiration and Biomimetics,* vol. 11, no. 3, 2016.

[63] F. Grasso and P. Setlur, "Inspiration, Simulation, and Design for Smart Robot Manipulators from the Sucker Actuation Mechanism of Cephalopods," *Bioinspiration and Biomimetics,* vol. 2, no. 4, pp. S170-S181, 2007.

[64] F. Tramacere, L. Beccai, M. Kuba, A. Gozzi, A. Bifone and B. Mazzolai, "The Morphology and Adhesion Mechanism of Octopus Vulgaris Suckers," *PLoS One,* vol. 8, no. 6, 2013.

[65] F. Tramacere, L. Beccai, F. Mattioli, E. Sinibaldi and B. Mazzolai, "Artificial Adhesion Mechanisms Inspired by Octopus Suckers," in *IEEE International Conference on Robotics and Automation,* Saint Paul, MN, 2012.

[66] F. Tramacere, N. Pugno, M. Kuba and B. Mazzolai, "Unveiling the Morphology of the Acetabulum in Octopus Suckers and its Role in Attachment," *Interface Focus,* vol. 5, no. 1, 2015.

[67] R. Aiken and A. Khan, "The Adhesive Strength of Males of a Boreal Water Beetle, Dysticus Alaskanus J. Balfour Browne (Coleoptera: Dystiscidae)," *Canadian Journal of Zoology,* pp. 1321-1324, 1992.

[68] J. Bergsten, "Taxonomy, Phylogeny, and Secondary Sexual Character Evolution of Diving Beetles, Focusing on the Genus Acilius," Umea University Department of Ecology and Environmental Science, Umea, 2005.

[69] Y. Chen, M.-C. Shih, M.-H. Wu, E.-C. Yang and K.-J. Chi, "Underwater Attachment Using Hairs: the Functioning of Spatula and Sucker Setae from Male Diving Beetles," *Journal of the Royal Society Interface,* pp. 1-12, 2014.

[70] K. Green, A. Kovalev, E. Svensson and S. Gorb, "Male Clasping Ability, Female Polymorphism, and Sexual Conflict: Fine-Scale Elytral Morphology as a Sexually Antagonistic Adaptation in Female Diving Beetles," *Interface,* vol. 10, no. 86, 2013.

[71] S. Holmgren, R. Angus, F. Jia, Z.-n. Chen and J. Bergsten, "Resolving the Taxonomic Conundrum in Graphoderus of the East Palearctic with a Key to All Species," *ZooKeys,* vol. 574, pp. 113-142, 2016.

[72] G. Walker, "Adhesion to Smooth Surfaces by Insects--a Review," *International Journal of Adhesion and Adhesives,* vol. 13, no. 1, pp. 3-7, 1993.

[73] R. Spolenak, S. Gorb, H. Gao and E. Arzt, "Effects of Contact Shape on the Scaling of Biological Attachments," *Proceedings of the Royal Society A,* vol. 461, no. 2054, pp. 305-319, 2005.

[74] R. O'Rorke, T. Steele and H. Taylor, "Bioinspired Fibrillar Adhesives: A Review of Analytical Models and Experimental Evidence for Adhesion Enhancement by Surface Patterns," *Journal of Adhesion Science and Technology,* vol. 30, no. 4, pp. 362-391, 2016.

[75] S. Fischer, K. Grob, O. Abad, M. Becker, E. Park, R. Hensel and E. Arzt, "Funnel-Shaped Microstructures for Strong Reversible Adhesion," *Advanced Materials Interfaces,* vol. 4, no. 20, p. 1700292, 2017.

[76] L. Heepe, M. Varenberg, Y. Itovich and S. Gorb, "Suction Component in Adhesion of Mushroom-Shaped Microstructure," *Journal of the Royal Society Interface,* pp. 585-589, 2011.

[77] R. Manabe, K. Suzumori and S. Wakimoto, "A Functional Adhesive Robot Skin with Integrated Micro Rubber Suction Cups," in *IEEE International Conference on Robotics and Automation*, Saint Paul, 2012.

[78] D. Sameoto and C. Menon, "Recent Advances in the Fabrication and Adhesion Testing of Biomimetic Dry Adhesives," *Smart Materials and Structures,* vol. 19, p. 103001, 2010.

[79] A. Wasay and D. Sameoto, "Gecko Gaskets for Self-Sealing and High-Strength Reversible Bonding of Microfluidics," *Lab on a Chip,* vol. 15, pp. 2749-2753, 2015.

[80] A. Crosby, M. Hageman and A. Duncan, "Controlling Polymer Adhesion with “Pancakes”," *Langmuir,* pp. 11738-11743, 2005.

[81] M. Lamblet, E. Verneuil, T. Vilmin, A. Buguin, P. Silberzan and L. Leger, "Adhesion Enhancement through Micropatterning at Polydimethylsiloxane-Acrylic Adhesive Interfaces," *Langmuir,* vol. 23, no. 13, pp. 6966-6974, 2007.

[82] S. Lee, C. Park and M. Kwak, "Continuous Fabrication of Wide-Tip Microstructures for Bio-Inspired Dry Adhesives via Tip Inking Process," *Journal of Chemistry,* vol. 2019, p. 4827918, 2019.

[83] S. Kim and M. Sitti, "Biologically Inspired Polymer Microfibers with Spatulate Tips as Repeatable Fibrillar Adhesives," *Applied Physics Letters,* vol. 89, p. 261911, 2006.

[84] D. Sameoto and C. Menon, "A Low-Cost, High-Yield Fabrication Method for Producing Optimized Biomimetic Dry Adhesives," *Journal of Micromechanics and Microengineering,* vol. 19, no. 11, p. 115002, 2009.

[85] J.-Y. Lee, S.-H. Kim, H.-T. Lim, C.-H. Kim, C.-W. Baek and Y.-K. Kim, "Electric Spring Modeling for a Comb Actuator Deformed by the Footing Effect in Deep Reactive Ion

Etching," *Journal of Micromechanics and Microengineering,* vol. 13, no. 1, pp. 72-79, 2002.

[86] Y. Wang, Y. Guo and H. Zhang, "Modeling and Simulation of the Footing Effect in DRIE Process," in *IEEE Conference on Nanotechnology*, Hong Kong, 2007.

[87] R. Manabe, K. Suzumori and S. Wakimoto, "Robot Skin with Integrated Micro Rubber Suction Cups Adhering Rough Surfaces," in *IEEE/RSJ International Conference on Intelligent Robots and Systems*, Tokyo, 2013.

[88] M. Choi, O. Park, C. Choi, S. Qiao, R. Ghaffari, J. Kim, D. Lee, M. Kim, W. Hyun, S. Kim, H. Hwang and S.-H. Kwon, "Cephalopod-Inspired Miniaturized Suction Cups for Smart Medical Skin," *Advanced Healthcare Materials,* vol. 5, no. 1, pp. 80-87, 2016.

[89] S. Baik, J. Kim, H. Lee, T. Lee and C. Pang, "Highly Adaptable and Biocompatible Octopus- Like Adhesive Patches with Meniscus- Controlled Unfoldable 3D Microtips for Underwater Surface and Hairy Skin," *Advanced Science,* vol. 5, no. 8, p. 1800100, 2018.

[90] N. Thanh-Vinh, H. Takahashi, T. Kan, K. Noda, K. Matsumoto and I. Shimoyama, "Micro Suction Cup Array for Wet/Dry Adhesion," in *Micro Electro Mechanical Systems (MEMS)*, Cancun, 2011.

[91] S. Chary, J. Tamelier and K. Turner, "A microfabricated Gecko-Inspired Controllable and Reusable Dry Adhesive," *Smart Materials and Structures,* vol. 22, no. 2, p. 025013, 2013.

[92] Y. Li, D. Sameoto and C. Menon, "Enhanced Compliant Adhesive Design and Fabrication with Dual-Level Hierarchical Structure," *Journal of Bionic Engineering,* vol. 7, no. 3, pp. 228-234, 2010.

[93] M. Murphy, S. Kim and M. Sitti, "Enhanced Adhesion by Gecko-Inspired Hierarchical Fibrillar Adhesives," *ACS Applied Materials & Interfaces,* vol. 1, no. 4, pp. 849-85, 2009.

[94] T. Kustandi, V. Samper, D. Yi, W. Ng, P. Neuzil and W. Sun, "Self-Assembled Nanoparticle-Based Fabrication of Gecko Foot Hair-Inspired Polymer Nanofibers," *Advanced Functional Materials,* vol. 17, pp. 2211-2218, 2007.

[95] Y.-C. Chen and H. Yang, "Octopus-Inspired Assembly of Nanosucker Arrays for Dry/Wet Adhesion," *ACS Nano,* vol. 11, no. 6, pp. 5332-5338, 2017.

[96] D. Bratton, D. Yang, J. Dai and C. Ober, "Recent Progress in High Resolution Lithography," *Polymers for Advanced Technologies,* vol. 17, pp. 94-103, 2006.

[97] M. Morariu, N. Voicu, E. Schaffer, Z. Lin, T. Russell and U. Steiner, "Hierarchical Structure Formation and Pattern Replication Induced by an Electric Field," *Nature Materials,* pp. 48-52, 2003.

[98] N. Wu and W. Russel, "Micro- and Nano-Patterns Created via Electrohydrodynamic Instabilities," *Nano Today*, pp. 180-192, 2009.

[99] Z. Nie and E. Kumacheva, "Patterning Surfaces with Functional Polymers," *Nature Materials,* pp. 277-290, 2008.

[100] E. Schaffer, T. Thurn-Albrecht, T. Russell and U. Steiner, "Electrically Induced Structure Formation and Pattern Transfer," *Nature,* pp. 874-877, 2000.

[101] M. Dickey, A. Raines, E. Collister, R. Bonnecaze, S. Sreenivasan and G. Wilson, "High-Aspect Ratio Polymeric Pillar Arrays Formed via Electrohydrodynamic Patterning," *Journal of Materials Science,* pp. 117-122, 2008.

[102] X. Li, J. Shao, Y. Ding, H. Tian and H. Liu, "Improving the Height of Replicaiton in EHD Patterning by Optimizing the Electrical Properties of the Template," *Journal of Micromechanics and Microengineering*, vol. 21, no. 11, 2011.

[103] P. Goldberg-Oppenheimer and U. Steiner, "Rapid Electrohydrodynamic Lithography Using Low-Viscosity Polymers," *Small,* vol. 6, no. 11, pp. 1248-1254, 2010.

[104] C. Trease, P. Foot and A. Augousti, "Electrohydrodynamic Patterning in a Curable Resin over a Wide Range of Fabrication Parameters," *European Polymer Journal*, vol. 91, pp. 315-325, 2017.

[105] H. Tian, J. Shao, X. Chen, L. Wang and Y. Ding, "A Versatile Approach to Fabricate Modulated Micro-/Nanostructures by Electrohydrodynamic Structuring on Prepatterned Polymer," *Jounral of Micromechanics and Microengineering*, vol. 27, no. 2, 2016.

[106] Q. Yang, B. Li, H. Tian, X. Li, J. Shao, X. Chen and F. Xu, "Deformation Hysteresis of Electrohydrodynamic Patterning on a Thin Polymer Film," *ACS Applied Materials & Interfaces,* pp. 17668-17765, 2016.

[107] X. Chen, H. Tian, X. Li, J. Shao, Y. Ding, N. An and Y. Zhou, "A High Performance P(VDF-TrFE) Nanogenerator with Self-Connected and Vertically Integrated Fibers by EHD Pulling," *Nanoscale*, pp. 11536-11544, 2015.

[108] H. Tian, J. Shao, H. Hu, L. Wang and Y. Ding, "Role of Space Charges Inside a Dielectric Polymer in the Electrohydrodynamic Structure Formation on a Prepatterned Polymer (ESF-PP)," *RSC Advances*, pp. 77275-77283, 2016.

[109] K. Lee and H. Jung, "Drawing Lithography for Microneedles: A Review of Fundamentals and Biomedical Applications," *Biomaterials,* vol. 33, no. 30, pp. 7309-7326, 2012.

[110] M. Snyder, "Microneedle Technology Makes a Splash in Drug Delivery Space," 14 July 2017. [Online]. Available: https://www.rdmag.com/article/2017/07/microneedle-technology-makes-splash-drug-delivery-space. [Accessed 1 June 2019].

[111] R. MacDougall, "Researchers Develop Microneedle Patch for Flu Vaccination," 27 June 2017. [Online]. Available: https://www.nih.gov/news-events/news-releases/researchers-develop-microneedle-patch-flu-vaccination. [Accessed 1 June 2019].

[112] H. Jeong, S. Lee, P. Kim and K. Suh, "Stretched Polymer Nanohairs by Nanodrawing," *Nano Letters,* vol. 6, no. 7, pp. 1508-1513, 2006.

[113] G. Spina, C. Stefanini, A. Menciassi and P. Dario, "A Novel Technological Process for Fabricating Micro-Tips for Biomimetic Adhesion," *Journal of Micromechanics and Microengineering,* pp. 1576-1587, 2005.

[114] J. Paek and J. Kim, "Microsphere-Assisted Fabrication of High Aspect-Ratio Elastomeric Micropillars and Waveguides," *Nature Communications,* pp. 1-8, 2014.

[115] W. Jiang, B. Lei, H. Liu, D. Niu, T. Zhao, B. Chen, L. Yin, Y. Shi and X. Liu, "Fabrication of Directional Nanopillars with High-Aspect-Ratio Using a Stretching Imprint Process with a Microcavity Mold," *Nanoscale,* pp. 2172-2177, 2017.

[116] W. Jiang, L. Wang, H. Liu, H. Ma, H. Tian, B. Chen, Y. Shi, L. Yin and Y. Ding, "Bio-Inspired Directional and High-Aspect-Ratio Nanopillars: Fabrication and Actuation," *RSC Advances,* pp. 42002-42008, 2014.

[117] C.-C. Yang and K. Wang, "Dip-drawing Process Characterization of Making High-aspect-ratio Polymeric Microneedles," in *IEEE International Conference on Advanced Manufacturing*, Yunlin, 2018.

[118] H. Yi, I. Hwang, J. Lee, D. Lee, H. Lim, D. Tahk, M. Sung, W.-G. Bae, S.-J. Choi, M. Kwak and H. Jeong, "Continuous and Scalable Fabrication of Bioinspired Dry Adhesives via a Roll-to-Roll Process with Modulated Ultraviolet-Curable Resin," *ACS Applied Materials and Interfaces,* vol. 6, no. 16, pp. 14590-14599, 2014.

[119] Y. Li, J. Krahn and C. Menon, "Bioinspired Dry Adhesive Materials and their Application in Robotics: A Review," *Journal of Bionic Engineering,* vol. 13, no. 2, pp. 181-199, 2016.

[120] "Stainless Steel," McMaster-Carr, [Online]. Available: https://www.mcmaster.com/#balls/=1cd9ulv. [Accessed 11 4 2018].

[121] S. Bochereau, B. Dzidek, M. Adams and V. Hayward, "Characterizing and Imaging Gross and Real Finger Contacts under Dynamic Loading," *IEEE Transactions on Haptics,* vol. 10, no. 4, pp. 456-465, 2017.

[122] J. Engelsma, K. Cao and A. Jain, "RapsiReader: Open Source Fingerprint Scanner," 26 December 2017. [Online]. Available: https://www.groundai.com/project/raspireader-open-source-fingerprint-reader/. [Accessed 15 October 2019].

[123] E. Eason, E. Hawkes, M. Windheim, D. Christensen, T. Libby and M. Cutkosky, "Stress Distribution and Contact Area Measurements of a Gecko Toe using a High-Resolution Tactile Sensor," *Bioinspiration and Biomimetics*, vol. 10, no. 1, 2015.

[124] V. Levesque and V. Hayward, "Experimental Evidence of Lateral Skin Strain during Tactile Exploration," in *Proceeding of Eurohaptics*, Dublin, 2003.

[125] S. Anna, "Elasto-Capillary Thinning and Breakup of Model Elastic Liquids," *Journal of Rheology*, pp. 115-138, 2001.

[126] A. Vittoria, V. Busico, F. Cannavacciuolo and R. Cipullo, "Molecular Kinetic Study of "Chain Shuttling" Olefin Copolymerization," *ACS Catalysis*, vol. 8, no. 6, pp. 5051-5061, 2018.

[127] M. Wu, Z. Wu, K. Wang, Q. Zhang and Q. Fu, "Simultaneous the Thrmodynamics Favorable Compatibility and Morphology to Achieve Excellent Comprehensive Mechanics in PLA/OBC Blend," *Polymer*, vol. 55, no. 24, pp. 6409-6417, 2014.

[128] "INFUSE Olefin Block Copolymers," Dow Chemical Company, December 2016. [Online]. Available: http://msdssearch.dow.com/PublishedLiteratureDOWCOM/dh_097c/0901b8038097c9cc.pdf?filepath=elastomers/pdfs/noreg/788-08201.pdf&fromPage=GetDoc. [Accessed 15 July 2019].

[129] "ExxonMobil LDPE LGA 105," ExxonMobil, 2019. [Online]. Available: https://exxonmobilchemical.ulprospector.com/en-US/ds244000/ExxonMobil%E2%84%A2%20LDPE%20LGA%20105.aspx?I=58933&U=1. [Accessed 15 July 2019].

[130] S. Chum and K. Swogger, "Olefin Polymer Technologies-History and Recent Progress at The Dow Chemical Company," *Progress in Polymer Science*, vol. 33, no. 8, pp. 797-819, 2008.

[131] X. Zhou, J. Feng, D. Cheng, J. Yi and L. Wang, "Different Crystallization Behavior of Olefin Block Copolymer in α- and β-Polypropylene Matrix," *Polymer*, vol. 54, no. 17, pp. 4719-4727, 2013.

[132] M. Sentmanat, B. Wang and G. McKinley, "Measuring the Transient Extensional Rheology of Polyethylene Melts using the SET Universal Testing Platform," *Journal of Rheology*, vol. 49, no. 3, pp. 585-606, 2005.

[133] J. Humbeeck, "Simultaneous Thermal Analysis," in *Handbook of Thermal Analysis and Calorimetry Volume 1: Principles and Practice*, Amsterdam, Elsevier Science, B. V., 1998, pp. 497-508.

[134] N. Cheremisinoff, "Thermal Analysis," in *Polymer Characterization Laboratory Techniques and Analysis*, Westwood, Noyes Publications, 1996, pp. 17-24.

[135] A. S. D3418, *Standard Test Method for Transition Temperatures and Enthalpies of Fusion and Crystallization of Polymers by Differential Scanning Calorimetry,* West Conshohocken, PA, 2015.

[136] R. Blaine, "Thermal Applications Note Polymer Heats of Fusion," TA Instruments, [Online]. Available: http://www.tainstruments.com/pdf/literature/TN048.pdf. [Accessed 3 July 2019].

[137] Y. Yuan and R. Lee, "Contact Angle and Wetting Properties," in *Surface Science Techniques*, Heidelberg, Springer, 2013, pp. 3-29.

[138] M. Bracke, F. De Voeght and P. Joos, "The Kinetics of Wetting: The Dynamic Contact Angle," *Progress in Colloid & Polymer Science,* pp. 142-149, 1989.

[139] G. Zitzenbacher, H. Dirnberger and C. Holzer, "Calculation of the Contact Angle of Polymer Melts on Tool Surfaces from Viscosity Parameters," *Polymers,* vol. 10, no. 1, 2017.

[140] H. Schonhorn, H. Frisch and T. Kwei, "Kinetics of Wetting of Surfaces by Polymer Melts," *Journal of Applied Physics,* pp. 4967-4973, 1966.

[141] "Drop Shape Analysis," EPFL, 20 October 2013. [Online]. Available: http://bigwww.epfl.ch/demo/dropanalysis/. [Accessed 3 July 2019].

[142] R. Bird, R. Armstrong and O. Hassager, Dynamics of Polymeric Liquids Vol 1, 2nd Ed: Fluid Mechanics, John Wiley and Sons Inc, 1987.

[143] J. Dealy and J. Wang, "Linear Viscoelasticity and Nonlinear Viscoelasticity: Phenomena," in *Melt Rheology and its Applications in the Plastics Industry*, Dordrecht, Springer Science and Business Media, 2013, pp. 49-113.

[144] A. Kumar and R. Gupta, "Flow Behavior of Polymeric Fluids," in *Fundamentals of Polymer Engineering*, New York City, Marcel Dekker, Inc., 2003, pp. 573-629.

[145] A. Franck, "Rheology and Structure-Rheology Relationship for Thermoplastics," TA Instruments.

[146] M. Rubinstein and R. Colby, "Networks and Gels," in *Polymer Physics*, Oxford, Oxford University Press, 2003, pp. 282-295.

[147] Z. Tadmor and C. Gogos, "Polymer Rheology and Non-Newtonian Fluid Mechanics," in *Principles of Polymer Processing*, Hoboken, John Wiley & Sons, 2006, pp. 79-132.

[148] G. Peters, J. Schoonen, F. Baaijens, and H. Meijer, "On the Performance of Enhanced Constitutive Models for Polymer Melts in a Cross-Slot Flow," *Journal of Non-Newtonian Fluid Mechanics*, vol. 82, pp. 387-427, 1999.

[149] P. Lomellini, "Williams-Landel-Ferry Versus Arrhenius Behaviour: Polystyrene Melt Viscoelasticity Revised," *Polymer*, vol. 33, no. 23, pp. 4983-4989, 1992.

[150] M. Bohn, "The Connection Between the Parameters of WLF Equaiton and of Arrhenius Equation," *Propellants, Explosives, Pyrotechnics*, vol. 44, pp. 696-705, 2019.

[151] T. Ondarcuhu, "Tack of a Polymer Melt: Adhesion Measurements and Fracture Profile Observations," *Journal of Physics II France,* pp. 1893-1916, 1997.

[152] A. Crosby and K. Shull, "Adhesive Failure Analysis of Pressure-Sensitive Adhesives," *Polymer Physics,* vol. 37, no. 24, pp. 3455-3472, 1999.

[153] F. Mazzeo, "Characterization of Pressure Sensitive Adhesives by Rheology," TA Instruments, [Online]. Available: http://www.tainstruments.com/pdf/literature/RH082.pdf. [Accessed 22 July 2019].

[154] D. Hoyle and S. Fielding, "Criteria for Extensional Necking Instability in Complex Fluids and Soft Solids. Part I: Imposed Henkcy Strain Rate Protocol," *Journal of Rheology*, vol. 60, no. 6, 2016.

[155] F. Deplace, C. Carelli, S. Mariot, H. Retsos, A. Chateauminois, K. Ouzined and C. Creton, "Fine Tuning the Adhesive Properties of a Soft Nanostructured Adhesives with Rheological Measurements," *The Journal of Adhesion,* vol. 85, pp. 18-54, 2009.

[156] E. Narimissa, R. Gupta, N. Kao, D. Nguyen and S. Bhattacharya, "Extensional Rheological Investigation of Biodegradable Polylactide-Nanogrpahite Platelet Composites via Constitutive Equation Modeling," *Macromolecular Materials and Engineering,* vol. 299, no. 7, pp. 851-868, 2014.

[157] G. McKinley, S. Anna, A. Tripathi and M. Yao, "Extensional Rheology of Polymeric Fluids and the Uniaxial Elongation of Viscoelastic Filaments," in *International Polymer Processing Society*, 1999.

[158] A. Malkin, A. Arinstein and V. Kulichikhin, "Polymer Extension Flows and Instabilities," *Progress in Polymer Science,* pp. 959-978, 2014.

[159] S. Anna and G. McKinley, "Elasto-Capillary Thinning and Breakup of Model Elastic Liquids," *Journal of Rheology,* pp. 115-138, 2001.

[160] M. Chellamuthu, D. Arora, H. Winter and J. Rothstein, "Extensional Flow-Induced Crystallization of Isotactic Poly-1-Butene Using a Filament Stretching Rheometer," *Journal of Rheology,* vol. 901, 2011.

[161] Z. Stary, M. Papp and T. Burghelea, "Deformation Regimes, Failure, and Rupture of a Low Density Polyethylene (LDPE) Melt Undergoing Uniaxial Extension," *Journal of Non-Newtonian Fluid Mechanics,* vol. 219, pp. 35-49, 2015.

[162] H. Sun and S.-Q. Wang, "Shear and Extensional Rheology of Entangled Polymer Melts: Similarities and Differences," *Science China Chemistry,* pp. 779-786, 2012.

[163] G. McKinley and T. Sridhar, "Filament-Stretching Rheometry of Complex Fluids," *Annual Reviewof Fluid Mechanics,* pp. 375-415, 2002.

[164] L. Vagharchakian, F. Restagno and L. Leger, "Capillary Bridge Formation and Breakage: A Test to Characterize Antiadhesive Surfaces," *Journal of Physical Chemistry B,* pp. 3769-3775, 2009.

[165] Y. Wang, P. Boukany, S.-Q. Wang and X. Wang, "Elastic Breakup in Uniaxial Extension of Entangled Polymer Melts," *Physical Review Letters,* pp. 237801:1-4, 2007.

[166] A. Malkin and G. Vinogradov, "Fracture of Polymers in the Visco-Fluid State on Stretching: Review," *Polymer Science USSR,* vol. 27, no. 2, pp. 245-257, 1985.

[167] T. Chen, "Strategies for Rheological Evaluation of Pressure Sensitive Adhesives," Pressure Sensitive Tape Council, [Online]. Available: https://www.pstc.org/files/public/Chen_Terri.pdf. [Accessed 22 July 2019].

[168] P. Elemans, J. Janssen and H. Meijer, "The Measurement of Interfacial Tension in Polymer/Polymer Systems: the Breaking Thread Method," *Journal of Rheology,* vol. 34, no. 8, pp. 131-1325, 1990.

[169] T. d. L. Magistrale, "Analysis of the Effect of Different Coatings on Ejection Forces in Micro Injection Molding," University of Padua, Padua, 2017.

[170] M. Wouters and B. Ruiter, "Contact-Angle Developement of Polymer Melts," *Progress in Organic Coatings,* vol. 48, no. 2-4, pp. 207-213, 2003.

[171] K. Shull, "Wetting Autophobicity of Polymer Melts," *Faraday Discussions,* vol. 98, pp. 203-217, 1994.

[172] T.-S. Jiang, S.-G. Oh and J. Slattery, "Correction for Dynamic Contact Angle," *Journal of Colloid and Interface Science,* vol. 69, no. 1, pp. 74-77, 1979.

[173] J. Paek, "Unconventional Elastomeric Systems: Fabrication and Application," Iowa State University, Ames, 2015.

[174] K. Holbrook and G. Odland, "Regional Differences in the Thickness (Cell Layers) of hte Human Stratum Corneum: An Ultrastructural Analysis," *Journal of Investigative Dermatology,* vol. 62, no. 4, pp. 415-422, 1974.

[175] J. McGeough, M. Leu, K. Rajurkar, A. De Silva and Q. Liu, "Electroforming Process and Application to Micro/Macro Manufacturing," *CIRP Annals,* vol. 50, no. 2, pp. 499-514, 2001.

[176] "EPO-TEK 377 Technical Data Sheet," Epoxy Technology, July 2019. [Online]. Available: http://www.epotek.com/site/administrator/components/com_products/assets/files/Style_Uploads/377.pdf. [Accessed 18 September 2019].

[177] "Thermal Conductivity of Metals, Metallic Elements, and Alloys," Engineering ToolBox, 2005. [Online]. Available: https://www.engineeringtoolbox.com/thermal-conductivity-metals-d_858.html. [Accessed 18 September 2019].